



# LUND UNIVERSITY

## Time-Frequency Analysis in Attosecond Spectroscopy

Isinger, Marcus

2018

*Document Version:*

Publisher's PDF, also known as Version of record

[Link to publication](#)

*Citation for published version (APA):*

Isinger, M. (2018). *Time-Frequency Analysis in Attosecond Spectroscopy* (1st ed.). [Doctoral Thesis (compilation), Atomic Physics]. Division of Atomic Physics, Department of Physics, Faculty of Engineering, LTH, Lund University.

*Total number of authors:*

1

*Creative Commons License:*

Unspecified

**General rights**

Unless other specific re-use rights are stated the following general rights apply:

Copyright and moral rights for the publications made accessible in the public portal are retained by the authors and/or other copyright owners and it is a condition of accessing publications that users recognise and abide by the legal requirements associated with these rights.

- Users may download and print one copy of any publication from the public portal for the purpose of private study or research.
- You may not further distribute the material or use it for any profit-making activity or commercial gain
- You may freely distribute the URL identifying the publication in the public portal

Read more about Creative commons licenses: <https://creativecommons.org/licenses/>

**Take down policy**

If you believe that this document breaches copyright please contact us providing details, and we will remove access to the work immediately and investigate your claim.

LUND UNIVERSITY

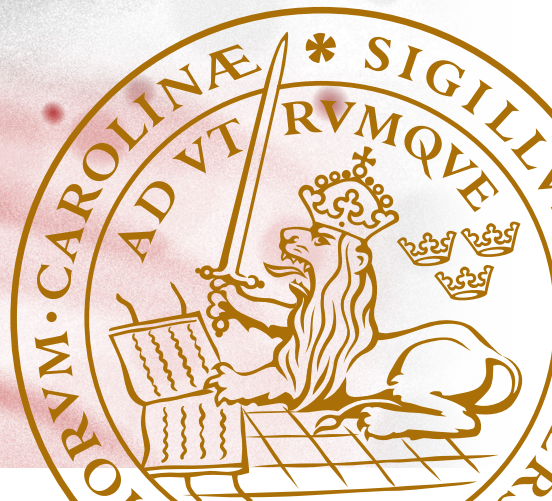
PO Box 117  
221 00 Lund  
+46 46-222 00 00

# Time-Frequency Analysis in Attosecond Spectroscopy

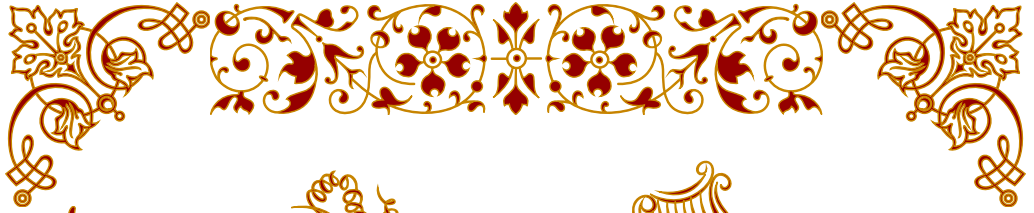
---

MARCUS ISINGER

DEPARTMENT OF PHYSICS | FACULTY OF ENGINEERING | LUND UNIVERSITY







*Time-Frequency*

*Analysis*

*in*

*Attosecond*

*Spectroscopy*



*Marcus Isinger*

*2019*





# Time-Frequency Analysis in Attosecond Spectroscopy

by Marcus Isinger



**LUND**  
UNIVERSITY

Thesis for the degree of Doctor of Philosophy

Thesis advisors:

Prof. Anne L'Huillier

Dr. Mathieu Gisselbrecht

Dr. Per Johnsson


Faculty opponent:

Prof. Dr. Thomas Pfeifer

To be presented, with the permission of the Faculty of Engineering of Lund University, for public criticism in Rydbergssalen at the Division of Atomic Physics on Friday, the 25th of January 2019 at 09:00.

|   |  |  |       |
|---|--|--|-------|
| Organization<br>LUND UNIVERSITY<br>Division of Atomic Physics<br>Box 118<br>SE-221 00 LUND<br>Sweden  |  | Document name<br>DOCTORAL DISSERTATION                       |       |
| Author(s)<br>Marcus Isinger   |  | Date of disputation<br>2019-01-25                            |       |
|   |  | Sponsoring organization                                      |       |
| Title and subtitle<br>Time-Frequency Analysis in Attosecond Spectroscopy  |  |  |       |
| <p>Abstract</p> <p>This thesis deals with ultrafast dynamics of electronic processes in rare gas atoms. The processes we explore include <i>photoemission</i>, where we time the emission of electrons moving away from the atomic core following ionization by a photon; and <i>auto-ionization</i>, where the atom spontaneously releases an electron wave-packet following photo-excitation. These processes occur on an attosecond and femtosecond time scale, respectively. The experimental results presented in this thesis have been obtained with the interferometric technique named RABITT, which involves ionizing a target with a train of attosecond pulses and "probing" the event with a weak IR pulse. The attosecond pulse train is generated by focusing an intense laser pulse of femtosecond duration into a gaseous medium. Through a well-known process called high-order harmonic generation, a broadband spectrum of phase locked frequencies are generated in the medium, resulting in a train of pulses with attosecond duration. The special characteristics of this spectrum allows for a quantum interferometer to be conceived by overlapping the train with a weaker replica of the femtosecond IR pulse. Information of the dynamics of the ionization process is imprinted in the interference fringes obtained by varying the delay between the APT and the IR pulse with attosecond precision.</p> <p>In the six papers that this thesis is based on, we investigate three different rare gas systems: <i>helium</i>, <i>neon</i> and <i>argon</i>. We are able to tell which electron, released out of two different shells of neon, escapes first from their parent atom, with a precision of 10 attoseconds or better. In helium, we are able to follow the creation of a wave-packet created by absorption of an attosecond pulse in the vicinity of a resonance and time its decay. We pave the way towards accessing all available information about a similar wave-packet creation in argon, through an angle detection technique with attosecond precision. We then perform a detailed examination of the interferometric technique used in all six papers (RABITT) and determine its limitations in terms of time resolution.</p> <p>The realization of this thesis work involved generating, from a fundamental frequency corresponding to a photon energy of 1.55 eV, high-order harmonics with photon energies exceeding 100 eV. It also involved developing a more stable optical interferometer, optimizing a 2 meter long time-of-flight electron spectrometer, developing scripts for treating and analyzing the data retrieved with the RABITT technique and creating a new interface for acquiring data from the spectrometers.</p> |  |  |       |
| Key words<br>Ultrafast, Atto, Time-Frequency  |  |  |       |
| Classification system and/or index terms (if any)   |  |  |       |
| Supplementary bibliographical information   |  | Language<br>English  |       |
| ISSN and key title<br>ISSN: 0281-2762   |  | ISBN<br>978-91-7753-892-9 (print)<br>978-91-7753-893-6 (pdf) |       |
| Recipient's notes   |  | Number of pages<br>229                                       | Price |
|   |  | Security classification                                      |       |

I, the undersigned, being the copyright owner of the abstract of the above-mentioned dissertation, hereby grant to all reference sources the permission to publish and disseminate the abstract of the above-mentioned dissertation.

Signature 

Date 2018-11-27

# Time-Frequency Analysis in Attosecond Spectroscopy

by Marcus Isinger



**LUND**  
UNIVERSITY

Thesis for the degree of Doctor of Philosophy



A doctoral thesis at a university in Sweden takes either the form of a single, cohesive research study (monograph) or a summary of research papers (compilation thesis), which the doctoral student has written alone or together with one or several other author(s).

In the latter case the thesis consists of two parts. An introductory text puts the research work into context and summarizes the main points of the papers. Then, the research publications themselves are reproduced, together with a description of the individual contributions of the authors. The research papers may either have been already published or are manuscripts at various stages (in press, submitted, or in draft).

Cover illustration: An illustration of neon 2s and 2p configurations under the influence of an attosecond pulse train and an IR pulse (Produced by the author with *Cinema 4D* and *GIMP*).

This thesis was typeset in *EB Garamond*, edited with *Atom* and compiled with Lua $\LaTeX$

All figures are produced (and in a few cases reproduced) by the author (if no other source is specified) using a combination of *MATLAB*, *Tikz/PGFPlots*, *PSTricks* and *Inkscape*.

Permissions:

- pp. i-96*      © Marcus Isinger 2019  
*pp. 97-105*    © 2018 CC  
*Paper I*        © 2018 CC BY 3.0  
*Paper II*       © the authors  
DOI: 10.1126/science.aao7043.  
Reprinted with permission from AAAS.  
*Paper III*     © 2018 CC BY 3.0  
*Paper IV*     © 2018 CC BY 4.0  
*Paper V*       © the authors  
*Paper VI*      © the authors

*Time-Frequency Analysis in Attosecond Spectroscopy*

Faculty of Engineering, Division of Atomic Physics

ISBN: 978-91-7753-892-9 (print)

ISBN: 978-91-7753-893-6 (pdf)

ISSN: 0281-2762

Printed in Sweden by Media-Tryck, Lund University, Lund 2019



*Dedikerad till Eléni,  
αγάπη μου,  
για πάντα!*



# Abstract

**T**HIS THESIS deals with ultrafast dynamics of electronic processes in rare gas atoms. The processes we explore include *photoemission*, where we time the emission of electrons moving away from the atomic core following ionization by a photon; and *auto-ionization*, where the atom spontaneously releases an electron wave-packet following photo-excitation. These processes occur on an attosecond and femtosecond time scale, respectively. The experimental results presented in this thesis have been obtained with the interferometric technique named RABITT, which involves ionizing a target with a train of attosecond pulses and "probing" the event with a weak IR pulse. The attosecond pulse train is generated by focusing an intense laser pulse of femtosecond duration into a gaseous medium. Through a well-known process called high-order harmonic generation, a broadband spectrum of phase locked frequencies are generated in the medium, resulting in a train of pulses with attosecond duration. The special characteristics of this spectrum allows for a quantum interferometer to be conceived by overlapping the train with a weaker replica of the femtosecond IR pulse. Information of the dynamics of the ionization process is imprinted in the interference fringes obtained by varying the delay between the APT and the IR pulse with attosecond precision.

In the six papers that this thesis is based on, we investigate three different rare gas systems: *helium*, *neon* and *argon*. We are able to tell which electron, released out of two different shells of neon, escapes first from their parent atom, with a precision of 10 attoseconds or better. In helium, we are able to follow the creation of a wave-packet created by absorption of an attosecond pulse in the vicinity of a resonance and time its decay. We pave the way towards accessing all available information about


---

a similar wave-packet creation in argon, through an angle detection technique with attosecond precision. We then perform a detailed examination of the interferometric technique used in all six papers (RABITT) and determine its limitations in terms of time resolution.

The realization of this thesis work involved generating, from a fundamental frequency corresponding to a photon energy of 1.55 eV, high-order harmonics with photon energies exceeding 100 eV. It also involved developing a more stable optical interferometer, optimizing a 2 meter long time-of-flight electron spectrometer, developing scripts for treating and analyzing the data retrieved with the RABITT technique and creating a new interface for acquiring data from the spectrometers.



# Popular scientific summary

UR UNDERSTANDING of the world around us took a giant leap with the advent and development of the atomic theory: the idea that all matter is composed of small building blocks called atoms (from Greek *ἄτομος*, *undivided*). The different properties of matter could be connected to the kind of atom it was composed of. The atoms themselves were later found to be made up of even smaller building blocks: a nucleus containing protons and neutrons and a "cloud" of electrons surrounding it.

The idea of tiny particles building up ourselves and everything around us dates back to ancient Greece, but it started to slowly gain traction in the middle of the 19th century when physicists and chemists developed a table of periodic trends seen in the then known 56 elements. This would later become the well-known periodic table. These periodic trends could be well explained by the atomic theory that was quickly emerging during the beginning of last century. Technological breakthroughs allowed advanced experiments to dig deep into atoms, confirming that there are tendencies in the arrangement of their electrons. Today, all 94 elements of natural occurrence have been scrutinized and their structures are available in huge databases. The behavior (in the chemical, physical or biological sense) of an atom or molecule, and by extension its macroscopic substance, is mostly determined by the arrangement, but also on the movements, of its electrons. Electronic motion in an atom can lead to emission of light. Motion of electrons on the molecular scale can transport information along a DNA molecule and it initiates changes in the chemical composition and function of biological systems.

The ability to track electron motion inside of atoms and molecules would be a breakthrough for all of science, not the least for medical applications. It is a challenging task since elec-

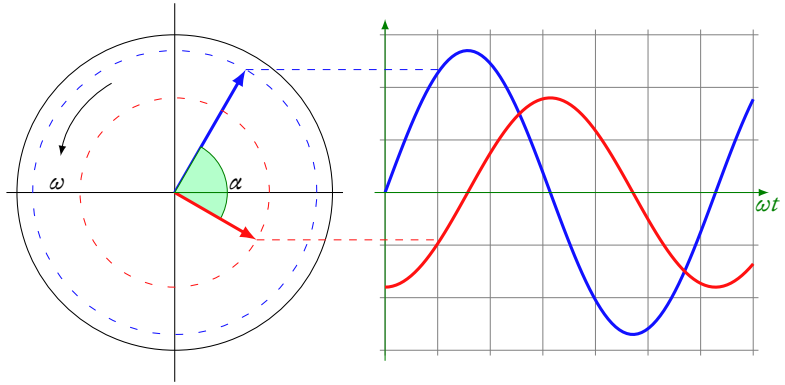


Figure 1. *The blue and red arrows are called phasors. We assign a certain amplitude (dotted circles) to each of them and a phase difference between them (the geometrical angle  $\alpha$ ). Once they start turning with an angular frequency  $\omega$ , the projected amplitude (dotted line) follows a wave motion, with the same amplitude, phase difference and frequency as their respective phasor.*

trons are some of the lightest matter in the universe, therefore moving very fast "around" the atom. One of the first steps towards this vision was taken in 2010, when scientists detected a minuscule time difference of two different electrons escaping a neon atom. This meant that the electron takes a small amount of time to be released from the atom: it is not an instantaneous process. In this thesis we have, amongst other things, further developed the means of timing and tracking electron motion as well as investigated with what accuracy we can do this.

To understand how these complex measurements work, along with most of the concepts described in this thesis, it is important to understand the concept of *phase*. A phase is a very fundamental property of a wave. In the physical sense, a wave is fully described by a frequency, an amplitude and a phase, but in the common sense we probably think of the frequency (as in the tone of a sound wave) and an amplitude (the loudness of the sound wave). If we take a light wave instead, the frequency of light now determines what color we see and the amplitude affects the brightness we sense. Why, then, is the phase so important?

When discussing abstract concepts it is useful to have a good analogy. In the field of attosecond physics we usually make a parallel to a single-arm clock, often called a phasor, seen on the

left in figure 1. The orientation of the arm depicts the phase and the length of the arm the amplitude. If the arm starts turning with a constant velocity, its motion follows a wave with a certain frequency (and its corresponding wavelength) as in figure 1. We can still assign a phase to the clock, but the value depends on what we compare the phase with. If two clocks are turning with the same speed, their arms opposite each other, the phase between them is 180 degrees at all times. If they are instead turning with different speeds, the phase difference depends on which moment in time we "freeze" their rotations. An important feature of the phase is that it is periodic. This means that we can only really detect a movement of the arm within a single turn, equivalent to 360 degrees. If we look away and the arm turns exactly one revolution, we have no way of knowing if it moved at all.

In order to easier conceive the importance of a phase, let us turn to figure 2 where we see a motorcycle. Just like a the groove of a vinyl record contains the sound waves from all instruments involved, we can treat the image lines as grooves: a sum of spatial waves with amplitude and phase information. In the middle, we see the result of keeping the phase of the waves, but replacing the amplitude information with noise. The photo is faint but still very much recognizable, even though the arm length of all clocks are completely random. On the bottom we see the reverse case, where the phase information has been replaced with noise. The arms are now pointing in a random direction, and a gray fog is all that remains.

The phase is clearly more important than the amplitude in the above case and for our measurements it is absolutely crucial. It can however be a very difficult property to measure physically, as in the case for visible light. Continuing the analogy with the clock above, neither our eyes nor a camera chip can detect the way the arm of the clock is pointing (phase), only the length (amplitude). The frequency of visible light is simply much too high (the wave oscillates a trillion times per second). It is not surprising then that a phase might be a foreign concept for us. Nonetheless, the phase can affect one of the properties our eyes are capable of perceiving: the amplitude.

An important feature of a wave, represented by a phasor, is that we can add different phasors to create new phasors, a process called interference. If we have one arm pointing at 12 o'clock

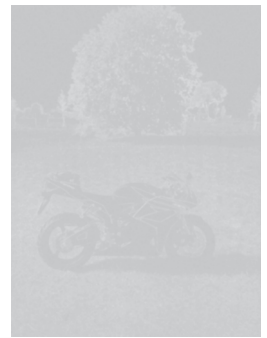


Figure 2. *On the top we see the full picture, an image of a motorcycle. This image is decomposed to its constituent "waves", and the amplitude information is replaced with noise while the phase information is kept. The result is seen in the middle. On the bottom we see the reverse case, where the phase information is instead replaced with noise while the amplitude information of the original image is kept.*




---

and one at 6 o'clock, their addition results in an armless clock, if their lengths are the same. Through the addition of phasors, we obtain a measurable result (a length change) that depends on their relative phase difference. If you have ever looked at the reflection off a wall of a laser pointer you have seen this in action. The spot looks grainy and the pattern moves when you move your head/eyes. What you see is actually the interference of waves on your retina. If we again use the analogy of the clock, the laser pointer emits only one color (related to the rotation speed of the turning arm), and all arms are synchronized: they are in phase. But when the laser light hits an uneven surface, the clocks will change direction when reflected on the rough surface (almost all surfaces are rough on the atomic scale). In our eyes the clocks add up, interfere, and the darker and brighter spots we observe results from this interference.

How is this then related to the timing of electron motion? In the same way that light exhibits particle- (i.e. the photon) and wave-properties, matter does too. An electron released from an atom following absorption of light can also behave as a wave, with an amplitude and a phase just like the phasor. The phase can tell us about the time evolution of a system, as long as we have a reference (we recall that *phase* is a relative term). It would be natural to relate the events to the light that caused the release of the electron, but this phase is not easily attained. What we can do is release two electrons simultaneously and compare their phases, and by extension determine which electron was released first. In essence we have then caught the movement of an electron at its own timescale.

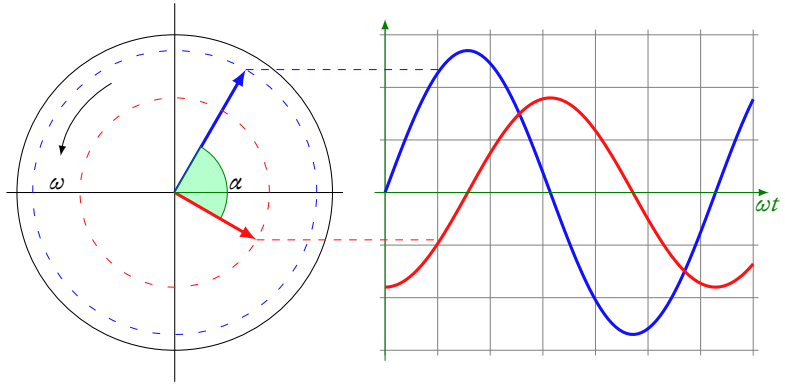


# Populärvetenskaplig sammanfattning

LLA ÄMNEENS egenskaper, från den genomskinliga och lätta luften vi andas till det sträva, vita pappret den här avhandlingen är tryckt på, kan förklaras av de byggstenar de består av. Detta misstänkte redan ”de gamla grekerna” och de kallade denna byggsten för *ἄτομος* (odelbar) vilket också blev namnet på dessa byggstenar: atomer. I mitten på 1800-talet började kemister att dela upp de ämnen som då var kända i grupperingar och man såg tydliga beteendemönster som mynnade ut i det nu välkända periodiska systemet. Dessa mönster kunde sedan förklaras med den atomteori som utvecklades på 1900-talet. I takt med att mätinstrument blev mer tekniskt avancerade kunde man fastställa att atomer består av en kärna med protoner och neutroner samt en yttre mantel av elektroner, bundna av kärnans attraktiva kraft. Hur en atom beter sig bestäms i mångt och mycket av hur elektronerna är grupperade, framförallt hur den yttersta grupperingen ser ut.

Idag är alla 94 upptäckta atomslag av naturlig förekomst kartlagda till minsta detalj. Vad som fortfarande saknas är en detaljerad förståelse för hur atomer interagerar med andra atomer, eller egentligen hur deras elektroner rör och förflyttar sig. Möjligheten att följa denna process i realtid skulle vara ett enormt kliv framåt för hela naturvetenskapen. Det är en oerhörd utmaning eftersom elektroner är några av de lättaste partiklarna i universum, och rör sig därför oerhört fort ”runt” atomerna.

En av de första milstenarna på vägen mot detta mål passerades 2010, då man uppmätte att två elektroner från olika skal i neon inte tog samma tid på sig att frigöras; man hade alltså ”tagit tiden” på en elektron och därmed följt dess rörelse, om än ganska primitivt fortfarande, experimentets komplexitet till trots. I denna avhandling har vi bland annat vidareutvecklat metoder för att följa elektroners rörelse bort från atomen och samtidigt



Figur 3. Den blå och röda pilen kallas för fasvinklar, och har egenskaper som en amplitud (streckade cirkeln) och en vinkelskillnad ( $\alpha$ ). När de börjar snurra med konstant vinkelhastighet  $\omega$  så följer deras projicerade amplitud (streckade linjen) en vågrörelse (blåa och röda kurvan) med samma amplitud, fas och frekvens.

undersökt hur noggrant vi kan göra detta.

För att förstå principen bakom dessa experimentella metoder måste man vara bekant med begreppet *fas*. En fas är en fundamental egenskap hos en våg. En våg i den fysikaliska meningen kan beskrivas helt med en frekvens, en fas och en amplitud, men i den allmänna bemärkelsen tänker vi nog oftare på frekvensen (som i tonen hos en ljudvåg) och intensiteten (hur högt vi uppfattar en ljudvåg). När det kommer till ljus bestämmer frekvensen vilken färg vi ser och intensiteten hur ljusst något är. Så varför ska vi bry oss om fasen?

För att förstå detta abstrakta koncept ska vi ta till en analogi. En bra analogi i det här fallet är ett visardiagram (fasvektor), alltså en enarmad klocka, som syns i figur 3. Riktningen hos visaren bestämmer fasen och längden blir dess amplitud. Vi kan förstå att en fas är ett relativt begrepp, eftersom vi förlorar vår referens om "urtavlan" skulle vridas. Det blir också tydligt att om vi har en fas som ändrar sig med tiden så börjar visaren att snurra, och visarens position i höjdlid bildar då en våg med en frekvens som bestäms av hur snabbt visaren snurrar. När visaren snurrar behöver vi en till visare som snurrar för att kunna säga vilken fas visaren har, i vilket fall vi menar vinkelskillnaden mellan de två visarna. Om visarna pekar i tvärt olika riktningar har de 180 graders fasskillnad. Om de däremot skulle snurra med olika hastighet måste vi

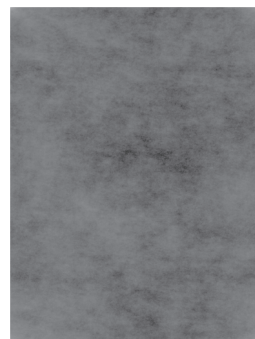
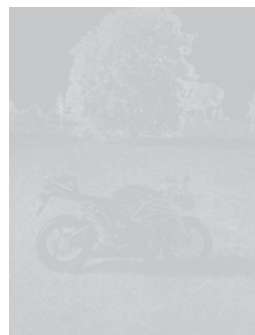
välja ett ögonblick och ”stanna tiden” för att kunna bestämma fasskillnaden.

En viktig egenskap hos en fas är att den är periodisk, den kan bara anta värden mellan 0 och 360 grader, efter vilka den repeterar sig. Om vi skulle titta bort medan visaren rör sig exakt ett varv kan vi inte veta om visaren rört sig alls.

För att visa just hur viktig fasen är för en våg kan vi vända oss till figur 4 där ser vi en bild av en motorcykel. Denna bild har nu tolkats som en summa av många vågor, alla med en fas och amplitud. Detta kan vara svårt att föreställa sig, men på samma sätt som ett ljudspår på en vinylskiva består av summan av ljudet från alla instrument kan man tolka varje rad i bilden som ett ”bildspår”. I mitten av figuren ser vi vad som blir kvar om vi bara behåller fas-informationen men ersätter amplitud-informationen med slumpmässigt brus. Porträttet är fortfarande igenkännligt, trots att alla information om visarnas längder (figur 3) är borta. Nederst i figuren ser vi å andra sidan vad som blir kvar om fas-informationen istället ersätts med brus. Nu pekar visarna i totalt slumpmässig riktning. En grå dimma är allt som syns i bilden.

Fas-informationen hos en våg är alltså i föregående fall viktigare än amplituden, och för våra experiment är den helt väsentlig, men när det kommer till ljus är den ganska svår att mäta fysikaliskt. Varken våra ögon eller en kameras sensor kan mäta fasen hos ljusvågor som träffar dem, då ljusvågen har en väldigt hög frekvens (synligt ljus oscillerar en biljon gånger i sekunden). Däremot kan fasen påverka det våra ögon kan uppfatta; amplituden.

En viktig egenskap hos en våg, som vi sedan tidigare representerar med en klockvisare, är att man kan addera dem för att få nya klockvisare, en process som kallas interferens. Både fasen och amplituden avgör den resulterande visarens riktning och längd. En visare som pekar klockan 12 och en som pekar klockan 6, blir till en klocka utan visare (om de båda visarna är lika långa). Genom att addera två visare, får vi ett mätbart resultat (skillnad i längd) som beror på deras inbördes fas. Detta har ni säkert sett själva om ni studerat en laserpekares ljusprick på nära håll. Den ser lite grynig ut, och grynen rör sig när man flyttar på blicken. Den uppfattas som grynig för att vissa delar av ljuspricken släcks ut. Ljuset från lasern består av många visare som alla pekar i samma riktning. När de reflekteras på en ojämn yta (ojämn på mikroskopisk nivå) påverkas visarnas riktning, och vissa visare



Figur 4. Överst i figuren ser vi en svartvit bild av en motorcykel. Pixelvärdena i bilden tolkas sen som en summa av vågor med en fas och amplitud. Figuren i mitten visar resultatet av att ersätta amplitud-informationen (längden hos visarna) hos alla vågor med slumpmässigt brus. Nederst i figuren har istället fas-informationen (riktningen hos visaren) ersatts med brus.

---

kommer peka i motstående riktning. När ljuset når vårt öga läggs visarna ihop och några visare kommer släcka ut varandra medan andra kommer skapa längre visare, vilket leder till att vi ser ljusa och mörka områden i ljuspricken.

Vad har då detta med tidtagningen av elektroner att göra? Jo, en elektron som frigörs från en atom kan också bete sig som en våg, likt en klockvisare med en fas och amplitud. Fasen kan säga oss något om tidsförloppet (tänk er en sekundvisare) så länge vi har något att jämföra med (som nämnt ovan är fas ett relativt begrepp). Det naturliga vore att jämföra med fasen hos ljuset som frigjorde elektronen från atomen, men denna fas är inte lättillgänglig. Däremot kan vi jämföra olika elektroners faser och därmed ta reda på vilken som frigjordes först och hur stort försprånget var. På ett någorlunda rudimentärt sätt har vi då uppmätt en elektrons rörelse på dess egna tidsskala.



# List of Publications

This thesis is based on the following papers:

Paper I **Roadmap of ultrafast x-ray atomic and molecular physics**

Linda Young, Kiyoshi Ueda, Markus Gühr, Philip H Bucksbaum, Marc Simon, Shaul Mukamel, Nina Rohringer, Kevin C Prince, Claudio Masciovecchio, Michael Meyer, Artem Rudenko, Daniel Rolles, Christoph Bostedt, Matthias Fuchs, David A Reis, Robin Santra, Henry Kapteyn, Margaret Murnane, Heide Ibrahim, François Légaré, Marc Vrakking, **Marcus Isinger**, David Kroon, Mathieu Gisselbrecht, Anne L’Huillier, Hans Jakob Wörner and Stephen R Leone.  
*Journal of Physics B: Atomic, Molecular and Optical Physics*, 51, 032003 (2018).

Paper II **Photoionization in the time and frequency domain**

**Marcus Isinger**, Richard J. Squibb, David Busto, Shiyang Zhong, Anne Harth, David Kroon, Saikat Nandi, Cord L. Arnold, Miguel Miranda, Jan Marcus Dahlström, Eva Lindroth, Raimund Feifel, Mathieu Gisselbrecht, Anne L’Huillier.  
*Science*, 358, 893-896 (2017).

Paper III **Time-frequency representation of autoionization dynamics in helium**

David Busto, Lou Barreau, **Marcus Isinger**, Margherita Turconi, Christina Alexandridi, Anne Harth, Shiyang Zhong, Richard J. Squibb, David Kroon, Stefan Plogmaker, Miguel Miranda, Álvaro Jiménez-Galán, Luca Argenti, Cord L. Arnold, Raimund Feifel, Fernando Martín, Mathieu Gisselbrecht, Anne L’Huillier, Pascal Salières.

*Journal of Physics B: Atomic, Molecular and Optical Physics*, 51, (2018) 044002.

Paper IV **Anisotropic photoemission time delays close to a Fano resonance**

Claudio Cirelli, Carlos Marante, Sebastian Heuser, Leon Petersson, Álvaro Jiménez-Galán, Luca Argenti, Shiyang Zhong, David Busto, **Marcus Isinger**, Saikat Nandi, Sylvain Maclot, Linnea Rading, Per Johnsson, Mathieu Gisselbrecht, Matteo Lucchini, Lukas Gallmann, Jan Marcus Dahlström, Eva Lindroth, Anne L’Huillier, Fernando Martin, and Ursula Keller.

*Nature Communications*, 9, (2018) 9:955.

Paper V **Temporal resolution of the *RABBIT* technique**

**Marcus Isinger**, David Busto, Sara Mikaelsson, Shiyang Zhong, Danielle Dowek, Pascal Salières, Anne L’Huillier, Cord L. Arnold and Mathieu Gisselbrecht.

*Philosophical Transactions A*, Submitted, (2018).

Paper VI **Fano’s propensity rule in angle-resolved attosecond pump-probe photoionization**

David Busto, Jimmy Vinbladh, Shiyang Zhong, **Marcus Isinger**, Saikat Nandi, Sylvain Maclot, Per Johnsson, Mathieu Gisselbrecht, Anne L’Huillier, Eva Lindroth, and Jan Marcus Dahlström.

*Physical Review Letters*, Submitted, (2018).

# Abbreviations

|        |   |
|--------|---|
| ADC    | Analog-to-Digital Converter   |
| APT    | Attosecond Pulse Train  |
| CCD    | Charge-Coupled Device   |
| CPA    | Chirped Pulse Amplification   |
| CW     | Continuous Wave   |
| FFT    | Fast Fourier Transform  |
| FWHM   | Full-Width at Half-Maximum  |
| HHG    | High-order Harmonic Generation  |
| IR     | Infrared  |
| KLM    | Kerr-Lens Modelocking   |
| MBES   | Magnetic Bottle Electron Spectrometer   |
| MCP    | Microchannel Plate  |
| ML     | Mode Locking  |
| RABITT | Reconstruction of Attosecond Beating<br>by Interference of Two-photon Transitions |
| SAP    | Single Attosecond Pulse   |
| SPIDER | Spectral Phase Interferometry<br>for Direct Electric-field Reconstruction         |
| TOF    | Time of Flight  |
| VMIS   | Velocity Map Imaging Spectrometer   |
| XUV    | Extreme Ultraviolet ( $10 < \hbar\omega < 124 \text{ eV}$ )                       |





# Contents

## *Thesis*

---

|   |   |     |
|---|---|-----|
| 1 | Introduction to the Ultrafast           | 3   |
| 2 | Generation of Short Light Bursts        | 11  |
| 3 | Interferometry with Photoelectrons      | 27  |
| 4 | Time-Frequency Analysis                 | 43  |
| 5 | Outlook                                 | 67  |
|   | The Author's Contribution to the Papers | 73  |
| A | Documentation for an ADC                | 79  |
| B | Photoniques Special Issue               | 97  |
|   | References                              | 115 |
|   | Index                                   | 117 |

## *Papers*

---

|     |  |     |
|-----|--|-----|
| I   | Roadmap of ultrafast x-ray atomic and molecular physics            | 121 |
| II  | Photoionization in the time and frequency domain                   | 129 |
| III | Time-frequency representation of autoionization dynamics in helium | 139 |
| IV  | Anisotropic photoemission time delays close to a Fano resonance    | 153 |

- V Temporal resolution of the *RABBIT* technique 171
- VI Fano's propensity rule in angle-resolved attosecond pump-probe photoionization 191

# THESIS



# Introduction to the Ultrafast

*In the microcosm, the borders between biology, chemistry, and physics tend to disappear. The gaps between these apparently so disparate fields are bridged by the microscopic motion of electrons in atoms, molecules, and nanoscale structures. Electronic motion inside atoms is behind the emission of visible, ultraviolet, and x-ray light. Electronic dynamics on the molecular scale is responsible for the transport of bio-information and initiates changes in the chemical composition and function of biological systems. Details of these motions often occur on time scales of tens to ten thousands of attoseconds ( $1 \text{ as} = 10^{-18} \text{ s}$ ) and require commensurate measurement and control techniques for their observation and steering, respectively. Can the function of bio-molecules be manipulated and novel molecular structures be formed by steering electrons in chemical bonds? How does charge transfer occur in molecules assembled on surfaces and how can it be optimized for more efficient solar cells? What are the ultimate size and speed limits of electronic information processing and magnetic information storage, and how can we approach these limits? Answers to these scientific and technological questions will first require insight into and later possibly control of microscopic electron motion.*

- 1.1 The timescale of microcosm
- 1.2 Short light bursts
- 1.3 Interference of waves
- 1.4 Scope of this work
- 1.5 Papers and outline

## 1.1 THE TIMESCALE OF MICROCOSM

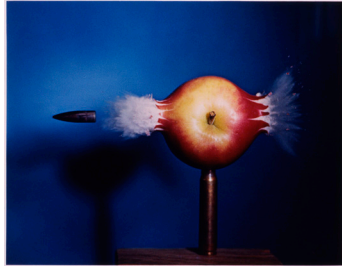


Figure 1.1. Harold E. Edgerton, *Bullet through Apple*, 1964, printed 1984, dye transfer print, Smithsonian American Art Museum.

**T**HE SMALLER the system we want to study is, the faster the dynamics of said system is expected to be. This is a universal rule, applicable to the macrocosm as well as the microcosm. In the macrocosm, typical motion (such as revolution of galaxies) occurs on a timescale of millions of years and beyond. In the microcosm, the world of atoms, movements are very rapid and often referred to as ultrafast. The term *ultrafast* is used to describe a physical process with a duration shorter than a nanosecond ( $10^{-9}$  s), though this definition is not set in stone. Water molecules (i.e. movement of many atoms bundled together) vibrate on a timescale measured in picoseconds ( $10^{-12}$  s). The same water molecule is broken up into its constituent atoms (i.e. movements of single atoms) in a few of femtoseconds ( $10^{-15}$  s) [1]. The motion of electrons around the atom is instead unfolding in attoseconds ( $10^{-18}$  s). How could we ever detect this motion?

To be able to capture a sharp snapshot of the wings of a fly in motion, a camera needs to open and close its shutter in a millisecond of time. The fastest shutters today are able to open and close in just a microsecond, before mechanical constraints start to be of issue. To capture motion faster than this, we can play a trick with the lighting. If we eliminate the background light, and illuminate the object with a short burst of intense light, it can be as short as 10 ns, the shutter speed is not a limitation anymore. The short burst of light ensures that a single instance in time will be captured by the sensor, allowing for a snapshot of a bullet through an apple to be captured on camera, as seen in figure 1.1.

Can the same technique be used to capture electron motion? In a way, yes, but the flash and camera are quite different. First of all, we have no way of "seeing" an electron in the literal sense, we can just detect traces of it. The flash to "freeze" electron motion is on the other hand more similar, but neither a mechanical nor electronic solution can produce a flash of attosecond duration. What is needed is a purely optical solution.

## 1.2 SHORT LIGHT BURSTS

Several technological breakthroughs were required to advance ultrafast science from the nanosecond regime, which could be accessed using a normal, incoherent light flash, to the attosecond time scale. The laser [2], discovered in 1960, was the first and most crucial breakthrough. The laser could emit a light wave with an almost perfect single frequency, offering a completely new layer of controlling light.

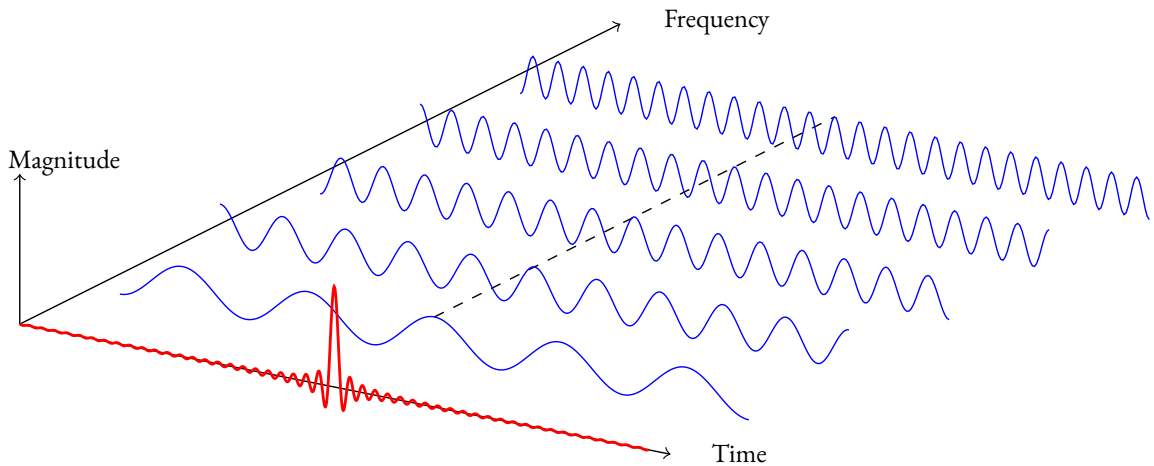


Figure 1.2. *By adding many waves with different frequencies together, it is possible to create a wave with a magnitude spike confined to a small region in time or space. This wave is often called a pulse or a wave packet. The dashed line connects the crest of each wave, indicating the phase relation between the waves. A straight line generates the shortest pulse, a tilted or curved line results in a longer pulse. The more frequencies are added, the shorter the pulse duration gets.*

A single frequency is useful for many spectroscopic applications, but ultrafast science is not one of them. A single frequency is by definition infinitely stretched in time. Let us instead see what happens when we add many frequencies together. As seen in figure 1.2, by adding waves of increasing frequency, the resulting wave is confined to a very narrow region in time, a pulse, where all frequencies are in phase\*. To create a shorter pulse, we "just" need to add more waves in phase. In practice, this was realized by utilizing new-found properties of some transparent

\*Indicated by the dashed line



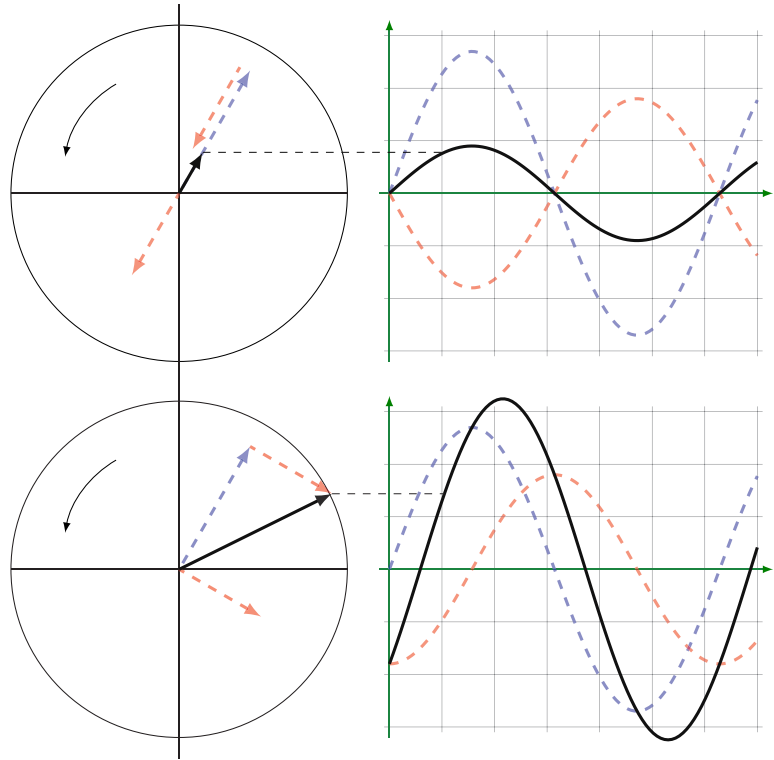


Figure 1.3. *Interference of the blue and red phasor and the corresponding waves. Adding the red phasor to the blue phasor results in the black phasor. (Top) When the phase difference is  $\pi$ , the black phasor is minimal and the wave that results from the rotation is the least intense. (Bottom) When the phase difference is  $\frac{\pi}{2}$  the amplitude is larger and the interference results in a more intense wave.*

materials [3] which emitted more frequencies of light while passively keeping them in phase, leading to the first laser pulses of femtosecond duration.

The next leap was when a process now called High-order Harmonic Generation (HHG) [4, 5] was discovered, which quickly inspired the notion of generating pulses of attosecond duration [6–8]. By focusing a highly intense laser pulse into a dense gas, it was possible to generate a large range of high frequencies, capable of adding up to an attosecond pulse. But even if they did, how would we confirm it?

### 1.3 INTERFERENCE OF WAVES

The first detection and proof of attosecond pulses came in 2001, where two groups independently of each other detected a train of attosecond pulses [9] and a single attosecond pulse [10], marking the birth of attosecond science. The two experimental techniques that made this possible both relied on a phase sensitive measurement, revealing all necessary information about the wave. Throughout this thesis we will only discuss the foremost technique, which is based on interference of waves.

Most instruments for detecting light waves only measure the intensity of a wave, so in order to measure the phase of a wave it is often necessary to include another wave; a reference wave. Let's say we want to measure the phase of an unknown wave, the blue wave in figure 1.3. First we generate a reference wave, the red wave, whose phase we can control precisely\*. We let the two waves interfere, i.e. we add them together as in figure 1.3, and we measure the intensity of the resultant (the black curve). On the top of figure 1.3, the resulting wave is weak since the blue and red waves are completely out of phase. When the phase between the two waves changes, the resulting wave changes as well. If we record the intensity\* at every phase difference, from 0 to  $2\pi$ , we get an oscillating intensity curve. The phase of this new curve depends only on the phase of the blue and red waves, and since we control the phase of the red wave, we can determine the phase of the blue wave. This is the principle behind the first detection of an attosecond pulse train. For a more rigorous walk-through, see the succeeding chapters.

The confirmation of an attosecond "flash" was the starting gun for studying electron motion in atoms and molecules in real time. In 2002, the first experiment using attosecond pulses was successfully carried out [11]. Drescher and coworkers managed to follow an inner shell electronic process of Krypton atoms on a femtosecond timescale with attosecond resolution. Since then, other atomic processes such as valence electron motion [12] and photoionization [13–15] has been studied, but also electron dynamics in solids [16] and molecules [17]. All experiments have in common the use of a reference wave, which very roughly can be thought of as the "camera", allowing for snapshots to be taken at different relative position of the reference wave.

\*How this is done experimentally will be discussed later on

\*A measure of the length of the phasor

## 1.4 SCOPE OF THIS WORK

The scope of this thesis is limited to studying the temporal aspects of photoionization of atoms, the process where an atom absorbs light (a photon) and an electron is released. The experimental method used throughout this work is based on interference of the released electrons (photoelectrons), utilizing the wave nature of electrons, bearing much resemblance to the description above. The method was originally suggested in 1996 [18] and demonstrated in 2001 [9, 19] where it was dubbed RABITT\* (*Reconstruction of Attosecond Beating by Interference of Two-photon Transitions*). Interestingly, the time resolution that can be obtained is ultimately not limited by the duration of the pulse but rather by the precision with which we can control the relative phase between the attosecond pulse (the "flash") and the reference wave.

\*The community has still not agreed on the spelling of the acronym

## 1.5 PAPERS AND OUTLINE

In this thesis work we pushed the interferometric technique further by installing a high resolution photoelectron spectrometer and improving the long and short term stability of the interferometer, which allowed developing the analytical process as demonstrated in *Paper II*. In this paper we revisited the scope of reference [14] and resolved the discrepancy between experimental observations and theoretical predictions.

In *Paper I* we discuss the current status and challenges of photoionization dynamics in atoms, in a road-map on ultrafast atomic and molecular physics. While *Paper II* investigates photoionization in neon on an attosecond timescale, *Paper IV* and *Paper III* focuses on resonant photoionization, which occurs on a femtosecond timescale, showcasing the versatility of RABITT. In *Paper III* we follow the spontaneous emission of electrons (*autoionization*) following photo-excitation of helium. In *Paper IV* we use a similar technique to showcase a proof-of-principle measurement in argon, where the autoionization process is more complicated due to the number of electronic states involved. In the same measurement, we found a periodic modification of the angular distribution of the photoelectrons in *non-resonant* ion-

ization, as described in *Paper VI*. In *Paper V*, we perform a thorough investigation of the RABITT technique itself by simulating different experimental conditions.

The succeeding chapters will explain in detail how the attosecond flash is created and how we use this flash to follow electron motion. Starting with *Chapter 2*, the procedure of generating attosecond pulses in a train is described and the theoretical model helping us understand and optimize the process is reviewed. *Chapter 3* describes photoelectron detection for attosecond experiments and the interferometric technique\* is introduced and thoroughly explained. *Chapter 4* describes the extensive analysis made possible by RABITT and shows how we can use this analysis to follow electron motion. Finally, *Chapter 5* gives a summary and an outlook.

\*i.e. RABITT





# CHAPTER 2

## Generation of Short Light Bursts

*Just one year after the invention of the first working laser, the very same laser was responsible for the discovery of a new property of transparent media. It was found that a quartz crystal, upon being illuminated by the laser beam, caused some of the light passing through to oscillate twice as fast, in other words the frequency had been doubled. This highly nonlinear optical process, called second harmonic generation, discovered thanks to the high intensity of laser light, is a common tool today to create light waves at frequencies where lasing is difficult to achieve. Two decades later, in 1987, another similar process was discovered, this time allowing for not one new frequency but a dozens or more to be generated at higher harmonic orders than ever before.*

- 2.1 Generation of femtosecond pulses
- 2.2 Generation of attosecond pulses
- 2.3 The HHG setup in Lund
- 2.4 Summary

---

### 2.1 GENERATION OF FEMTOSECOND PULSES

**A**LL LIGHT around us results from electronic motion. Most\* of it is generated when electrons move to a lower energy state, be it the sun, an incandescent light bulb, an LED or a laser. As was briefly discussed in the earlier chapter, in order to create a burst of light with a duration much shorter than a mechanical shutter or an electronic switch can produce, a purely optical solution needs to be adopted. As

\*There are exceptions, for example synchrotron light

was shown, a broad band of plane waves with increasing frequencies add up to a short pulse/wave packet. The pulse duration,  $\Delta\tau$ , of the wave packet and the spectral bandwidth,  $\Delta\nu$ , of the waves are related via the *time-bandwidth product* [20], a property which is prevalent whenever waves are studied\*:

$$\Delta\tau \cdot \Delta\nu \geq 0.44 \quad (2.1)$$

It is clear that the shorter the pulse duration we aim for, the broader the bandwidth needs to be. A pulse of 10 fs duration requires a bandwidth of roughly 44 THz ( $44 \cdot 10^{12}$ Hz). Visible light spans from 400 to 700 THz\*, meaning visible light can support a 10 fs pulse. However, let's assume we want a wave-packet with a central wavelength of 800 nm\*. At 800 nm, a 44 THz bandwidth corresponds to a band of wavelengths 100 nm broad, i.e. if all wavelengths from 750 to 850 nm oscillate in phase, they add up to a pulse of 10 fs duration. In the following, we will see how this can be achieved experimentally, but for a more extensive review see reference [21].

To achieve this in practice is not a trivial feat, but one of the most common solutions spells *Ti:Sapphire*. This material, titanium-ion ( $\text{Ti}^{3+}$ ) doped sapphire ( $\text{Al}_2\text{O}_3$ ) crystal, or Ti:Sapphire, has several qualities which makes it an ideal laser gain medium [22]. If we turn to figure 2.1, we see the first reason. It has a gain curve almost 400 nm broad, peaking at 800 nm, meaning it certainly can support our 10 fs pulse. At the same time, the absorption curve is well separated and peaks at 530 nm, a region where many commercial pump lasers function. What is more, the sapphire crystal can sustain high laser power since it can be efficiently cooled, owing to its high thermal conductivity.

The issue now is that all the waves, or modes, needs to be phase-locked in relation to each other to create a traveling pulse in the laser cavity. This can be solved by utilizing a non-linear effect of the crystal, called the *Kerr lens effect*, and designing the laser cavity accordingly. The refractive index of a medium becomes intensity dependent at high laser intensities, with a maximum at the center of the beam, so that the medium acts as a lens for the laser beam. If an aperture is placed after the medium, we restrict the cavity to only amplify light which is intense enough to focus through the aperture, in this case a femtosecond pulse. This is

\*Gaussian pulse shapes and FWHM are assumed

\*Or conversely, from 700nm to 400nm  
\*i.e. in the NIR or Near InfraRed region. However, it is referred to as IR henceforth.

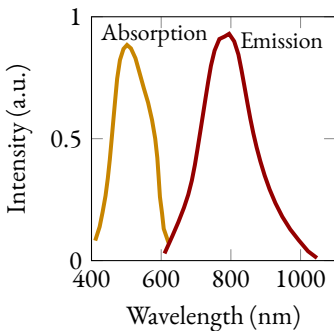


Figure 2.1. The gain and pump curve of Ti:Sapphire.

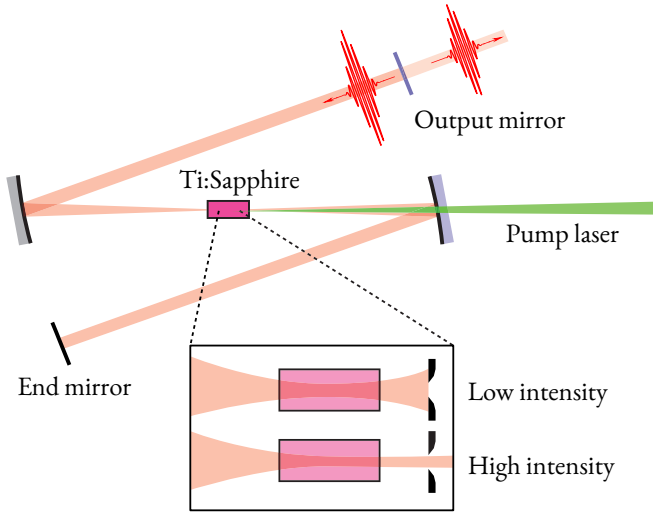


Figure 2.2. Principle of a z-shaped Ti:Sapphire mode-locked oscillator, showcasing how the Kerr-lens effect aids in achieving mode-locking.

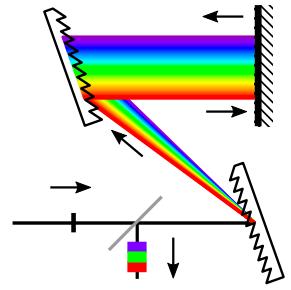


Figure 2.3. A pulse can be stretched in time by simply allowing different colors (frequencies) to travel different lengths, thereby delaying the blue colors with respect to the red colors, leading to a longer pulse.

called passive mode-locking. All we need is a short pulse to spontaneously appear, and it will be self-sustained, similar to how a combustion engine needs an initial turn of the crank to sustain the movement. We can "kick-start" the oscillator by introducing a disturbance, moving a mirror for example, until a short pulse appears and the oscillator is mode-locked. A schematic drawing of this process is seen in figure 2.2. Not shown is a way of compensating for the dispersion in the cavity. With broadband light we have to take into account that waves of different frequencies do not necessarily travel at the same speed in air or transparent media, which leads to a stretching of the pulse length if not properly compensated for. A common way to compensate for the dispersion in air is to introduce two gratings (shown in figure 2.3) or prisms (shown in figure 2.4) in the laser cavity.

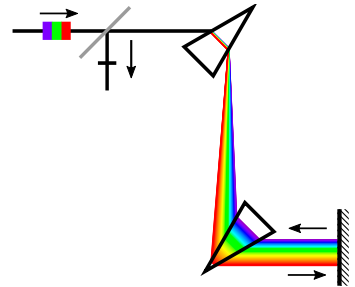


Figure 2.4. A stretched (chirped) pulse can also be compressed in time by advancing the blue colors with respect to the red colors, causing all frequencies to be in phase.

Can the same technique be used to generate attosecond pulses? A 10 as (attosecond) pulse needs a bandwidth of 44 PHz ( $44 \cdot 10^{15}$  Hz), meaning visible light cannot be used anymore. The high frequencies correspond to wavelengths in the region between 124 nm to 10 nm, called xuv (*eXtreme Ultraviolet*). The biggest issue working with xuv (and X-rays for that matter) is that most mirrors are not reflective for xuv light at normal incidence, as figure 2.5 shows, massively complicating



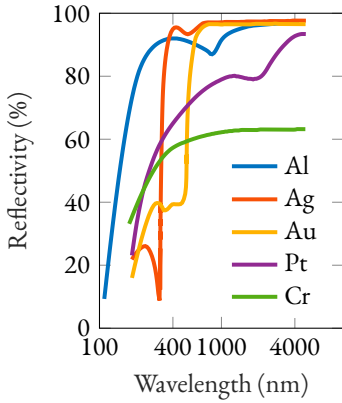


Figure 2.5. Reflectivity of different metals from the IR to XUV region.

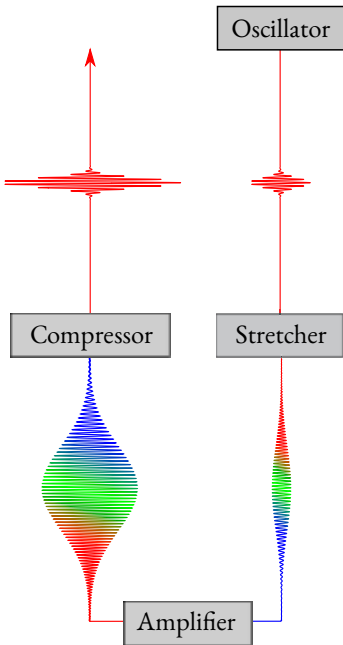


Figure 2.6. The principle of CPA. The pulses from the oscillator are first stretched in time, then amplified and lastly compressed to their final pulse duration and energy.

the design of the laser cavity for XUV radiation. A very different technique is indeed required, a technique which will utilize the extreme intensities that a femtosecond laser can achieve thanks to the ultrashort pulse duration.

Even though the output pulse of a properly dispersion-compensated mode-locked Ti:Sapphire oscillator can reach durations below 10 fs, the energy of a single pulse is normally limited to a few nanojoule (nJ). As we will see in the next section, to be able to generate attosecond pulses from a femtosecond pulse we need to reach peak powers in the TW ( $10^{12}$  W) region. For a pulse of 10 fs duration, this roughly means a pulse energy of 10 mJ, i.e. a million times more than the output of the oscillator. The problem is, if we were to send the oscillator output pulse through an amplifier chain of Ti:Sapphire crystals until we reach the desired energy, the peak powers will be high enough to destroy the crystals immediately. However, the crystals can be spared if the energy is in some way dispersed in space or time. Due to size constraints of the crystals and the optical elements, it is preferred to disperse the energy in time by simply stretching the pulse. As was mentioned earlier, a prism or a grating can be used to either stretch (figure 2.3) or compress (figure 2.4) pulses. By first stretching the pulse from a few fs to around 100 ps, the pulse can be amplified by a factor of  $10^6$  before being compressed to the final pulse length. This technique is called CPA (*Chirped Pulse Amplification*). A flowchart of the procedure is seen in figure 2.6. In fact, the 2018 Nobel Prize in Physics was awarded to Gérard Mourou and Donna Strickland for this technique, invented in 1985 [23].

## 2.2 GENERATION OF ATTOSECOND PULSES

In 1987 it was discovered that if we focus the laser pulse from a picosecond laser with an intensity of  $10 \text{ TW}/\text{cm}^2$  into a dense rare-gas target, the extreme intensities will cause a small fraction of the light to be up-converted to much higher orders than ever observed before [4, 5], seen in figure 2.7. The process was subsequently named *High-order Harmonic Generation* or HHG. It was soon realized that the broad spectrum of light generated in HHG could consist of attosecond pulses [8].

Even before the discovery of HHG, the non-linear process of frequency conversion was well known. Light propagating through a dielectric\* medium, such as a quartz crystal, will exert a force on the electrons in the medium, causing a charge separation. The collective induced separation, *polarization*, in the medium is called the *polarization density*,  $P$ :

$$P = \underbrace{\varepsilon_0 \chi^{(1)} E}_{\text{linear}} + \underbrace{\varepsilon_0 \chi^{(2)} E^2 + \varepsilon_0 \chi^{(3)} E^3 \dots}_{\text{non-linear}} \quad (2.2)$$

As seen, the polarization is a function of the electric field,  $E$ , and depends on the medium-dependent electric susceptibility\*,  $\chi$ . The polarization of the medium will affect the propagating light by acting as a light source itself. For electric field strengths much smaller than the electric field of the atoms in the medium, the polarization is well described by solely the linear term. The light propagating in the medium might then be *delayed*, if all frequencies are equally affected, or *dispersed* in time, if  $\chi$  is instead frequency dependent. This effect can be utilized or compensated for as we have seen earlier in this chapter.

Now, a field strength that is comparable to the atomic field ( $\sim 10^{11}$  V/m for the hydrogen atom) opens the door for a wide range of interesting phenomena, such as Kerr-lensing or second harmonic generation, and the non-linear terms must be included to describe these phenomena. For example, we see that the source will oscillate twice as fast if the second term is included, since  $E^2 \propto e^{i2\omega t}$ , where  $\omega$  is the frequency of the propagating light, thereby explaining second harmonic generation.

However, this model cannot fully describe the HHG process. Not only were the harmonics of very high orders, but the conversion efficiency seemed to be constant for a majority of the harmonic orders, shown in figure 2.7, in stark contradiction to equation 2.2 where each order is expected to be much lower than the previous. What follows now is a detailed explanation of the HHG process and how we can control it to obtain attosecond pulses.

### 2.2.1 HHG - the single atom response

The phenomena of HHG can be quite successfully modeled by a semi-classical model introduced in 1993 [24, 25] called *the*

\*a medium with a high polarizability

\*A measure of a material's polarization in response to an electric field, related to the refractive index as  $n^2 = 1 + \chi$

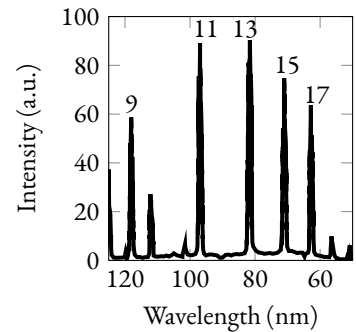


Figure 2.7. Harmonics generated from a fundamental wavelength of 1064 nm. Reproduced from reference [5].

*three-step model.* The model hinges on quantum mechanical concepts, but the mathematical description is classical. It is based on the premise that the electric field of the laser pulse is strong enough, meaning on the same order as the atomic potential, to modify the electric potential that a bound electron is subjected to. The sequence of the events that follow can be divided into three distinctly different steps. These steps are depicted in figure 2.8.

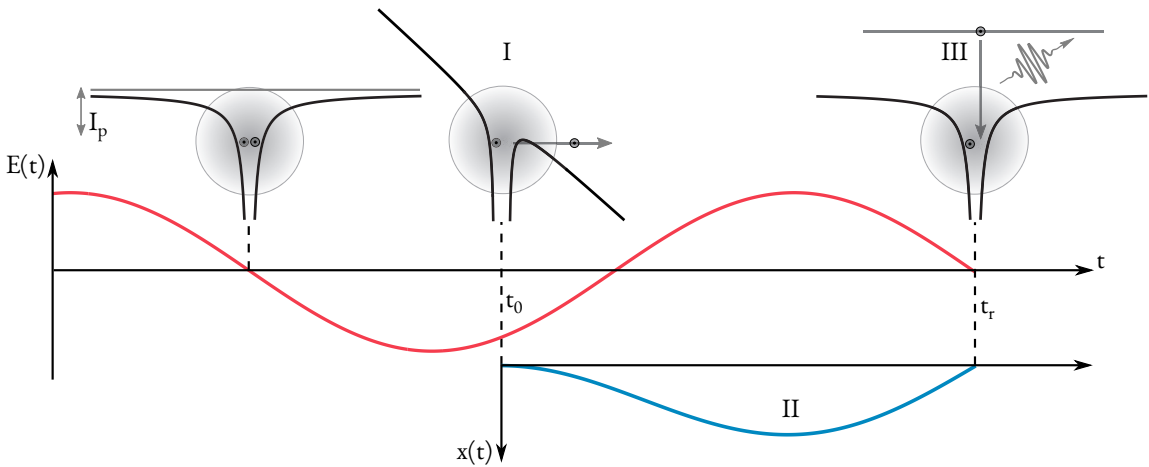


Figure 2.8. *Illustration of the three-step model. The electron is bound in an atomic potential. A strong, varying electric field (red wave) distorts the potential, allowing the electron to tunnel out of the potential at a time  $t_0$ . If the wavelength of the laser is relatively long, the field can be assumed constant during this step. The field changes direction, accelerating the electron (the blue curve is the path of the electron) only to return to the ion, where it recombines and a photon with high energy is emitted.*

- I The atomic potential is severely distorted, enabling a bound electron to tunnel out of the potential at a time  $t_0$ . If the wavelength of the laser is relatively long, the field can be assumed constant during this step.
- II The free electron is now subjected to the linearly polarized laser field, modeled as a sinusoidal electric field  $E = E_0 \sin(\omega t)$  with amplitude  $E_0$  and angular frequency  $\omega$ . The electron will be accelerated by said field, and if the electron has no initial velocity at  $t_0$ , the subsequent trajectory

can be derived as:

$$x(t) = \frac{eE_0}{m\omega^2} \left( \sin(\omega t) - \sin(\omega t_0) - \omega(t - t_0) \cos(\omega t_0) \right) \quad (2.3)$$

The electron mass and charge are denoted  $m$  and  $e$  respectively. The electron follows an oscillatory motion and depending on the time of ionization  $t_0$ , it might travel back and meet the parent ion (i.e. cross  $x = 0$ ) at a time  $t_r$ . At this point, it will have gained an energy  $E_r$ :

$$E_r = 2U_p (\cos(\omega t_r) - \cos(\omega t_i))^2 \quad (2.4)$$

The *ponderomotive energy*,  $U_p$ , is the cycle-averaged kinetic energy of the oscillating motion of an electron in the field:

$$U_p = \frac{e^2 E_0^2}{4m\omega^2} \propto \lambda^2 I \quad (2.5)$$

III There is now a possibility of the electron recombining with the parent ion, in which case a high energy photon will be emitted, the energy of which will depend on the path of the electron and on the ionization potential,  $I_p$ , of the atom. The maximum photon energy, also called the cut-off energy, is given by:

$$E_{\hbar\omega} \leq I_p + 3.17U_p \quad (2.6)$$

Since the cut-off energy depends on  $U_p$ , the maximum photon energy achievable with HHG increases linearly with intensity and quadratically with wavelength. Moreover, there is a wide spectrum of possible photon energies, depending on the path of the electron, meaning a broad range of frequencies in the XUV-region is emitted in a single half-cycle of the laser field. Since the laser field is sinusoidal, and the direction of the field irrelevant, the process of photon emission will be repeated twice per cycle. Due to this symmetry, radiation of even frequency-multiples of the laser photon energy (i.e. even harmonics) will be emitted with opposite phase from one half-cycle to the next, thus canceling each other, while those at odd multiples will have the same phase. The

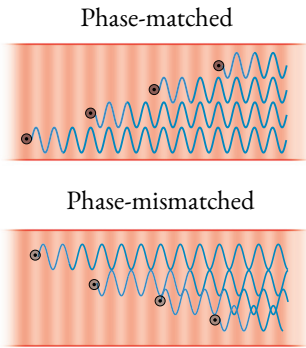


Figure 2.9. In a phase-matched medium, the light is emitted in phase and the sum of the light increases quadratically with the length of the medium. A mismatch of emission phase leads to an oscillation intensity of the output.

time-integrated field will then only exhibit odd-order frequency-multiples of the fundamental laser frequency  $\omega$ . The  $2\omega$ -spacing can also be understood by recalling the time-scaling property of the Fourier transform, where  $\alpha$  is 2 in this case:

$$f\left(\frac{t}{\alpha}\right) \iff \mathcal{F}(\alpha\omega) \quad (2.7)$$

All of the above mentioned predictions are seen experimentally [26]. The model is however limited to the response of a single atom, while the experimentally measured light is the result of an enormous ensemble of atoms emitting the light together. The properties of the resulting light will therefore also depend on the phase relation between each individual atomic response. To further explain what is measured experimentally, we need to look at the macroscopic effects of HHG.

### 2.2.2 HHG - macroscopic picture

It is not trivial to answer whether the atoms should emit the light in phase or not, but since we experimentally measure the generated light, we know that the emission of each atom must add more or less constructively. The issue of optimizing the emission process depends largely on this *phase-matching*, and the problem is visualized in figure 2.9. The intricate details of phase-matching are beyond the scope of this work, but its importance should not be understated. By knowing what circumstances affect the phase-matching, we have more control in shaping the generated light to our preference. The total phase-mismatch,  $\Delta k$ , depends on four contributions [27–31], where a perfect phase-matching corresponds to  $\Delta k = 0$ . Since the different contributions bear different signs, it is theoretically possible to minimize the mismatch. To achieve this experimentally, we can affect these contributions by modifying the gas pressure in the focus, the position of the focus and the intensity of the laser beam. Since HHG involves many parameters, the optimization is achieved through a recursive procedure, monitoring the output while modifying the conditions.

As was shown in the three-step model, the process of generating high harmonics is best understood in the time domain, i.e. by following the events of the atomic distortion at different

times in the electric field. The light generated from HHG however is most conveniently treated in the frequency domain, i.e. in a time-integrated picture, where the *spectral* amplitude and phase are studied. Since we measure the frequency spectrum of a signal with a photon or electron spectrometer, it is a natural choice.

In the following chapters we will often switch between the time- and frequency-domain to describe the measurements, but also to describe the dynamics of what we measure. In light of this, we will take a moment to discuss the time-frequency relation of the generated attosecond pulse train (APT).

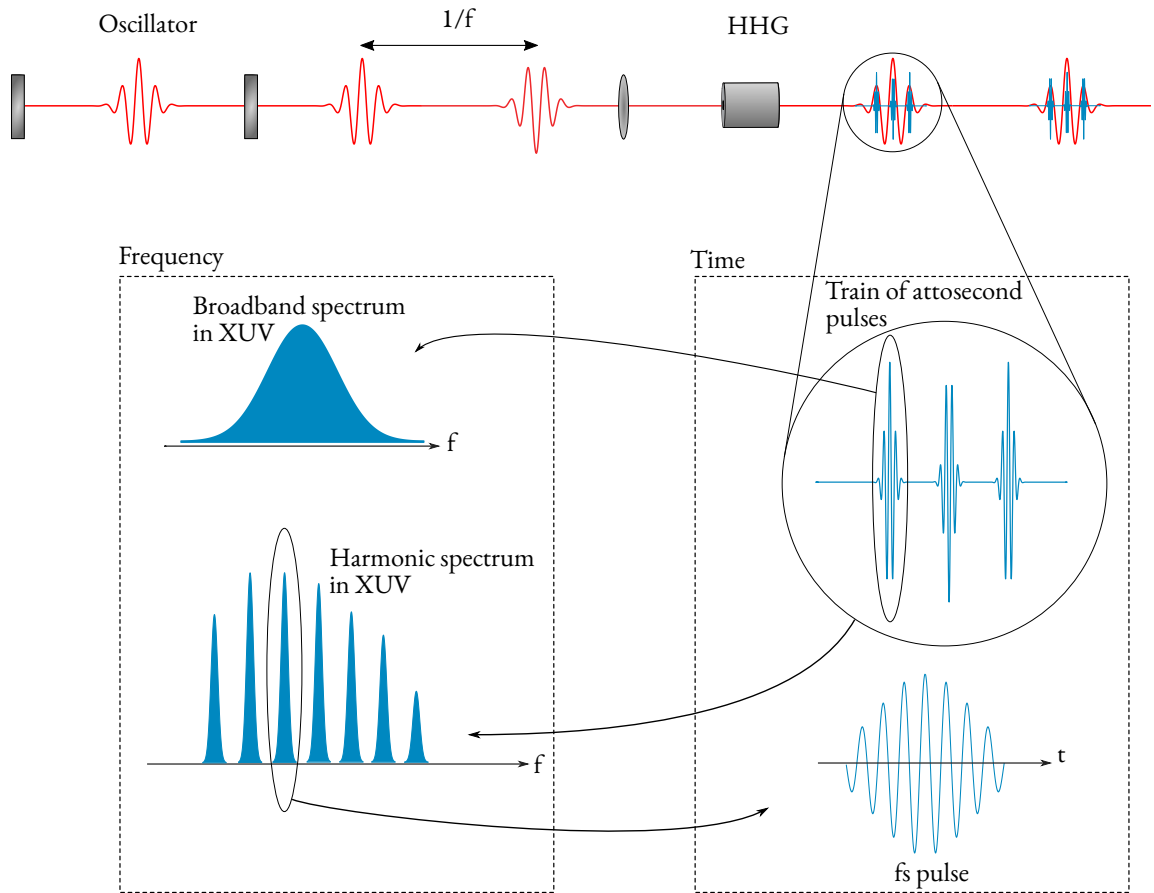


Figure 2.10. Relation between the pulses generated in the oscillator, the pulse trains generated from HHG and individual pulses in the train.

In a mode-locked oscillator there is a pulse traveling between the

two end mirrors, arriving at the output mirror with a frequency of  $f_{rep} = c/L_0$ , which depends on the oscillator length  $L_0$ . This means that the emitted pulses are separated in time by  $1/f_{rep}$ . As we discussed before, these pulses are amplified by several orders of magnitude before they are focused into a gas cell, generating high order harmonics. This sequence is seen in the top of figure 2.10, where the pulses are depicted in time. Beneath, we see a zoom-in of the train of attosecond pulses, which is generated in the gas cell. The interference of all pulses in the train is what leads to the characteristic harmonic spectrum, where each odd-order peak is separated by  $2\omega$ ,  $\omega$  being the frequency at the central wavelength of the fundamental pulse emitted from the oscillator. If we were to separate a single pulse in the train, which is possible via different methods of gating [32, 33], we get a broadband spectrum in the XUV. If instead we separate\* a single harmonic peak in the frequency domain, a pulse of femtosecond duration in the time domain emerges.

\*Via for example a refraction grating, spatially separating the harmonics.

With this in mind, let us have a closer look at the relationship between the spectral intensity and the temporal intensity in the train. In figure 2.11, the harmonic intensity and spectral phase are plotted on the left hand side, while the corresponding intensity of the APT is plotted on the right hand side. In the top of the figure, the phase across the full spectrum is flat\* and the corresponding pulse train is said to be *Fourier limited*. Both the individual pulses and the train is at their shortest duration, given a certain spectral intensity. The colors depict that a single harmonic corresponds to a femtosecond pulse and inversely a single pulse in time corresponds to a broad spectrum (only true for a Fourier limited pulse). In the middle, a quadratic phase relation between the harmonics have been introduced, and the individual pulses in the train are, as a result, not Fourier limited anymore. This phase relation is referred to as the *atto-chirp*, since it affects the attosecond pulses themselves. As seen, the phase of each harmonic order is still flat, they are just offset to each other in a quadratic manner. In the bottom of the figure the inter-harmonic phase is flat, while the intra-harmonic phase is now quadratic, a change which only affects the pulse train length, not the individual pulses. This phase is referred to as the *femto-chirp*, seeing as it affects the whole pulse train which has similar duration to the femtosecond pulses they are generated from.

\*I.e. all frequencies are in phase.

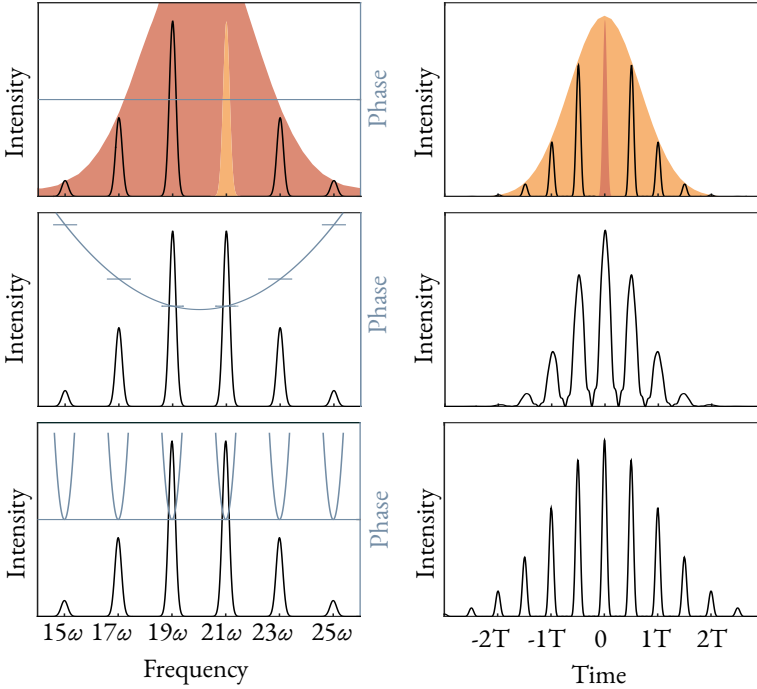


Figure 2.11. *Time-frequency relation in the pulse train. each frequency has a corresponding phase, essentially telling is when in time the frequency arrives related to the other frequencies. A flat phase relation across the full spectrum results in a pulse train of short pulses. If the phase is then varying inter-harmonic (middle) or intra-harmonic (bottom) the individual pulse (middle) or the length of the train (bottom) is affected.*

Using the three step model described earlier, we can derive a simple formula for the phase relation of the harmonic peaks [34]. An approximate expression for the return time of the electron as a function of emitted frequency,  $t_r(\Omega)$ , is obtained by examining how equation 2.4 vary as a function of  $t_r^*$ . Since  $\Omega = d\phi/dt$ , where  $\Omega$  is the frequency, the spectral phase  $\phi(\Omega)$  is determined by an integration of the return time, and the phase difference between two neighboring harmonics can then be approximated by:

$$\Delta\phi_q = \frac{4\gamma}{I} (q - q_p)\omega^2 \quad (2.8)$$

where  $\gamma$  is determined numerically in reference [34]. The attochirp is then  $\tau_{XUV} = \Delta\phi_q/2\omega$ , which varies linearly with harmonic order.

\*For a complete derivation, see reference [34]



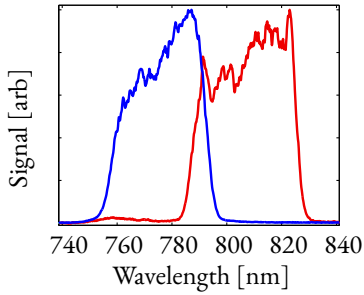


Figure 2.12. Output from a fiber-spectrometer, showing the two extremes of the tunable range when the bandwidth is limited.

\*This filter uses sound waves to manipulate the different frequencies of the pulse

## 2.3 THE HHG SETUP IN LUND

As the concepts of femtosecond and attosecond pulse generation have been introduced, we will turn our focus to the technical part of achieving HHG and what settings we can adjust to control the output to suit our experiments.

The laser chain is seeded by the commercial oscillator, model «Rainbow» from *Femtolasers*, where pulses of 7 fs duration are generated from a mode-locked Ti:Sapphire cavity. The pulses, originally of 2.5 nJ, are then stretched using the grating configuration of reference [35] and sent through an AOPDF [36] (*Acousto-Optical Programmable Dispersive Filter*)\* of model «Dazzler» from *FaStlite*. This filter can, if wanted, shape the spectrum of the pulse to produce a more narrow bandwidth, and additionally shift the central wavelength of the spectrum. The tunable range of the laser is seen in figure 2.12. This allows for, in turn, a tuning of the harmonic spectrum generated from the manipulated pulse. A narrower laser spectrum corresponds to a longer pulse in time, which in turn means that a longer train of attosecond pulses is generated by HHG, making the harmonics more narrow themselves (see figure 2.11). Shifting the central frequency by  $\delta\omega$  causes a shift of the harmonic spacing by  $2\delta\omega$ . The  $N^{th}$  harmonic then moves by  $N\delta\omega$ , allowing for a fine-tuning of the harmonic energies.

When the full bandwidth is used (100 nm), the filter operates only as an error-correction device, compensating for phase disturbances which are inevitably introduced throughout the laser chain.

The pulses are then sent through multiple stages of amplification. A short and concise schematic flowchart of the stages is seen in figure 2.13. Two pulsed diode lasers (green arrows) pump four different Ti:Sapphire crystals at a repetition rate of 1 kHz. After initial amplification to 250 nJ in the *Multi-pass* amplifier, the pulses travel 14 times through the crystal in the *Regenerative* amplifier, to an energy of 0.5 mJ. In the last two amplification stages the pulses pass two Ti:Sapphire crystals three times each, the latter being cryogenically cooled by liquid helium, to a final energy of 10 mJ. The pulses are then compressed with a grating pair as described in reference [37] to a Fourier limited duration of 20 fs if the full bandwidth is used.

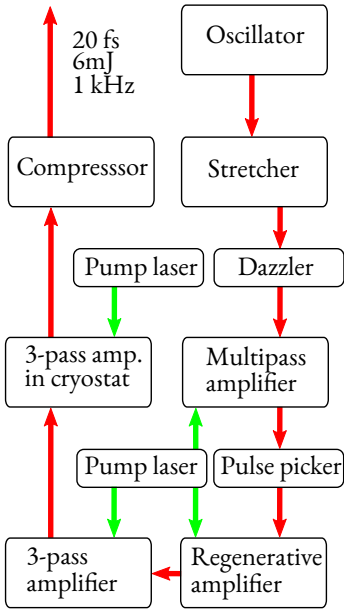


Figure 2.13. A flowchart of the 1 kHz laser in Lund. The pulse to be amplified is shown in red, the pump lasers in green.

The amplification chain is a quite sensitive system, so to ensure that the pulses are always of the specified duration and energy, a variety of diagnostic tools are connected to the chain. A «Wiz- zler» is used to measure the pulse duration in real time, and the measured spectrum can be fed back to the «Dazzler» to apply corrections to the amplitude and phase of the spectrum. Rougher corrections are applied to the grating angles in the compressor.

The pulses, or laser beam (these two descriptors will be used interchangeably to refer to the femtosecond laser output), are then directed to a vacuum chamber approximately 5 meters away. A small angular deviation results in a substantial spatial move- ment after 5 meters of travel, which is why the beam-stabilization system «Aligna» from TEM is used to correct for variations in the pointing of the beam at the entry of the HHG setup. It reads the position and angle of the beam at a 100 Hz, correcting small movements with piezo-actuators on two mirrors and larger move- ments with stepper motors. The beam is focused, using a spher- ical mirror with a focal length of 50 cm, down to a spot size of 86 micron. The focus spot is placed, after entry into a vacuum chamber, inside a small cavity with an opening of 1 mm, which is fed with gas using a pulsed valve. Before the pulse passes through the cavity, the valve opens and fills the cavity with a gas of *he- lium, neon, argon* or *xenon*. The intensity in the focus region is estimated to be  $4 \cdot 10^{14}$  W/cm<sup>2</sup>, high enough to generate an attosecond pulse train. The intensity can be varied by limiting the beam size before the focusing mirror, an action which will also change the focusing properties of the beam, or by limiting the power with a half-wave plate and a polarizer, which will add\* some dispersion to the femtosecond pulse.

The APTs\* are then focused into a target chamber, where the devices detailed in *Chapter 3* are mounted. The beam is then directed towards an XUV spectrometer for diagnosis. The prin- ciple of the spectrometer is seen in figure 2.14. The XUV beam hits a grating, which refracts the wavelengths of the attosecond pulse trains into different angles, causing a spatial separation of the harmonic orders. Longer wavelengths are refracted more, shorter less. The separated harmonics are focused in the vertical direction onto an MCP (*Multi-Channel Plate*), consisting of tiny metal channels which amplify the signal. Given that HHG is a very inefficient process, only about a millionth of the energy is

\*This can be pre-compensated for.

\*Alternatively «harmonics» or «XUV beam/pulses», all are used interchangeably

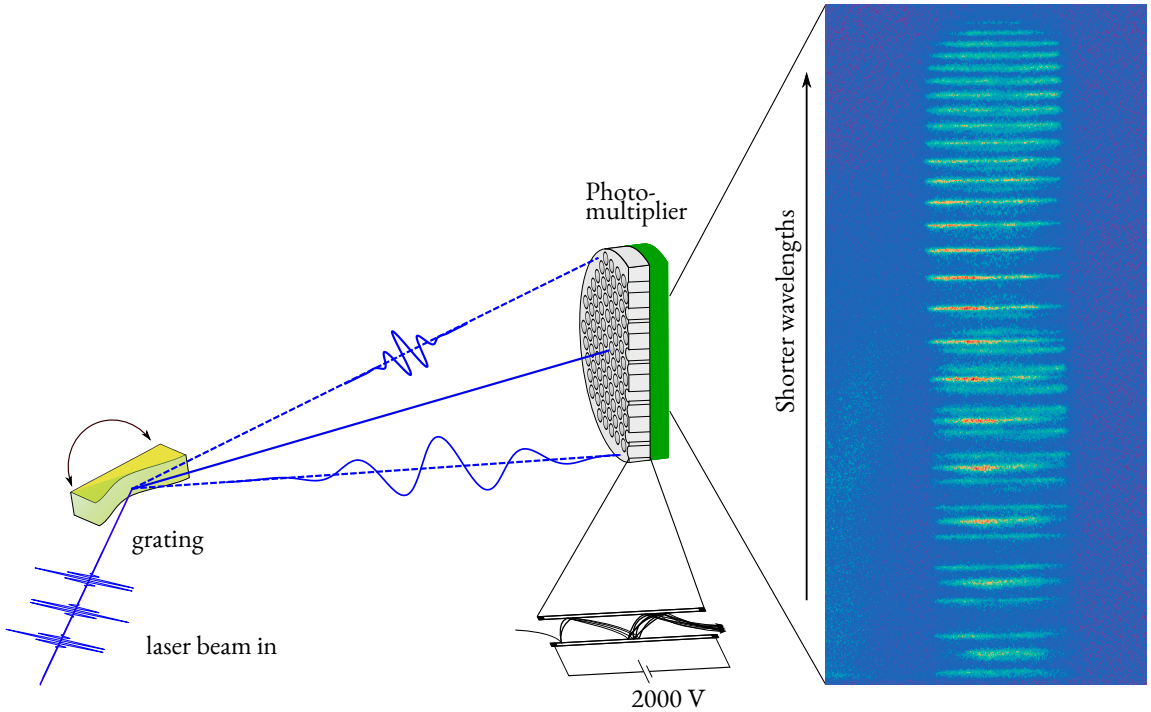


Figure 2.14. Schematic image of the XUV spectrometer. The attosecond pulse trains are refracted on a gold grating, which separates each harmonic in space onto a photo-multiplier. The resulting image from the phosphor-screen is captured by a camera.

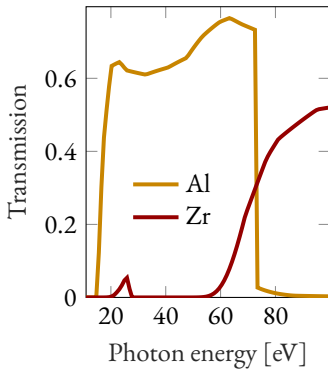


Figure 2.16. Transmission in the XUV region of an aluminium- and zirconium-foil with 200 nm thickness.

converted at best [29], the XUV light needs amplification to be seen. At the end of the MCP the electrons hit a phosphor screen, which will fluoresce as the electrons arrive. The fluorescing image is captured, as seen in the figure. The XUV spectrometer is mainly used for feedback of the harmonics in order to optimize them for a certain experiment. An experimentally measured spectrum generated in neon is shown in figure 2.15.

Metallic filters in the XUV path shape the harmonic spectrum in a very predictable way, while absorbing the fundamental. A 200 nm thin foil of *aluminium* has a transparency of almost 60 % in the region between 10 and 72 eV, with a very sharp definition. For a high pass filter, *zirconium* is often used, absorbing harmonics below 60 eV. See figure 2.16 for the transmission curves in the XUV region.

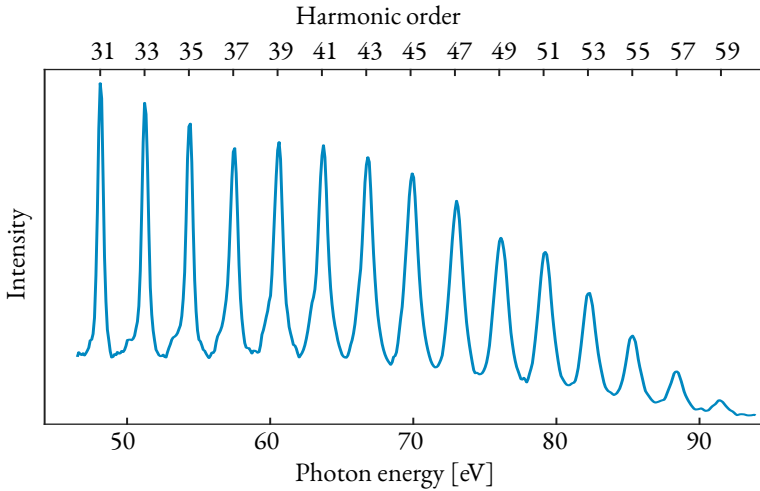


Figure 2.15. The image of the phosphor-screen is summed across its non-dependent axis, and the wavelength axis is converted to frequencies (photon energy). The spacing between each harmonic is now about 3.1 eV and the calibrated harmonic order is seen above. The spectrum was generated in neon. The cut-off is reached at 90 eV. There are more harmonics generated below 50 eV, they are just not able to fit onto the MCP all at once.

## 2.4 SUMMARY

In this chapter we have seen how we can create light with some very unique properties. Through a process called HHG, we can generate light bursts which are *coherent*\*, of unparalleled ultra-short duration and with energies in the extreme ultraviolet region closing in on the soft X-ray region. This region of light frequencies is extremely useful in spectroscopic applications, since it is able to excite the outer and inner shells of a wide range of atoms and molecules, not possible with normal laser light\*.

Now we will see how this light can be used to follow some electronic processes in real-time using an interferometric technique and deploying time-frequency analysis.

\*i.e the phase relation between the frequencies is well-defined

\*For example 800 nm corresponds to 1.55 eV. Only a high order process can ionize an atom.





# CHAPTER 3



## Interferometry with Photoelectrons

*Interferometry is an extremely powerful technique, which typically makes use of the short wavelengths of visible light to measure minuscule displacements and durations otherwise impossible to detect. An interferometer is conceptually a very simple device, it can consist of as few as three reflective elements and an eyepiece, and lends its use in all of science. A length change of a single nanometer, equal to the width of 10 atoms, is easily detectable even with our own eyes. This is possible though the interference of light waves. In this chapter, we will not only discuss interferometry with optical light, but also with matter waves using a quantum interferometer.*

- 3.1 Photoionization
- 3.2 Detecting photoelectrons
- 3.3 Photoelectrons - the footprints of the photon and atom
- 3.4 The Interferometer in Lund
- 3.5 Summary

---

### 3.1 PHOTOIONIZATION

**N**EGATIVELY or positively charged ions are produced when one or more electrons are absorbed or emitted from an atom or molecule. For an electron to be absorbed, there has to be a free electron available close-by. To remove an electron, we need to supply enough energy to overcome the attraction of the nucleus, referred to as the *atomic potential*. This can be done via energy transfer from either charged particles or photons. The event of the latter is what is

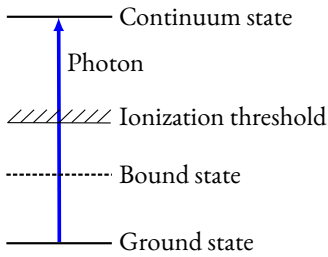


Figure 3.1. An electron transitions to an unbound state by interacting with light. The energy of the photon determines the final state.

\*i.e. the velocity

\*in spectroscopy this probability is called the *cross-section*, the larger the cross-section the larger the "hit area" for an impinging photon

called *photo-ionization*. As was stated in *Chapter 2*, most light results from electron relaxation, when an excited electron relaxes to a more bound energy state, releasing its excess energy in form of a photon. The reverse process is simply *photo-excitation*, and if the atom is ionized in the process we refer to it as photo-ionization. The released electron is called a photo-electron and its detection can give us insight into the system it was released from. We often want to investigate an atom at rest, but at the same time we need to disturb it to create a photoelectron. Gathering information about an atom at rest might seem like an impossible task then, but through some basic assumptions and an extensively tried theoretical framework it is possible.

If we were to generate light with a fixed energy of  $E_{ph}$  and focus it into a volume of atoms of a single element while measuring the kinetic energy\* of all the electrons that are released, we would make two observations: the energy of the electrons differ from  $E_{ph}$  by a constant value; the amount of electrons released and their energy offset depends on the atomic species. Furthermore, if the photon energy,  $E_{ph}$ , is continuously increased, the energy offset might suddenly change, as will then the electron yield. This tells us that the electrons are distributed into discrete, *quantized*, shells with a certain probability\* of absorbing a photon. If we observe the directions that the electrons are released in, we will not always see a uniform pattern: some directions might be more favored than others, depending on the atomic species and which energy level is ionized (the polarization of the light also plays a role). The electronic states of the atom are not only configured into discrete energy levels, they are also configured into certain rotational distributions around the nucleus. This property is referred to as *angular momentum*. By measuring the momentum of the released electrons, which includes measuring the angle of emission and the velocity, we gain full insight into the electronic state it originated from.

One of the first indications of a light quanta (i.e. the photon) came from an experiment by Hertz in 1887 [38]. The detected phenomena, the *photoelectric effect*, was later theoretically described by Einstein in 1905 [39]. This model of a light quanta, along with the atomic model of Bohr from 1913 [40], contributed immensely to the subsequent development of quantum mechanics.

The quantum mechanical model of photoionization is visually explained in figure 3.1. A ground state, the lowest energy electron configuration of the atom, is excited by a photon with an energy exceeding the ionization threshold of the least bound electron. The electron undergoes a transition to a state not bound by the atomic potential any longer. The electron will therefore escape the atom as time progresses with a kinetic energy  $\varepsilon = E_{ph} - I_p$ . The probability amplitude,  $c_{\varepsilon}$ , of this transition, after the interaction is over, can be written as [41]\*:

$$c_{\varepsilon,l}^{(1)} = \frac{e}{i\hbar} \underbrace{\langle \varepsilon_l | \hat{r} | g \rangle}_{\text{dipole}} \cdot \underbrace{E_{\text{XUV}}(\Omega)}_{\text{light frequencies}} \quad (3.1)$$

\*according to first-order time-dependent perturbation theory

where  $|g\rangle$  denotes the ground state,  $|\varepsilon_l\rangle$  the final un-bound state with angular momentum  $l$ , and  $\hat{r}$  the *electric dipole operator*. The latter describes the interaction between the electric field component of the xuv light and the charge separation (*dipole*) of the atom. There are other forms of transitions possible via other modes of charge separations, but these are far less likely. The term noted *dipole* above tells us which dipole transitions are possible. Only those transitions that change the angular momentum by  $\pm 1$  are possible, stemming from the fact that a photon carries angular momentum and the total angular momentum has to be conserved. Since the probability also depends on the xuv spectrum, we expect the distribution of photoelectrons to mimic that of the xuv spectrum. This means that the frequency comb of an attosecond pulse train will be imprinted on the photoelectron spectrum, originating from the interaction of said pulse with an atomic ensemble. This important relation will be utilized later on.

Now we know what properties a photoelectron will possess after ionization by an xuv pulse. We will now look at how to detect and measure these properties of the electrons to gain new insight into some dynamical processes induced by photoionization.

## 3.2 DETECTING PHOTOELECTRONS

The device used to detect and measure the kinetic energies of photoelectrons is often called a *spectrometer*, since we measure the



spectrum of energies of the electrons. Here, an overview of the two spectrometers used in *Papers II, III, IV and VI* is given. As can often be the case, there is no single spectrometer which suits every possible experiment. Some preferences are often competing against each other, and often one has to sacrifice one aspect in order to excel in another. However, they all need to support an ultra-high vacuum environment. The techniques below, known as MBES and VMIS, are two complementary techniques, the former focusing on signal strength and energy resolution while the latter includes angular resolvability while suffering in energy resolution.

### 3.2.1 Magnetic Bottle Electron Spectrometer

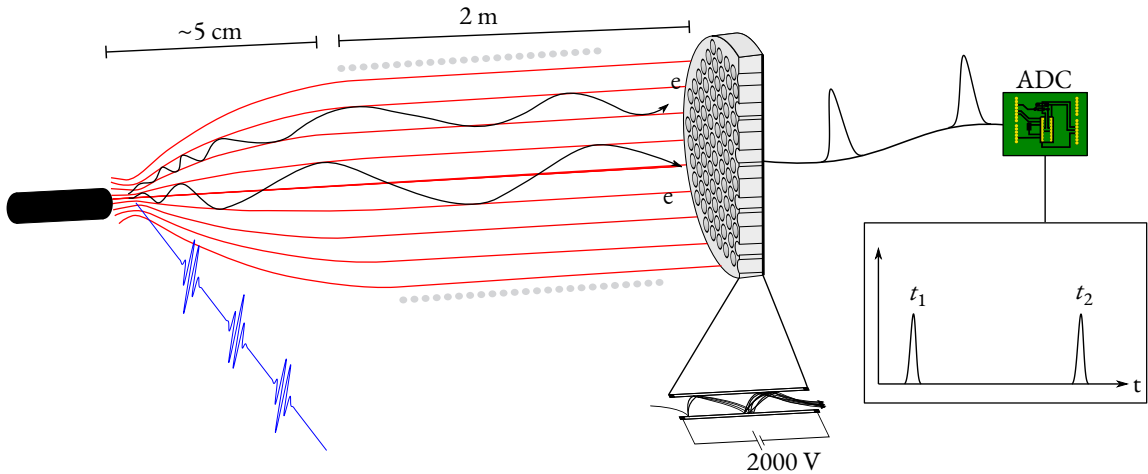


Figure 3.2. Schematic illustration of an MBES. The magnetic field lines which results from the permanent magnet (black cylinder) and the solenoid (gray dots) are shown in red. An electron which is created in a region close to the magnet will be forced towards the electron multiplier in a wiggling motion. The voltage spike is detected by an Analog-to-Digital-Converter.

The *Magnetic Bottle Electron Spectrometer*, or MBES, is a *Time-of-Flight* (ToF) spectrometer, meaning it measures the time it takes the electrons to travel a known distance. Since the electrons will have kinetic energies in the region of 100 eV, they can be treated classically and their kinetic energy is simply  $E_{kin} \propto \frac{L^2}{t^2}$

where  $t$  is the flight time and  $L$  the length the electrons travel, from the point they are created to the point they are detected. An electronic signal is generated from a photo-diode when the laser pulse exits the laser chain, which can be thought of as the start signal. A second signal is generated when an electron hits the detector: an electron-multiplier (a *Multi-Channel Plate*). The MCP generates a detectable voltage from a single electron, through a cascading collision process in the array of thin tubes, releasing millions of secondary electrons in the process. The second signal marks a stop signal, and the time difference is then a measure of the time-of-flight of the detected electron.

There are different methods of directing the electrons created in the *interaction region*, where for example an attosecond pulse train ionizes a gas target, to the sensitive area of an MCP, where they will be detected. An MBES uses an inhomogeneous magnetic field to collect as much as 90% of all electrons. The MBES used in this thesis work was based on the design from reference [42], and a description of the technique is seen in figure 3.2. A strong permanent magnet (0.23 T) with a conical pole directed towards the interaction region, generates a divergent magnetic field which acts as a magnetic mirror for all electrons. A magnetic field will exert no work on the electrons since the force is always perpendicular to the field lines. If the lines are curved inwards, as they are close to the tip of the magnet, there will be a force component pointing in the other direction, essentially "reflecting" electrons which happened to be traveling away from the detector. The divergent field soon meets the homogeneous field generated by a solenoid, which encapsulates a tube with external magnetic shielding. Over the length of a few centimeters, the field lines become parallel and the collected electrons are traveling in helical motion towards the detector, their initial velocities practically unmodified.

It is easy to imagine two electrons, with the same energy, being released in complete opposite directions. Ideally, these would be measured to have the same flight time, but since one electron needs to turn around while the other one is already traveling towards the detector, they will reach the MCP at slightly different times, more so at higher kinetic energies. This effect can be minimized by putting a large negative voltage on the magnet and an identical positive voltage on the entrance to the flight

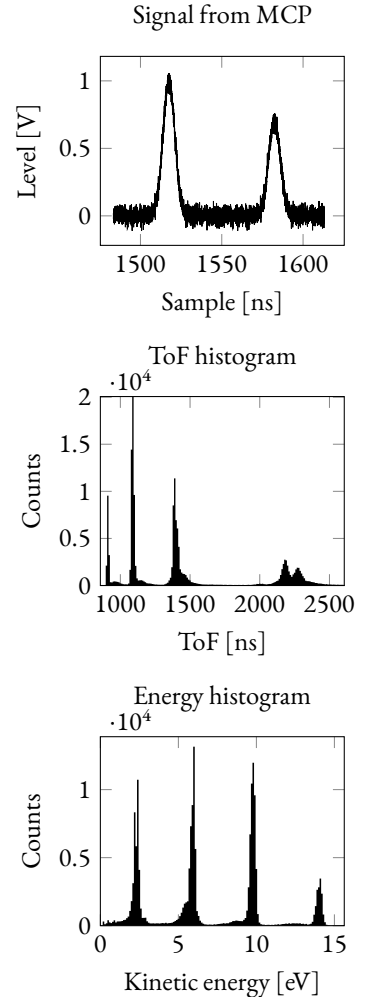


Figure 3.3. *Top: The voltage spike from the MCP is sampled with an ADC. Middle: Each peak arrival is collected in a histogram. Bottom: The time-of-flight histogram has been transformed to an equal-width binned kinetic energy histogram.*

tube, essentially accelerating the electrons swiftly away from the magnet before they are decelerated as they reach the flight tube.

Let us again imagine two electrons, collected from two different atoms in a gas target ionized by a single attosecond pulse train. The laser pulse itself triggers the timer of an *Analog-to-Digital Converter* (ADC) to start counting. The fastest electron naturally hits the MCP first, creating a small electronic pulse which is measured by the ADC. A couple of hundred nanoseconds later the second electron might hit. The electronic signal is seen in the top of figure 3.3. The ADC records the split times of the different arrivals. This process is then repeated and collected in a histogram which shows the distribution of electron flight times. In the middle of figure 3.3, a collection of electron flight times from roughly 120 000 laser pulses (2 minute acquisition at 1 kHz). At this point, the harmonic structure is clearly visible. Due to the non-linear relation between time-of-flight and kinetic energy, the even spacing is not present yet. Using equation 3.2 [43] we can easily transform the histogram to show the equivalent kinetic energies,  $E_{kin}$ , as seen in the bottom of figure 3.3.

$$E_{kin} = \frac{m}{2e} \left( \frac{L}{t + t_d} \right)^2 + E_{offset} \quad (3.2)$$

The length,  $L$ , of the flight tube is 2 m in this case,  $t$  is the ToF and  $t_d$  is included to account for any electronic delay in the transfer of the signals. The mass and charge of the electron are denoted  $m$  and  $e$  respectively. The kinetic energy spectrum can be offset by an acceleration/deceleration voltage,  $E_{offset}$ , to move a specific part of the spectrum to the slow kinetic energy region between 0-2 eV. As seen in the ToF histogram in figure 3.3, a given harmonic peak is sampled much more finely at long flight times (i.e. low kinetic energies) than at fast flight times, meaning the resolution is optimal at long flight times. The non-linear relationship also means that extra care needs to be taken when transforming the histogram. A direct conversion of each ToF bin to energy results in a non-uniform width of the energy bins. For equal-width energy bins, an interpolation method needs to be adopted to preserve the total number of counts in the transformation. The method is illustrated in figure 3.4. An energy axis with equal-width energy bins is created, spanning energies between those corresponding to the minimal and maximal ToF (or a smaller

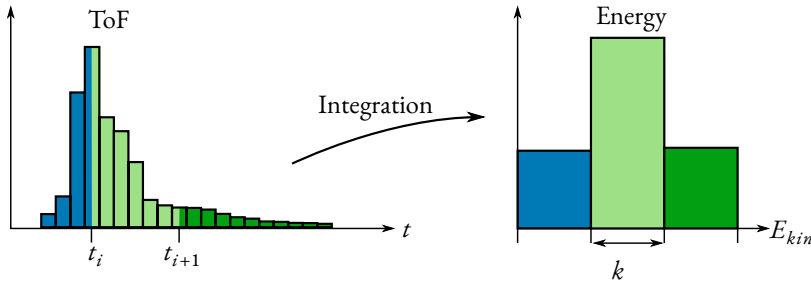


Figure 3.4. In order to produce a true-count energy histogram with bins of equal width from the ToF histogram, an interpolation method has been used. Each color represents the transferred counts. The counts between  $t_i$  and  $t_{i+1}$  corresponds to energy bin  $k$ .

interval if desired). For each energy bin  $k$ , the ToFs  $t_i$  and  $t_{i+1}$ , corresponding to the beginning and end of the energy bin, are calculated. As the figure shows,  $t_i$  and  $t_{i+1}$  will most probably not line up with the bin intervals in the ToF histogram. The counts at  $t_i$  and  $t_{i+1}$  are interpolated from the nearest ToF bins, and the integrated signal is put in energy bin  $k$  till the entire energy range is covered.

The obvious advantage of the MBES is the high collection efficiency, leading to a high quality\* signal, and the long flight times resulting in a high resolvability at low kinetic energies. Due to the magnetic mirror, we lose the ability to determine the emission angles of the electrons. For some experiments, this is an acceptable loss. In *Papers II* and *III* we used an MBES to take advantage of its excellent energy resolution.

\*i.e. high signal-to-noise.

In the next section, we will discuss a technique to determine the emission angles of the photoelectrons.

### 3.2.2 Velocity Map Imaging Spectrometer

A *Velocity Map Imaging Spectrometer*, or VMIS, uses high electrostatic fields to accelerate the electrons onto an imaging MCP. A fluorescent phosphor screen placed behind the MCP converts the electrons into visible photons, allowing the image to be captured by a camera.

The *Repeller* and *Extractor* plates, seen in figure 3.5, acts as a velocity lens. The potentials on the plates, usually on the order of 5000 V, can be chosen such that the position of an electron hitting the MCP is directly proportional to its transverse velocity,

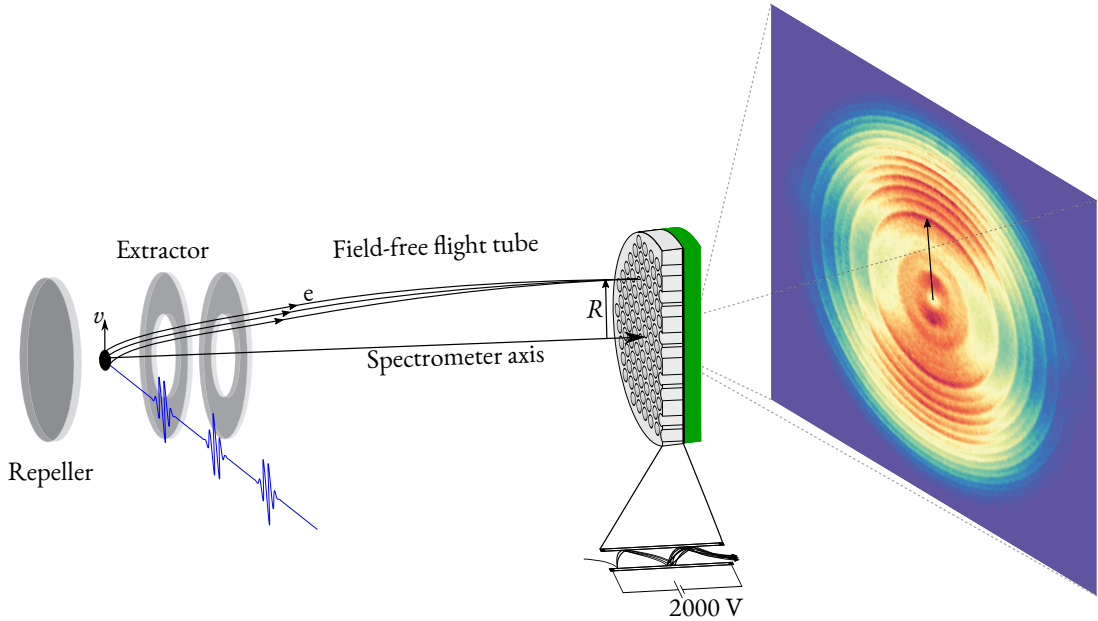


Figure 3.5. A VMIS uses a clever combination of two electrostatic fields to map the initial velocity component,  $v$ , perpendicular to the spectrometer axis, to the final position,  $R$ , on the position sensitive detector. The angle of emission in the transverse plane then corresponds to the angle of detection. A raw image from the phosphor screen is also shown.

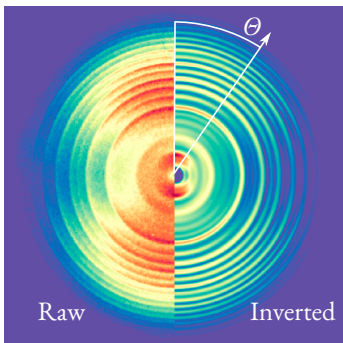


Figure 3.6. A comparison of the raw image and an inverted, using the inversion technique in reference [45]. The harmonic structure is clearly visible. In this case the photoelectrons are more prone to be emitted in the direction of the polarization of the xuv light (vertical). The angle  $\Theta$  is illustrated.

$v$ , upon emission, regardless of its position in the interaction region [44]. The radius,  $R$ , of the resulting image is therefore a measure of the transverse kinetic energy component, as equation 3.3 shows:

$$E_{kin} = qV \frac{R^2}{L^2} \quad (3.3)$$

while the angle  $\Theta$  is a measure of the angle of emission in the transverse plane, or the transverse *component* of the momentum vector in any other plane. Since the electrons are accelerated to a few 1000 eV, the longitudinal component is practically lost.

In order to study the angular distribution of the photoelectrons, we need a measure of the probability of finding an electron in a solid angle  $d\Omega$ , which we will denote  $d\sigma/d\Omega$ . This *differential photoelectron cross section* can, for ionization by a single photon, be expressed by a surprisingly simple formula [46]:

$$\frac{d\sigma}{d\Omega} = \frac{\sigma_{total}}{4\pi} \left( 1 + \frac{1}{2}\beta(3 \cos^2 \Theta - 1) \right) \quad (3.4)$$

Here,  $\sigma_{total}$  represents the total cross section,  $\Theta$  is the angle between the direction of the ejected electron and the polarization vector of the incident light. The so-called *asymmetry parameter*,  $\beta$ , is given for a certain initial state  $l$  (e.g., s, p, d, ...) and ranges from -1 to 2. For a complete formulation of  $\beta$ , see equation (2) in reference [46]. Here, it is sufficient to say that a  $\beta$  of «-1» corresponds to the electrons being released perpendicular to the polarization, «0» to a uniform distribution and «2» to electrons released parallel to the polarization.

The above equation is rotationally symmetric about the polarization axis, meaning the actual distribution is a 3D sphere around the interaction region. The 3D sphere is projected by the electrostatic fields onto the detector as a 2D image. If we are interested in the distribution *only* in the transverse plane, or any plane parallel to the polarization vector, an inversion procedure needs to be adopted. There are a number of procedures available with different strengths and weaknesses [45, 47, 48] regarding computation time and end-results. The procedure chosen in this thesis work is based on *pBasex*, described in reference [45]. In figure 3.6 the raw data is compared to the inverted image. In the inverted image, the radius  $R$  is a direct measure of the kinetic energy of the electron.

### 3.3 PHOTOELECTRONS - THE FOOTPRINTS OF THE PHOTON AND ATOM

While it is clear that the spectrometers just described would allow us to map the probability of photoionization and its energy dependence for a gaseous target atom, it is perhaps not as clear how we would follow photoionization as it unfolds, in real time. As figure 3.3 showed, the photoelectron spectrum shows the same harmonic structure as the XUV spectrometer measured. We recall that the characteristic spectrum arose due to the temporal interference of a train of attosecond pulses, where the harmonics are phase-locked to each other. A single pulse does not produce the same spectral comb. For the photoelectron spectrum to show

\*The electron wave action confined in time and space (recall figure 1.2)

the same behavior, the phase information must still be present in the photoelectron. The comb of peaks in the photoelectron spectrum is then a telltale sign of the wave-nature of the electron, suggested by deBroglie in 1924 [49]. Alas, this phase information is lost at detection as we convert the electron wave-packet\*, through repeated collisions in the MCP channels, to an intense electronic pulse. How should we go about to retrieve the phase?

A similar issue, namely the measurement of an ultrashort laser pulse in the visible and NIR region, was solved by employing an interferometric technique acronymized SPIDER, (*Spectral Phase Interferometry for Direct Electric-field Reconstruction*), which was introduced in 1998 [50]. It was needed since a femtosecond pulse cannot be measured simply by illuminating a photo-diode and observing the electronic signal, as the electronic response is too slow\*. The proposed technique instead made use of spectral interference of "sheared" pulses to obtain the phase of each frequency, after which the pulse could be reconstructed. Other techniques such as FROG [51] and *d-scan* [52] rely on second harmonic generation to retrieve the phase.

\*On the nanosecond timescale

In the XUV region, due to intensity and reflectivity issues, the same techniques cannot be applied. Methods that instead used atomic targets as mediators were then proposed [53, 54] to overcome these problems. In 2001, Paul and co-workers used a derivation of these methods to measure the relative phases of the harmonics generated in an argon gas, allowing them to reconstruct the average pulses in the pulse train and thereby confirming their attosecond duration [9]. They called this technique RABITT (*Reconstruction of Attosecond Burst by Interference of Two-color Transition*). In the next section, we will see how this technique can tell us not only the phase of the spectral comb, but also the phase of the electronic *transition* resulting in the photoelectrons: the key to following electron motion in real time.

### 3.3.1 Reconstruction of Attosecond Burst by Interference of Two-color Transition

In figure 3.7 we see an illustration of the underlying principle of RABITT. The attosecond pulse train was focused into a gas of argon atoms, and the photoelectrons were detected by the MBES described in the previous section. A negative voltage was applied

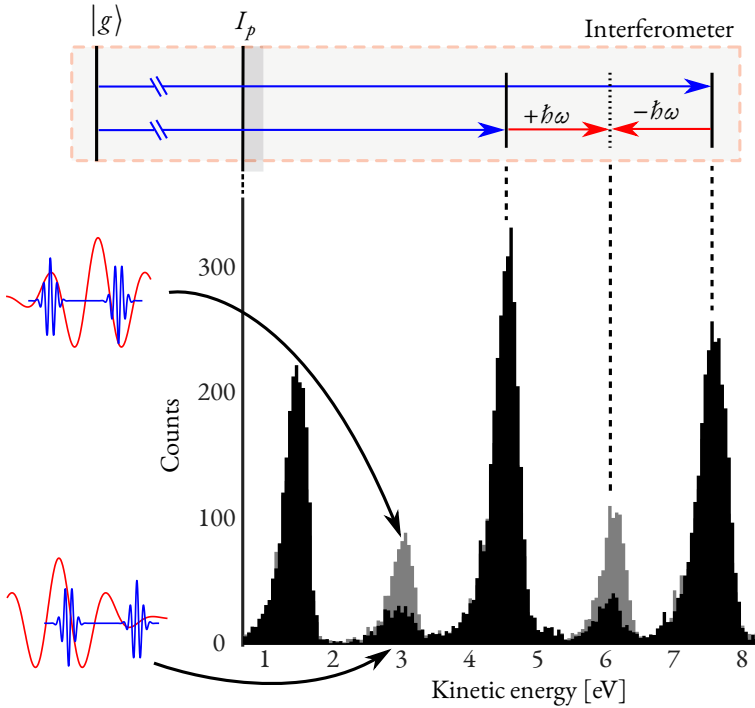


Figure 3.7. A photoelectron spectrum measured with an MBES. The harmonics were generated in an argon gas and focused into an argon target, giving rise to the three intense photoelectron peaks. If a weak replica of the generating IR pulse (red) is overlapped with the APT (blue) on target, photoelectron peaks at even orders appear due to two-photon transitions (top). The final state of the photoelectron can be accessed in two ways, leading to a phase-sensitive intensity of the side peaks (sidebands).

to the flight tube to decelerate the electrons. The photoelectron spectrum seen in the figure has been limited to only three harmonics in the post-processing of the acquired data. Above the photoelectron spectrum, a schematic energy diagram shows an atomic ground state,  $|g\rangle$ , being ionized by either of the two most energetic harmonics, illustrated by the blue arrows representing the photons. This process releases a photoelectron in the continuum with a kinetic energy of  $N\hbar\omega - I_p$ , where  $N$  is the harmonic order and  $\hbar\omega$  the photon energy of the fundamental frequency. The peaks in the measured spectrum are separated by a spectral distance of  $2\hbar\omega$  which, if the harmonics are generated by an NIR laser with a fundamental wavelength of 800 nm, corresponds to



an energy of roughly 3.1 eV.

If the attosecond pulse train is now overlapped in time and space with a weaker replica of the generating IR pulse (seen in red), there appears photoelectrons at the position of the spectrum corresponding to absorption of one harmonic photon and one IR photon. The relative intensity of these peaks, called *sidebands*, is dependent on the relative timing between the XUV pulse train and the IR pulse. In the figure, we see the sideband peak intensity at two different relative timings, referred to as *delay*, clearly showing the intensity variation. The harmonic intensity, only shown for one delay, decreases as the sideband intensity grows, owing to the fact that the number of photoelectrons is preserved. If we vary the delay in a controlled way and measure a photoelectron spectrum at each delay step, as was done in figure 3.8, we see a sideband intensity which is actually varying periodically with a frequency of  $2\omega$  (corresponding to a delay period of 1.3 fs at 800 nm).

\*via stimulated emission

This oscillation of the sidebands holds information about the spectral phase of the harmonic peaks. The sideband peaks appear when the released photoelectron, in the bold-line state in figure 3.7, either absorbs or emits\* an IR photon with frequency  $\omega$ . Owing to the odd-order spacing of the harmonics, there are then two pathways to the same final state, marked as a dashed line in figure 3.7. The intensity of the sideband depends on the total phase acquired during the transition from the ground state to the final state, essentially acting as an interferometer. The intensity can then be modeled from the interference of the two paths [19]:

$$I(\tau)_q = A_q + B_q \cos(2\omega\tau - \Delta\phi_q - \Delta\phi_q^{at}). \quad (3.5)$$

Here,  $q$  is an even integer and  $\tau$  is the relative delay between the pulses, which is controlled to high precision. The analytical formulation of  $A_q$  and  $B_q$  is not included here, since they carry no phase information, but the interested reader is referred to reference [55]. The phase difference  $\Delta\phi_q$  is defined as the difference between the phases of the neighboring harmonics,  $\phi_{q+1} - \phi_{q-1}$ . The phase  $\Delta\phi_q^{at}$ , strictly speaking, includes both the phase of the harmonic transition and the transition in the continuum induced by the IR. Since there are two unknowns but only one measurable ( $\phi = 2\omega\tau - \Delta\phi_q - \Delta\phi_q^{at}$ ) at each sideband, we have to make some

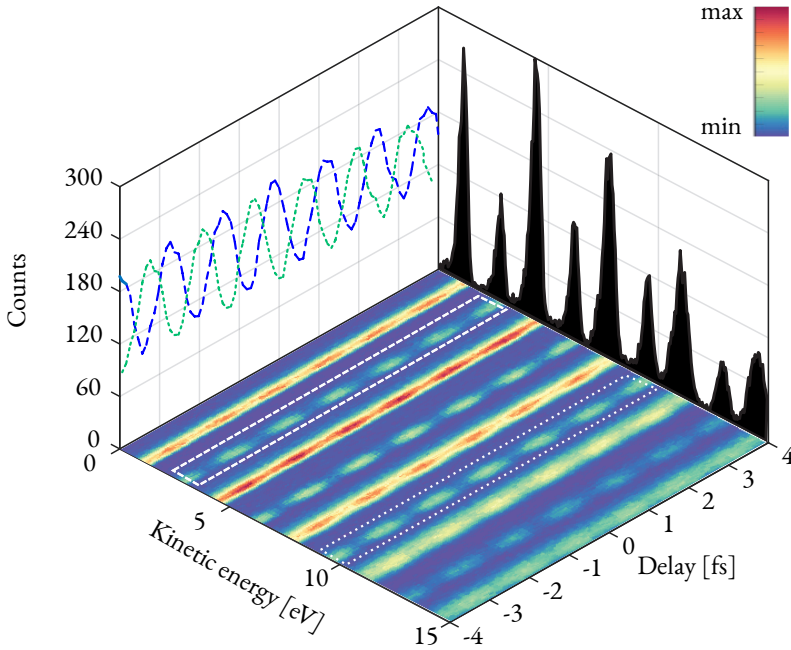


Figure 3.8. A false-color spectrogram of a RABITT measurement. The colorcode corresponds to the intensity of the spectrum at each delay (a single spectrum is seen projected in black). Two sidebands are summed across their spectral width and the intensity as a function of delay is seen in the projected plot to the left. Their inter-phase difference is exaggerated for visibility.

assumptions about either of the unknowns. These assumptions will be clarified in *Chapter 4*. In figure 3.8, the oscillations of two different sidebands are summed across its energy width and plotted as a function of the delay for two different sidebands. The phase difference, which is exaggerated in the projection for visibility, can be attributed to the atto-chirp of the harmonics (recall figure 2.11).

A successful implementation of the RABITT method, which provides us a quantum interferometer, requires a stable *optical* interferometer, since the delay between the pulse train and the IR replica needs to be controlled and varied with high precision. In the next section we will discuss the design of the existing optical interferometer for the laser setup in Lund, specifically aimed for the RABITT technique.

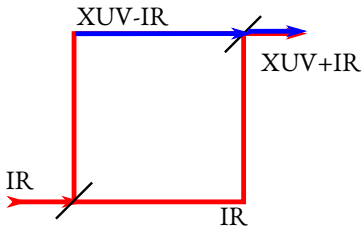


Figure 3.9. A simple sketch of a Mach-Zehnder interferometer incorporated into a RABITT setup. In one arm, the XUV pulse is generated while the IR is filtered out. The XUV pulse train is then recombined with the IR pulse from the other arm, allowing full control of the delay between the two.

\*A beam splitter is a semi-transparent mirror, reflecting and transmitting a certain percentage of the total power.

### 3.4 THE INTERFEROMETER IN LUND

In order to achieve an oscillating sideband intensity, we need to be able to control the delay between the pulse train and the IR pulse to a very high degree. The delay difference of one oscillation period is just 1.3 fs at 800 nm, which means we need to control the delay with a precision measured in attoseconds. The technique relies on overlapping two light beams in time and space and delaying one to the other, essentially requiring an interferometer.

Perhaps the most famous interferometer, the *Michelson-interferometer*, which was used to disprove the notion of the *ether* [56], would not be a suitable candidate. The basic principle, where each arm of the interferometer is traversed back and forth, would make for a very complicated design when incorporating HHG. Instead, most RABITT-interferometers, including the one in Lund, relies on the principles of *Mach & Zehnder* [57, 58]. The Mach-Zehnder interferometer utilizes two beam splitters\* to divide the light beam in two and then recombine them. The Mach-Zehnder scheme for a RABITT-interferometer is seen in figure 3.9.

The design of the actual interferometer is seen in figure 3.10. The output from the laser chain in figure 2.13 is fed to the setup from the left in the figure. A beam splitter reflects 70% towards the HHG setup (1<sup>st</sup> arm) and transmits the remaining 30% to the delay stage (2<sup>nd</sup> arm). In the first arm, the beam is traversing an aperture and is then reflected, as in figure 3.11, onto a spherical focusing mirror. The incident angle onto the focusing mirror is minimized to reduce spherical aberrations. The focus of the mirror lies, after entry to a vacuum chamber, in the center of a drilled channel through a cell which fills up with a rare gas, usually argon or neon, and the resulting high-order harmonics are emerging from the output of the cell. The generating IR beam is absorbed by a metallic filter, which transmits and shapes the spectrum of the HHG. In the second arm, a small part of the beam is reflected onto a CCD detector, which detects and corrects the pointing of the beam (the actual correction is applied before the beam enters the setup, not shown in the figure). The rest of the beam is sent through a retro-reflecting stage, where rough corrections to the delay is performed, and then reflected off a piezo-controlled mirror, before it is focused into a vacuum cham-

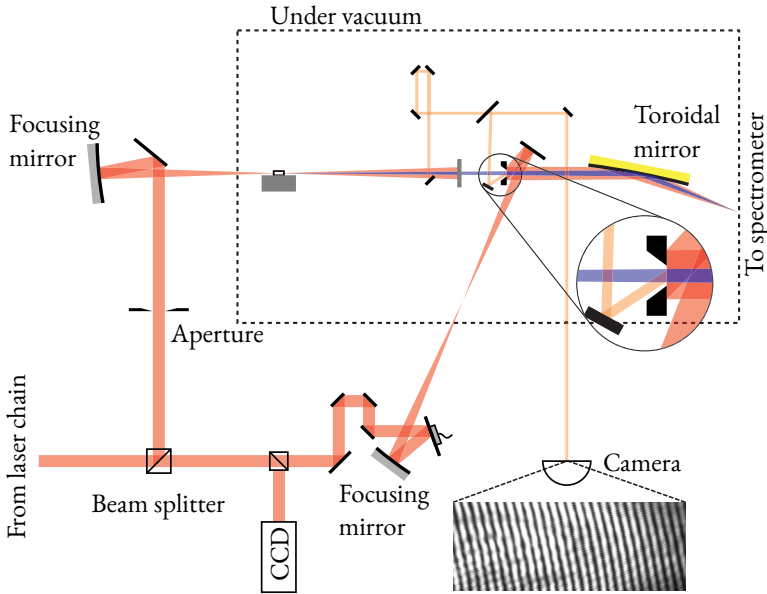


Figure 3.10. *A semi-realistic ray-trace of the interferometer. The output from a laser chain is supplied from the left. A beam splitter sends 70% of the power to an HHG setup (up). The beam (in red) is focused into a gas channel which fills with argon or neon as the pulse passes. The emanating APT (in blue) passes through a metallic filter, where the co-propagating IR is absorbed, and travels through a drilled hole from the back side of a mirror. Here, it is recombined with the other arm. The beam splitter sends the other 30% through a delay stage, and is reflected off a piezo-controlled actuator before it is focused into the vacuum chamber. This beam is reflected off the perimeter of the drilled mirror, and co-propagates with the APT after reflection. They are focused with a toroidal mirror into an electron spectrometer.*

ber. The piezo-controlled mirror adjusts the delay of the second arm in nanometer steps. The focusing mirror in the second arm is placed at exactly the same beam distance as in the first arm, to match the diverging wavefront of the generated harmonics. The second arm is then reflected onto a drilled mirror towards the toroidal mirror. The HHG passes through the drilled hole and the two beams are now recombined. The grating incidence on the toroidal mirror ensures good reflectivity for the XUV-radiation. The toroidal mirror images the point of the harmonic generation to the interaction region of the electron spectrometer of choice (either an MBES or VMIS).

Also seen in the figure is a second interferometer (orange)

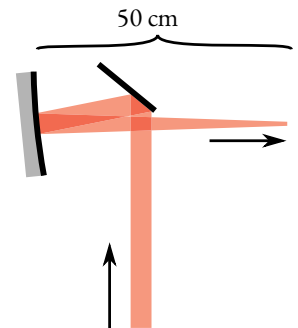


Figure 3.11. *Beam path through the focusing geometry.*

used to stabilize the delay between the two arms previously described. A small fraction of the IR beam is deflected before it is absorbed by the metallic filter. This part is sent through a small delay stage and is then recombined with the IR beam from the second arm that passes through the drilled hole from the right side. The recombined beams are sent, with a small angle between them, onto the CCD chip of a camera. The spatial angle between them creates spatial fringes, as shown in the figure. The phase,  $\nu = \omega \Delta\tau$ , of the pattern depends on the optical angular frequency,  $\omega$ , and the delay,  $\Delta\tau$ , between the two arms. With this design, the absolute overlap cannot be found without an auto-correlation measurement. However, during readout of the camera, the relative delay can be tracked. A script reading the delay from the camera controls the piezo-actuator and corrects the delay for unwanted movements.

\* confusingly abbreviated «as»

This setup allows the delay between the two arms to be controlled to a precision of less than 50 attoseconds\*, while keeping the delay stable over hours to days.

### 3.5 SUMMARY

In this chapter, we have seen how we can access the spectral phase of the attosecond electronic wave-packet, which includes one contribution from the pulse train and one from the atomic transition. This is made possible thanks to the RABITT method, involving interference of electron waves and an optical interferometer with active stabilization for control on the attosecond time scale\*.

\*In 50 as, light covers a length of  
15 nm, roughly equal to 150  
atoms in a row

In the next chapter, we will dive deeper into the details of the RABITT method and highlight a few applications.





# Time-Frequency Analysis

*The false-color two-dimensional map that is produced from a RABITT measurement is often referred to as spectrogram. A spectrogram is a visual representation of a spectrum of frequencies (or in this case kinetic energies) as they vary with time (or similarly, delay). Since the variation in time is expected to be periodic in a RABITT spectrogram, a frequency analysis of the delay axis can return the frequency and phase of the sideband oscillation. If the phase varies as a function of the sideband orders, this points to dynamics on the attosecond timescale (or dynamics of an individual pulse in the train). If the phase varies across the spectral width of a single sideband, this points to dynamics on the femtosecond timescale (or dynamics across the whole pulse train). Even though the spectral phase measurement paints the whole picture of the dynamics, it is more natural to explore the evolution of a system in time. It is therefore necessary to transform the data to the time domain. Additionally, a time-frequency representation can give a more complete picture than analyzing the two domains separately.*

- 4.1 Analysis of the spectrogram
- 4.2 Attosecond dynamics with attosecond resolution
- 4.3 Femtosecond dynamics with attosecond resolution
- 4.4 Limitations of RABITT
- 4.5 Summary

## 4.1 ANALYSIS OF THE SPECTROGRAM

**L**ET US recall the result from equation 3.5. The phase of a sideband is a contribution of three terms,  $(2\omega\tau - \Delta\phi_q - \Delta\phi_q^{at})$ , where  $\tau$  is the controlled delay between the APT and the IR. This leaves us with two unknowns. In reference [9], Paul and coworkers relied on calculations to prove that  $\phi_q^{at}$  is small for the transition involved, and could therefore be neglected. This allowed them to extract  $\Delta\phi_q$  for each sideband. By arbitrarily setting\* the phase of the first measured harmonic to 0, the rest of the harmonic phases,  $\phi_q$ , can be determined through addition of the measured phase differences  $\Delta\phi_q$ . Through a monochromatic approximation of each harmonic, the full intensity,  $I(t)$ , of the pulse train can be reconstructed [59] via:

\*Essentially removing the absolute temporal reference.

$$I(t) = \left| \sum_{q=q_i}^{q_f} \sqrt{I_q} e^{-i(q\omega t - \phi_q)} \right|^2 \quad (4.1)$$

where  $q_i$  to  $q_f$  is the range of measured harmonic orders and  $q\omega$  is the angular frequency of harmonic order  $q$ . Through this *characterization* procedure, Paul *et. al.* provided the first experimental evidence of attosecond pulses. Following this seminal work, a *single* attosecond pulse (SAP) with a duration of 650 as was generated and measured the same year [10], using a slightly different characterization scheme. The emergence of single attosecond pulses, which are generated by modifying the harmonic generation conditions [32, 33], pushed the development of new schemes. A method called *attosecond streaking* [41], often referred to as just *streaking*, uses the SAP to take snapshots of the electric field of a strong IR pulse. The SAP ionizes a target and the instantaneous IR field shifts the photoelectron energies proportionally to its field strength. Similar to RABITT, the time information is generated by relating all events to the delay between the XUV pulse(s) (often called pump) and the IR pulse (often called probe).

In the years following, experiments using an SAP measured a core-hole lifetime in krypton atoms [11] and observed electron tunneling [13] and electronic valence motion [12] in real-time. At the same time, RABITT was used to probe the phase of resonant atomic transitions [60, 61].

In 2010, Schultze and coworkers found that there appears to be a delay in photoemission [14] between two different electronic levels of neon, using the streaking method simultaneously on the two levels. The astonishing discovery of Schultze *et. al.* attracted a great deal of theoretical attention, due to the disagreement between the experimental data and theoretical calculations. In 2011 in Lund, RABITT was successfully used to measure a delay in photoionization of argon [15], spawning the term *photoionization time delay*.

Klünder and colleagues achieved this by deploying a referencing technique similar to the one shown by Schultze *et. al.*: an APT was generated in argon and further shaped using a metallic filter combination of chromium and aluminium, resulting in a spectrum of just four harmonics of orders 21 to 27. A RABITT spectrogram was then acquired by ionizing an argon target with this narrow spectrum, overlapped with the IR pulse. The harmonic spectrum was energetic enough to ionize both the  $3s^2$  and the  $3p^6$  levels of argon, resulting in a spectrogram containing photoelectrons from both levels. Since the two levels are ionized by the same XUV pulse train, the influence of the light can be subtracted. What remains is a measure of the transition phase difference between the two levels,  $\Delta\phi_q^{3s} - \Delta\phi_q^{3p}$ . Just as the relative phases of the harmonics are associated with a group delay\* the relative phase of the atomic transition results in an additional group delay of the electron wave packet:  $\tau_q^{at} = \Delta\phi_q^{at}/2\omega \approx -\delta\phi_q^{at}/\delta\omega$ . The remaining phase difference between the two levels is then a measure of their delay difference,  $\tau_{3s}^{at} - \tau_{3p}^{at}$ . RABITT has since then been used to measure the phase of a resonant electronic wave-packet using two different techniques [62, 63], and with angular resolvability to measure delays at different angles of emission [64]. It is clearly a versatile technique, used in all the papers of this thesis.

In the next sections, a typical procedure following an acquisition of a RABITT spectrogram is described in detail. The later sections provide some highlights from the papers.

#### 4.1.1 Sideband Analysis

The acquired spectra at different delays are typically presented in a spectrogram as shown in figure 3.8. A Fourier analysis across

\*Group delay:

$$\bullet \quad GD = -\frac{\partial\phi}{\partial\omega}$$

Group delay dispersion:

$$\bullet \quad GDD = \frac{\partial GD}{\partial\omega}$$



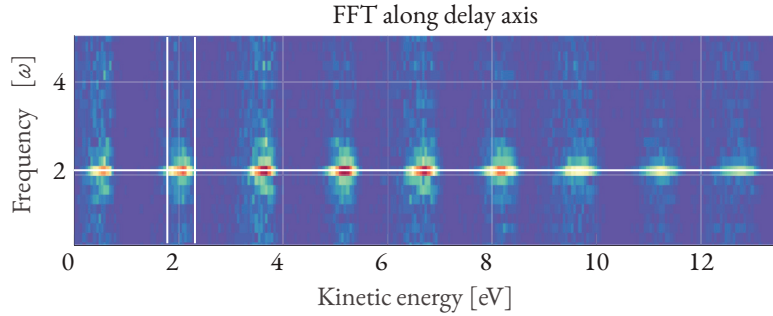


Figure 4.1. A Fast-Fourier Transform along the delay axis of the RABITT spectrogram shown in figure 3.8, revealing the  $2\omega$ -frequency of the sideband oscillations. Higher frequencies are absent, indicating promising conditions for RABITT. A peak-detection algorithm finds the width of the sideband.

the delay axis of each energy bin in the spectrogram reveals the oscillation frequency of the sidebands. In figure 4.1, a discrete Fourier transform algorithm, the *Fast Fourier-Transform* [65], has found the frequencies of the data in figure 3.8. The  $2\omega$ -frequency is marked with a white line. The Fourier analysis is a convenient way to survey the conditions of RABITT. If the probe field is too strong, not only will there appear higher frequencies in the analysis due to higher order photon absorption/emission, but odd orders might overlap with the  $2\omega$  frequency, distorting the phase [66]. The absence of a  $4\omega$  peak tells us the probe is "weak enough".

The marked sideband in figure 4.1 has been automatically selected from the  $2\omega$ -peak in frequency space using a standard peak detection algorithm. The peak is summed across its width and the signal intensity as a function of delay is seen in figure 4.2 as diamond markers. The DC component (mean of the signal) is removed and the signal is normalized. A non-linear least square algorithm, based on the *Levenberg-Marquardt method* [67, 68], is used to fit the amplitude and phase of the cosine signal with frequency  $2\omega_1$ . Here,  $2\omega_1$  is the peak frequency from the FFT analysis, which might slightly differ\* from  $2\omega$  of an 800nm fundamental due to laser and interferometer jitter. The uncertainty of the fit is also determined.

The procedure is repeated for all visible sidebands. In figure

\*A significant difference points to a drifting interferometer

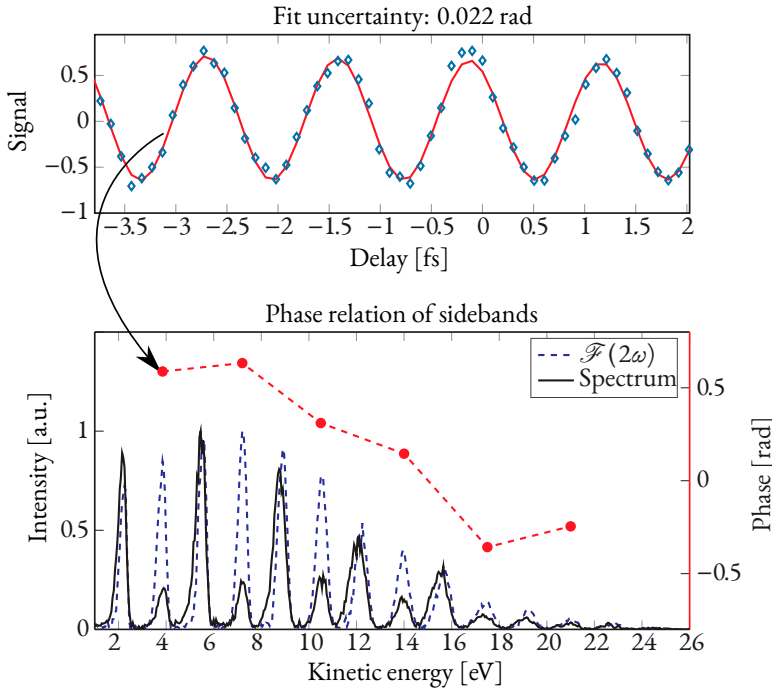


Figure 4.2. *Top:* The sideband selected in figure 4.1 is summed across its spectral width and the intensity as a function of delay is shown (diamonds). The signal is fed to a fit algorithm, which returns the best fit (red curve). *Bottom:* The phase of the fit is compared to the other sidebands. The absolute phase is arbitrary, we can only determine the relation between the sidebands. Note that the atto-chirp is inverted in this figure. Also shown is the spectrum and the amplitude of the  $2\omega$ -frequency of each energy bin. The harmonic electrons and the sidebands oscillate with the same amplitude since the total number of electrons are preserved.

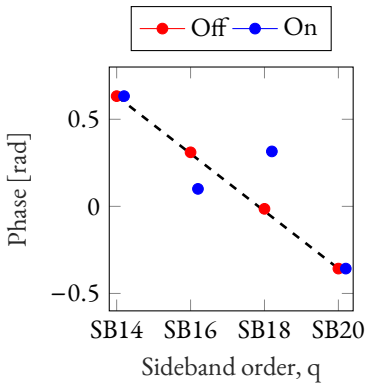
4.2 a spectrum at a certain delay is shown along with an outline of the signal at  $2\omega$  in frequency space (will be referred to as the  $2\omega$  amplitude from here on). The phase of the central bin of each sideband is shown along with a dashed line connecting them. It is important to note that the absolute phase value is arbitrary and chosen to be in a region between  $-\pi$  and  $\pi$ . It is the phase *relation* between each sideband that we have determined. This relation is commonly referred to as the atto-chirp, since it is connected to the width of the individual pulses in the APT (recall figure 2.10). A flat phase relation corresponds to Fourier limited pulses in the train. However, in reference [15], the atto-chirp is

not the main interest. By taking the difference of the measured phase relation between the two spectrograms, this phase cancels out. Any phase difference between the same sideband order, i.e. photoelectrons ionized by the same harmonic order but from two different atomic levels, is then only due to the influence of the atom.

Photoionization can also be a resonant process if the photon energy coincides with that of a *semi-bound* excited state, referred to as an *autoionizing state*. Such a state will decay to a continuum state via Coulomb interaction. This means that photoelectrons that are released through autoionization to a final energy  $E_f$  and photoelectrons that are directly ionized to the same energy will interfere. Fano derived a formulation in 1961 that describes the interactions involved [69] very well. We will return to this formulation in a later section.

\*i.e their photon energies

If one (or several) harmonic energies\* are resonant with an atomic transition to an autoionizing state, both the amplitude and the phase of the photoelectrons will be affected. If the resonant harmonic energy is scanned across the resonance, utilizing the ability to modify the fundamental frequency of the laser, the neighboring sideband will show signs of the resonance as seen in figure 4.3. This was first demonstrated by Kotur and coworkers in 2016 [62]. The same method was used in *Paper IV* to measure the angle-dependent phase (delay) of the same autoionizing state, developing the method further. A detailed description of the experiment is presented in section 4.3.



#### 4.1.2 Frequency-resolved analysis

The method of Kotur *et. al.* was improved by Gruson and coworkers [63] in 2016. They used a frequency-resolved analysis of the sidebands to recover the phase of the autoionizing state in a single RABITT scan. The almost continuous sampling of the phase allowed them to reconstruct the build-up of the electronic wave-packet during photoionization. We improved on this method in *Paper III* using a high resolution spectrometer and a time-frequency analysis to follow the dynamics more closely. In *Paper II*, we used the same frequency-resolved analysis to differentiate between different ionization processes, resulting in the resolution of a 7-year long debate on the measurement of

Figure 4.3. The atto-chirp is fitted with a straight line, and the deviation in phase of S16 and S18 is attributed to H17 lining up (labeled «On») with a Fano resonance. The points labeled «Off» shows the atto-chirp when H17 is not resonant.

photoionization time delays in neon [14]. For a more detailed description of the analysis, see section 4.2.

The generation conditions of HHG, namely the quickly varying intensity across the time span of the pulse, result in each harmonic possessing a quadratic phase across its spectral width. The phase at the harmonic peaks exhibit a quadratic relation as a function of the orders as well [70]. The sideband phases that we measure from RABITT are a difference of two quadratic phases of the neighboring harmonics, which are very similar, resulting in a flat phase as a function of energy across the sideband width, as seen in the top of figure 4.4. Therefore, in case of non-resonant ionization it is a good approximation to analyze the oscillation of either the central energy of the sideband or the integration across its spectral width. If the harmonic spacing is not conforming to twice the IR photon energy, as can easily happen if the intensity in the generation medium is too high as this will cause a non-linear shift of the fundamental frequency, the probe (which is not shifted) will interfere with different parts of two consecutive harmonics. This causes a linear tilt of the sideband phase across the energy axis, as shown in the middle of figure 4.4.

Although similar, the spectral phase of the resonant two-photon wave-packet is not an exact replica of the resonant one-photon wave-packet, due to the spectral width of the IR pulse, as shown by Jiménez-Galán and coworkers [71], and seen in the bottom of figure 4.4. To an approximation, the measured phase is equivalent to a convolution of the harmonic phase with the probe pulse. A spectrally broad probe might therefore obscure sharp phase features.

By analyzing the sideband oscillation bin by bin, the broadened phase of the electron wave-packet (created through absorption of two photons) is retrieved as a function of photon energy. Even if no harmonic is resonant, several atomic levels might be ionized if a high energy harmonic spectrum is generated. Owing to the broad spectrum, photoelectrons originating from different atomic levels might share kinetic energies. As such, it is important to perform a frequency resolved sideband oscillation analysis not only in the case of resonant photoionization (*Paper III*) but also in the case of multiple processes leading to electrons with similar kinetic energies, as shown in *Paper II*.

Following this overview, we will in the next sections have a

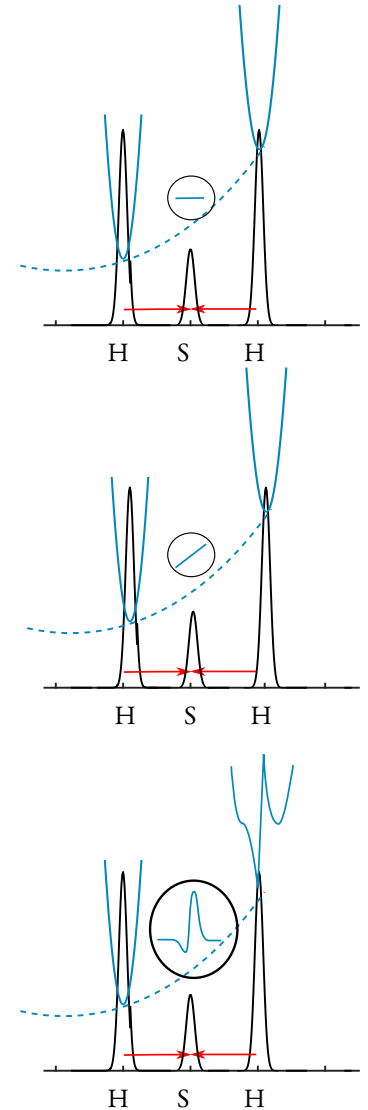


Figure 4.4. A frequency resolved analysis of the sideband (S) reveals a flat phase (top), tilted phase (middle) and a sharp phase jump (bottom), characteristic of a Fano resonance.

detailed look into some applications of the RABITT technique.

## 4.2 ATTOSECOND DYNAMICS WITH ATTOSECOND RESOLUTION

The process of photoionization was traditionally thought to be instantaneous, so the findings of Schultze *et al.* attracted a great deal of attention, not the least from theoretical efforts to successfully model the measured delay [72–74]. The measured value of  $21 \pm 5$  as could never be reproduced theoretically. Even 7 years after the breakthrough, following the birth of the term photoionization time delay, the discrepancy had still not been resolved. At the same time, RABITT had been successfully utilized to determine time delays in argon.

### 4.2.1 Time delays in neon

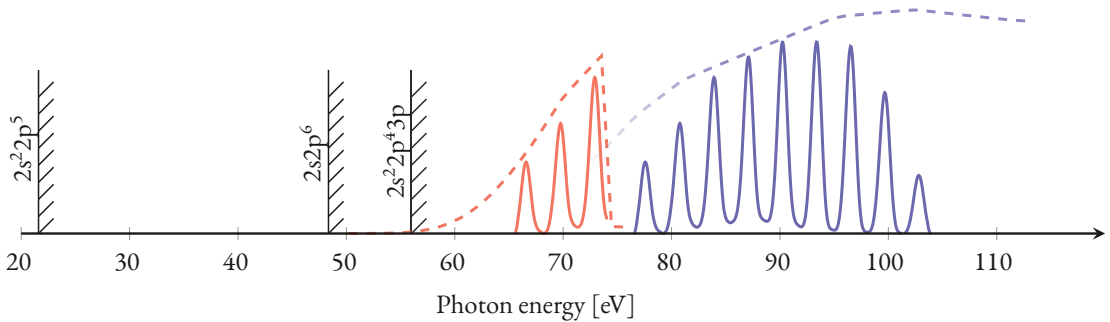


Figure 4.5. Energy diagram of neon, highlighting the three levels of interest in the study. The two different harmonic spectra are also shown, along with their filter curves. Adapted from Paper II.

In Paper II we decided to use RABITT, with the same simultaneous ionization method as in reference [15], to determine the time delays in neon. The states involved are  $2s^2 2p^5$  (also referred to as « $2p$ », with an  $I_p$  of 21.6 eV) and  $2s^1 2p^6$  (also referred to as « $2s$ », with an  $I_p$  of 48.5 eV). To reach the ionization potential of  $2s$ , we generated harmonics in neon leading to an unfiltered

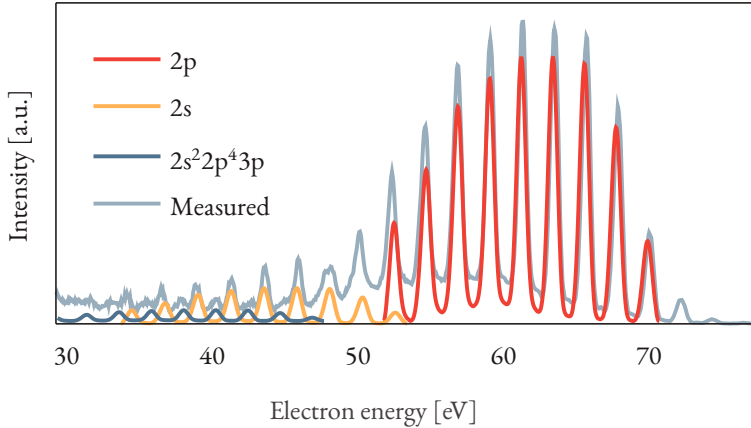


Figure 4.6. *A simulated photoelectron spectrum, simply created by shifting a harmonic spectrum by the ionization potential of the three levels in figure 4.5, and normalizing with the ionization probability of respective level. A measured photoelectron spectrum shows clear signs of electrons from the shake-up state.*

spectrum ranging up to a 100 eV. To prevent the faster photoelectrons stemming from the 2p level to overlap with the slower from the 2s level, the spectrum was filtered with a 200 nm thick foil of metallic zirconium, which acts as a high-pass filter above 60 eV, and an aluminium foil of 200 nm thickness, which acts as a band-pass filter between 10 and 72 eV. Together they form a narrow band-pass filter, letting through just three harmonics between 62 and 72 eV, as seen in figure 4.5. The phases of sideband 42 (S42), stemming from the photoelectrons of the 2s level and the 2p level, was compared as described before. A theoretical model based on a many-body perturbation theory approach, which accounts for the interaction between the escaping electron and the remaining electrons, agreed very well with the extracted delay at this photon energy [74].

To gather more data points at higher energies, the aluminium filter was replaced with yet another zirconium foil, resulting in a high-pass filter above 75 eV. As discussed in reference [72], there are a huge number of accessible states below the 100 eV region, not including the two states we are focusing on. While most of the transitions are very improbable, there is a transition to the excited state  $2s^2 2p^4 3p$  which has a probability of about a sixth of

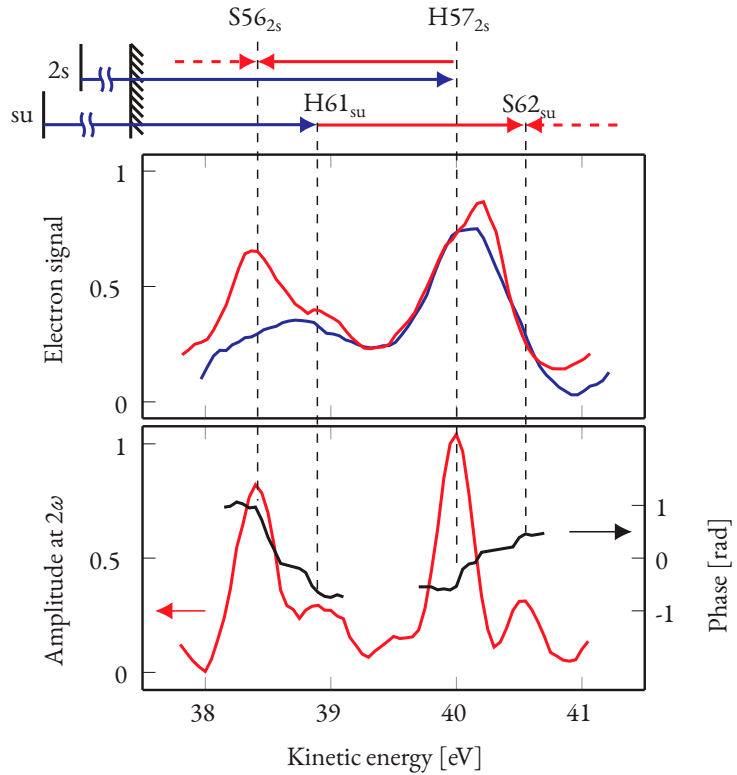


Figure 4.7. *Top: Energy diagram, explaining the different processes involved. Middle: The XUV-spectrum (blue), highlighted in figure 4.6, is compared to the XUV+IR-spectrum (red). Bottom: A Fourier analysis of the full spectrogram reveals a fast phase variation (black) of the  $2\omega$ -frequency (red) as we scan from 38 to 39 eV. Only the flat, horizontal part of the phase of S56 is considered. Reproduced from Paper II.*

the ionization from 2s, which in turn is about a sixth as strong as the ionization probability from 2p. The  $2s^2 2p^4 3p$  state is a so-called shake-up state, meaning the atom is left in an excited state after ionization which also results in a lower kinetic energy of the photoelectrons.

The spectrum containing three harmonics was narrow enough that we could neglect the photoelectrons from the shake-up state. When we now use a broader spectrum, the state cannot be ignored anymore. As shown in figure 4.6, the energy of the state is unluckily placing the photoelectrons in-between the photoelectrons stemming from 2s, with the same intensity of a

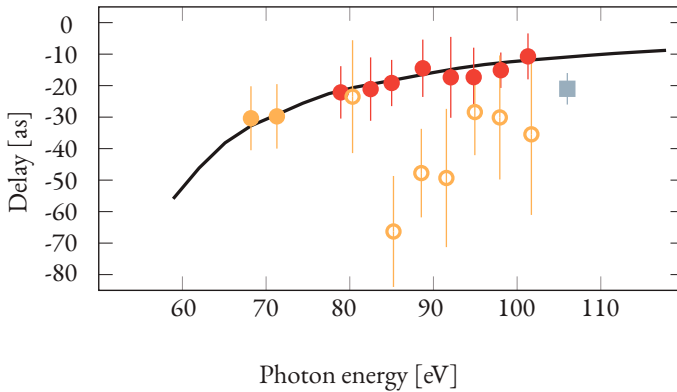


Figure 4.8. The phase difference between  $2s$ -level and the  $2p$ -level, interpreted as a delay. The yellow dots are retrieved by summing the sidebands across their spectral widths. The red dots are retrieved with a frequency (energy) resolved analysis, described in figure 4.7. The gray square is the result of reference [14]. Adapted from Paper II.

would-be sideband. This is confirmed with an experimentally measured spectrum also seen in the figure. The shake-up electrons are problematic, since the electrons at harmonic spacing oscillate out of phase with the sidebands, causing an incoherent mixing of the oscillations of the sidebands from  $2s$  and the electrons from harmonic frequencies stemming from the shake-up state. Consequently, we had to employ a frequency-resolved analysis.

The method is described in figure 4.7. There we see a zoom-in of a small section of the spectrum in figure 4.6, now with the added sidebands as well. The intensity spectrum is quite congested, but by displaying the oscillation amplitude at  $2\omega$ , the different contributions are clearly separated. The phase analysis shows a sharp jump when we move from 38 to 39 eV, where the harmonic is overlapping with the sideband. Only the flat phase\* of the sideband was considered. Repeating the analysis for all  $2s$  sidebands, we extracted a time delay across a 30 eV photon energy range with excellent agreement with theory, as seen in figure 4.8. In the same figure, we also see the result of not employing an energy resolved analysis (in hollow circles).

\*The phase marked by the dashed line from the label «S56<sub>2s</sub>»



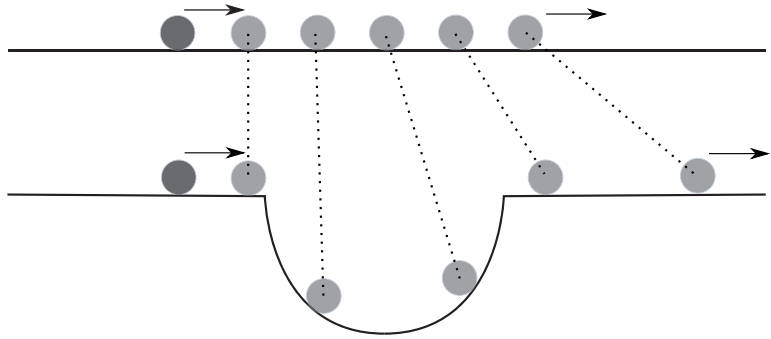


Figure 4.9. *A classical analogy of the origin of a time delay in photoemission. Two beads are released simultaneously and travel with the same velocity. The bead meeting the "potential" is accelerated in the well, exiting the potential ahead of the undisturbed bead.*

#### 4.2.2 Interpretation of time delays

As seen in figure 4.8, the delay in emission between the two levels vary quite a lot as a function of energy. The measured atomic delay (or delay difference in this case) can be approximated as a contribution of two terms:  $\tau_A \approx \tau_1 + \tau_{cc}$ . The delay term  $\tau_{cc}$  is a measurement induced delay, stemming from the second photon absorption/emission in the vicinity of the atomic potential. This *continuum-continuum* transition adds a universal delay [75, 76] which increases quickly as we approach the ionization threshold. Indeed, if an analytical calculation of this delay is removed from the measured delay difference, the energy dependence is much weaker in the case of neon. The delay difference that is left arises due to the different atomic potentials seen by the 2s and 2p photoelectrons. In *Paper II* we relied on calculations to prove that we could subtract the delay of the 2p electron and therefore extract the delay of the 2s electron, which proved to be identical to the so-called *Wigner-delay*. Since this delay arises due to the atomic potential, our timing reference is essentially a freely moving electron. It is perhaps more intuitive to think of it in terms of a scattering process, as Wigner [77] formalized in 1955. An electron wave-packet moving under the influence of the atomic potential will be delayed (or advanced) compared to a free electron wave-packet.

In figure 4.9 we see a classical analogy. Two beads are traveling

with a velocity  $v$  on a straight line. One bead approaches a well, symbolizing the atomic potential, while the other is undisturbed. The gray beads are snapshots taken at a constant intervals as time progresses. As seen, the bottom bead is accelerated by the well, and while it will exit the well with the exact same velocity as it entered, it will have covered a greater horizontal distance than the bead at the top, causing a delay between the two.

### 4.3 FEMTOSECOND DYNAMICS WITH ATTOSECOND RESOLUTION

Not all electronic processes occur on an attosecond time scale. Processes following photoionization, such as interactions between the remaining electrons and the outgoing electron, often occur on a longer time scale. Auto-ionization, which is induced by electron-electron interaction, is one such process. The interference between the electron wave-packets being released through direct photoionization and auto-ionization gives rise to a characteristic line shape in the photoelectron spectrum, named after Ugo Fano who developed an extensive theoretical framework in 1961 [69]. Probing the ionization dynamics with RABITT gives us the most complete picture to date of the process.

#### 4.3.1 Fano resonance

A Fano resonance is not only an atomic concept, it is a universal phenomenon related to oscillators. A harmonic oscillator, such as a pendulum, has a resonance frequency,  $\omega_R$ , which depends only on the length of the pendulum in this case. If we force the pendulum to oscillate with this frequency, the amplitude will grow rapidly. All other frequencies will result in much lower amplitudes. In figure 4.10, we see two different pendulums coupled with a spring and an external force applied to one of them. There will now also exist a frequency of the driving force where the amplitude of the forced pendulum vanishes completely, as seen in figure 4.11.

In the lower half of figure 4.10, we see the atomic equivalent of the classical Fano resonance. The two harmonic oscillators are now replaced by a dipole transition to an autoionizing state

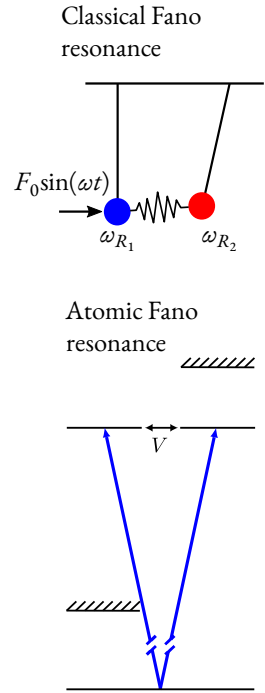


Figure 4.10. *Top: A classical Fano resonance. Two harmonic oscillators are coupled with a spring, while one (blue) is driven with an oscillating force. Bottom: An atomic Fano resonance. A dipole transition to a final, unbound state (left) and a transition to a bound state (right). The bound state is coupled to the unbound state via electron-electron interaction.*

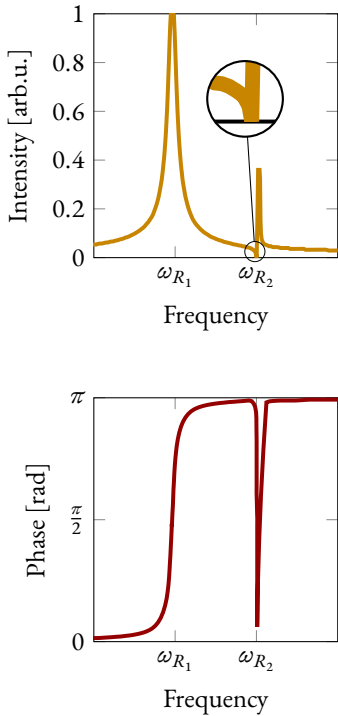


Figure 4.11. *Top: The amplitude of the pendulum subjected to the driving force (the blue pendulum), as a function of driving frequency. The resonance frequencies of the blue and red oscillators,  $\omega_{R_1}$  and  $\omega_{R_2}$  respectively, are marked. The resonance frequency of the red oscillator is seen in the response curve of the blue oscillator. As we approach  $\omega_{R_2}$ , the amplitude vanishes completely. Bottom: At the same time, the phase of the oscillation makes a jump of  $\pi$  radians.*

and one to the continuum. The electron-electron interaction which induces the decay into the continuum corresponds to the coupling spring. Since the transition to the continuum is flat, i.e. no frequency is preferred over any other, a detection of the released photoelectrons will only show the asymmetric line shape.

In addition to the amplitude, the phase of the oscillation will also vary as we change the driving frequency. When we approach and cross  $\omega_{R_1}$ , the phase of the oscillation compared to the driving force changes quickly, and frequencies above  $\omega_{R_1}$  are out of phase with the oscillation. We can see this for ourselves by holding the top of a single pendulum in our hand (i.e. not a coupled pendulum). Slowly rocking the string back and forth will force the pendulum to oscillate and the movement of the ball will follow our hand. If we slowly increase the speed with which we rock, the amplitude will grow. If we increase it too much however, the bottom weight will move in the opposite direction of our hand: the motion is  $\pi$  out of phase. The phase of a Fano resonance typically increases by  $\pi$  as we pass  $\omega_{R_2}$ , only to decrease by  $\pi$  again, as seen in the bottom of figure 4.11.

### 4.3.2 Build-up of a wave-packet

As mentioned, in *Paper III* we used the same technique showed in reference [63] to access the phase and amplitude of a resonant wave-packet. The system investigated was helium, where the two electrons in the ground state,  $1s^2$ , are excited to the state  $2s2p$  when the impinging light has an energy of 60.15 eV. This state reconfigures to the ground state of a helium ion,  $1s^1$ , by releasing one of the electrons, leading to the interference which creates the characteristic line shape. In fact, this line shape in helium was the motivation for Fano's formulation. According to his formulation, the transition probability amplitude,  $R$ , depends on an asymmetry parameter,  $q$ , and the reduced energy,  $\varepsilon$ :

$$R(\varepsilon, q) = \frac{q + \varepsilon}{\varepsilon + i} \quad (4.2)$$

Both the asymmetry parameter and the reduced energy is a property of the autoionizing state in question, and the definition of them can be found in reference [69]. In the experiment in *Paper III*, the 39<sup>th</sup> harmonic (H39) of the laser pulse centered at 800

nm was tuned to the energy of 60.15 eV, by careful shaping of the fundamental spectrum. A certain de-tuning was added, i.e. the central energy of H39 did not overlap perfectly with the state, to ensure equal amplitudes from the direct and autoionizing paths. Since we use non-monochromatic radiation, H39 will create a resonant electron wave-packet. If we know the phase and amplitude of the wave-packet, we can re-trace its creation in "real-time".

An energy-resolved analysis of the phases of sideband 38 or 40 shows a fast phase variation across its spectral width. As discussed in figure 4.4, the energy-resolved phase of a non-resonant sideband should be flat if no blue-shift is introduced. As such, any additional phase variation in one harmonic lies on top of this background, allowing for a direct correspondence of the measured phase variation to the phase of the wave-packet. Note that this is a two-photon wave-packet\*, due to the additional transition in the continuum. The measured intensity of a sideband is related to the amplitude,  $A_{39-1}$ , of this two-photon wave-packet by [63]:

$$|A_{39-1}| \propto \frac{I_{38}}{\sqrt{I_{44}}} \quad (4.3)$$

where  $I_{38}$  is the measured intensity of sideband 38 and  $I_{44}$  the intensity of a non-resonant sideband. As we now have extracted the *spectral* phase and amplitude, we can access the *temporal* amplitude via the Fourier transform.

To get an even more complete picture of the process, we can apply a short-time Fourier transform (STFT) with a moving window across the temporal amplitude, to generate a spectrogram of the process. The spectrogram shows how the frequencies, i.e. the spectral width of the wave-packet, evolve over time. The result of the STFT depends on the features of the window we chose for the Fourier transform and it can therefore be difficult to attribute features of the spectrogram to actual dynamics or artifacts of the transformation. Consequently, we adopted a time-frequency representation which does not depend on the window: the *Wigner representation*\* [78, 79]. It can be seen as the Fourier transform of the auto-correlation function of the wave-packet. A projection across the respective axes also returns the spectral/temporal intensity of the wave-packet.

\*Although it closely resembles the one-photon wave-packet.

\*It is often used in ultrafast optics to represent the characteristics of a light pulse.

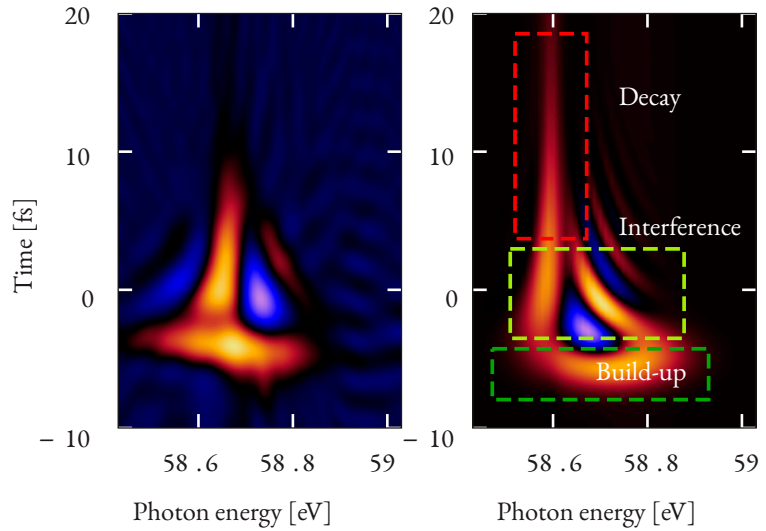


Figure 4.12. *The Wigner-representation is a simultaneous view of the energy- and time-components of a signal, in this case a two-photon electron wave-packet emanating from a Fano resonance. Left: Representation of the measured amplitude and phase of the Fano resonance at 60.15 eV in helium ( $60.15 - 1.55 = 58.8$ ). Right: Representation of a simulated amplitude and phase. Three different regimes are identified.*

In figure 4.12 we see a false-color Wigner representation of the resonant two-photon wave-packet. The left image represents the measured phase and amplitude while the right is a calculated phase using the method described in reference [71] with parameters mimicking the experiment. The spectrogram has three distinct areas: the build-up of the wave-packet which resembles the spectral width of the resonant harmonic; the interference between the direct and the resonant path; and the exponential decay of the resonance. As we showed in *Paper III*, the features of the spectrogram are dependent on the parameters of our pulse that we use to probe the dynamics. As such, we advocated for the use of a spectrally narrow (temporally broad) probe pulse. Indeed, the left part of figure 4.12 shows experimental data recently acquired using a 10 nm bandwidth probe, compared to the 70 nm bandwidth in *Paper III*. The resemblance to the simulation is striking.

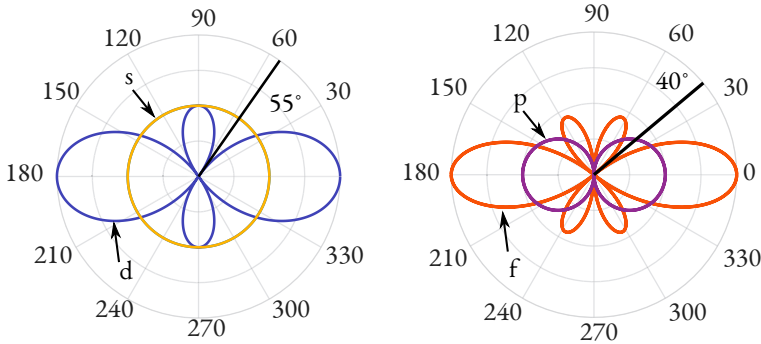


Figure 4.14. *Left: The rotational distributions of the s- and d-levels, reachable by a one-photon transition from p (see figure 4.13). At 55°, the d-level probability vanishes. Right: As in the left figure, but for the f- and p-level, reachable by a two-photon transition. At 40°, the f-level probability vanishes.*

#### 4.3.3 Towards a "complete" measurement

A "complete" measurement, in the quantum mechanical sense, measures every observable of a system. In the previous system, helium, two electrons are involved in the autoionization-process but the continuum wave-packet can only take an angular momentum of  $\epsilon p$ . In *Papers IV*, we revisited the resonant state of argon of reference [62]. Here, an electron is excited from the ground state  $3s^2 3p^6$  to the excited state  $3s^1 3p^6 4p^1$ . The continuum state can now take on either an angular momentum of  $\epsilon s$  or  $\epsilon d$ , owing to the direct ionization channel originating from a p-level. The direct ionization with H17 is illustrated in figure 4.13, where the continuum-continuum transitions of RABITT are also drawn.

A measurement of solely the kinetic energies of the created photoelectrons following ionization would not be able to distinguish between these transitions, resulting in a loss of information about the dynamics. A more sophisticated approach needs to be able to measure the angle of emission of the electrons as well, since the final continuum states have different angular distributions. In *Papers IV* and *VI*, we used a VMIS to detect the angle of emissions during acquisition of the RABITT spectrogram.

In figure 4.14 we can see the projected photoelectron angular distributions\* of the different levels involved. In the left plot, the

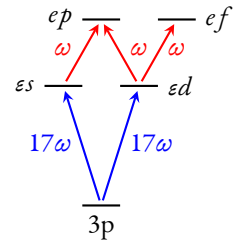


Figure 4.13. *A sketch of the possible one- and two-photon transitions from the ground state of argon,  $3p$ , to the continuum,  $\epsilon$ , with angular momenta  $s$  or  $d$ , and the additional transition in the continuum to the final state,  $e$ , with angular momenta  $p$  or  $f$ .*

\*It is strictly the normalized spherical harmonics that are plotted

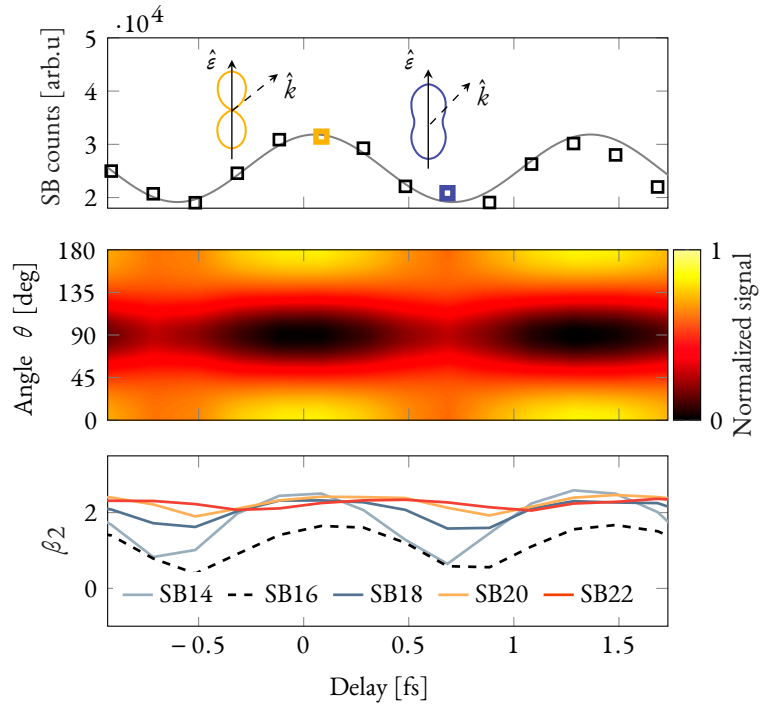


Figure 4.15. *Top: Outline of the oscillation of SB14 as a function of the delay. Two instances of the PAD are shown and the laser polarization is marked in dashed lines. Middle: The normalized PAD of SB14 for the same delay steps. A bright region corresponds to a high probability of finding electrons at this angle. Bottom: Sidebands 14 to 22. SB16 shows sign of the resonant state we studied in Paper IV and is therefore not included in the analysis. Reproduced from Paper VI*

distributions of the one-photon transition are shown individually. The VMIS will collect photoelectrons from both channels which means the measured distribution is an incoherent\* sum of the two. However, we can identify an angle, often referred to as the *magic angle*, where the cross-section of the d-level vanishes. Photoelectrons collected at an angle of  $55^\circ$  are therefore purely from the transition to  $\epsilon s$ . Now, to access the phase we need to induce a transition in the continuum, which complicates the matter. As seen in figure 4.13, there are three continuum transitions possible which ends up in two different final states. To the right in figure 4.14, the projected angular distributions of these final states are shown. Again, there is an angle,  $40^\circ$ , where one of the cross-sections vanishes (the f-level), while the other

\*Since the final states are different

(p-level) does not. However, the p-level is reachable from both  $\epsilon s$  and  $\epsilon d$ , meaning we have still not entirely decoupled the transitions. Simulations showed that the energy dependent phase at this angle is deviating from the phase at other angles.

In *Paper IV*, we were able to measure the energy and angle-dependent phase of a resonant two-photon electronic wavepacket, by tuning the central wavelength of the laser and performing several RABITT measurements. In *Paper VI*, we instead studied the *non-resonant* emission of photoelectrons stemming from the 3p-level, using the same experimental setup and measurement technique. In figure 4.15 we see the photoelectron angular distribution (PAD) of sideband 14 (SB14) along with the  $\beta$ -parameters of sidebands 14 to 22, at different delays between the APT and the IR. The PAD, reconstructed from the measured  $\beta$ -parameter, oscillates between the two distributions shown in the inset at the top of the figure. The distribution at a trough of the sideband oscillation has a non-zero amplitude perpendicular to the polarization direction of the laser light. In other words, we find a periodic emission of photoelectrons perpendicular to the laser polarization at specific delays between the fields. This emission decreases\* with the sideband order, as seen in the bottom of the figure. This behavior can be explained by applying Fano's propensity rule\* [80] to the continuum-continuum transition. In figure 4.16, we see an illustration of the principle. The bold arrows indicate an enhanced transition amplitude, compared to the dashed arrows, indicating a reduced transition. This asymmetry leads to a delay-dependent modification of the PAD.

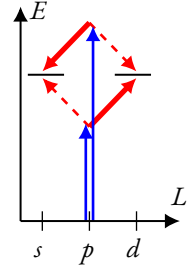


Figure 4.16. Schematic representation of Fano's propensity rule for the case of sideband formation from two intermediate continuum states. Adapted from *Paper VI*.

\*  $\beta = 2$  corresponds to emission along the polarization.

\* Stating that a transition that increases the electron angular momentum is favored, due to increase of the centrifugal potential with angular momentum

#### 4.4 LIMITATIONS OF RABITT

While RABITT is a versatile and robust technique for probing the dynamics of photoionization, there will be physical limitations determining how small time scales\* we can resolve. Still, the plausibility of the extraordinary resolution has not yet been discussed in detail. In *Paper V* we investigated possible sources of error for a RABITT measurement, ranging from uncertainties stemming from the light properties to errors generated by instabilities in the interferometer. We also discussed how to choose the parameters for the sampling of the sideband oscillation.

\*i.e. fast dynamics



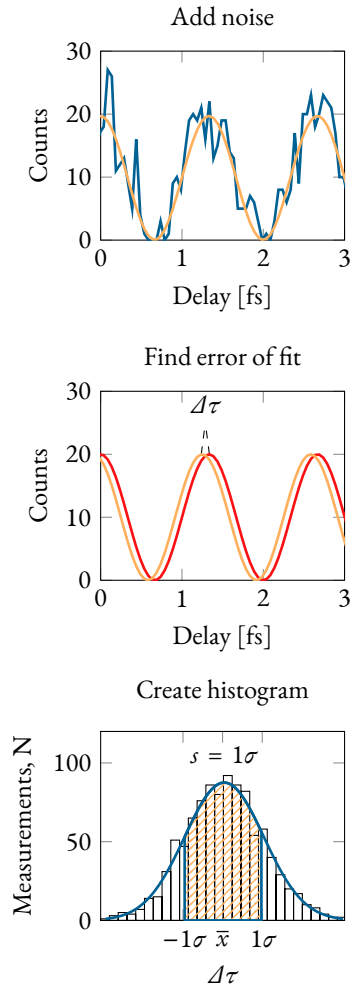


Figure 4.17. The procedure of the Monte Carlo-simulations. A cosine is injected with random noise and a fit of the noisy curve is compared to the original, unperturbed cosine. A histogram of a thousand errors is shown on the bottom, where  $1\sigma$  is marked. Adapted from Paper V.

#### 4.4.1 Monte-Carlo simulations

In a RABITT measurement, we need to sample equation 3.5 for a finite period of delay time (which we refer to as the number of *oscillation periods*) in non-zero delay steps (which we refer to as *step size*). At the same time, the stabilized delay between the pulse train and the IR will jitter around its mean value. Furthermore, at each delay step, a photoelectron spectrum is acquired during a duration which is often determined by the count rate. The count rate, i.e. the number of electrons produced (or detected) each second, depends on the amount of XUV photons, the laser repetition rate, the amount of gas supplied in the interaction region and the target atom.

As is apparent, there are many parameters that might ultimately affect the accuracy of the phase determination. We decoupled these sources of uncertainty and devised a set of Monte-Carlo simulations (a Monte-Carlo method relies on repeated random sampling) to examine their effects. The simulations were set up as shown in figure 4.17:

- 1 Equation 3.5, now with the simpler form  $I(\tau) = \cos(2\omega\tau - \Phi)$  where  $\Phi$  is chosen randomly, is sampled with a chosen step size and for a certain number of periods (see figure 4.18 for an illustration of these definitions.).
- 2 For each sample point, a random variable drawn from a normal distribution and with a set variance of  $\sigma_t^2$  is added in the horizontal direction to emulate interferometer instability. Another random variable, now drawn from a Poisson distribution with a variance of  $\sigma_s^2$ , is added in the vertical direction to emulate the noisy process of counting electrons.
- 3 The noisy cosine is fed to the non-linear least square fitting algorithm mentioned in Chapter 3. The phase of the best fit is compared to  $\Phi$  and the discrepancy is referred to as the «error» of the phase retrieval.
- 4 The above routine is repeated a thousand times and the errors are collected in a histogram. The resolution of the phase retrieval is defined to be equal to the standard deviation,  $\sigma$ , of the histogram.

The procedure is initially run with a jitter of 50 as RMS (the stability of the interferometer) to keep the delay at the desired delay value. A set of simulations were conducted for a constant number of sample points:  $\text{sampler periods} = \text{nr of points} \times \text{step size}$ . The resolution, as defined above, was determined for 101, 51 and 26 sample points. The result is shown in figure 4.19. As seen, the resolution is not dependent on how we distribute the points between the  $\text{step size}$  and  $\text{sampler periods}$ , as long as we can resolve the oscillation frequency (we cannot sample at a rate of  $1\omega$  or lower). The resolution doubles as the amount of points increases fourfold.

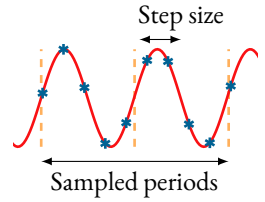


Figure 4.18. The definition of «step size» and «sampled periods».

The resolution we have determined is the estimated error of a single phase retrieval. A sample size of a thousand tries is large enough to closely estimate the normal distribution of errors. A larger sample size will not decrease the standard deviation of the distribution, we will only come closer to the true distribution. A collection of  $N$  real measurements allows us to estimate the true mean,  $\bar{x}$ , of some quantity  $x$ . The standard deviation of a single measurement is denoted  $\sigma$ . The standard deviation of the mean, or simply standard error, is then given by:  $\sigma_{\bar{x}} = \frac{\sigma}{\sqrt{N}}$ .

The resolution is then found to increase (i.e. the error decreases) linearly as the jitter of the interferometer decreases. Interestingly, the absolute value of the jitter is not a limiting factor, as long as the sideband can be sampled with a finer step or during more periods. Even an oversampling, where we sample with a step size smaller than the RMS of the jitter, results in an increase of the resolution. For a typical delay jitter of 50 as and a step size of 100 as, we can reach a resolution of 10 as in our phase retrieval if we sample 10 periods (13 fs total delay difference) of the sideband oscillation.

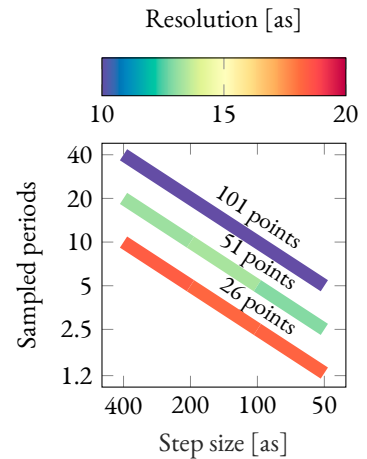


Figure 4.19. Results from the Monte Carlo-simulations. Each line represents a constant number of sample points. If the step size is decreased from 400 as to 200 as, we can only sample half the number of periods. As shown, the resolution is independent of the step size and sampled periods for a certain number of sample points (indicated by the labels). If the number of points increases by  $4x$ , the resolution increases by  $2x$ . Adapted from Paper V.

#### 4.4.2 The recipe for RABITT

A real acquisition of a RABITT spectrogram requires many considerations to be weighted against each other. A common limiting factor is the total time spent on a measurement, which is given by  $\text{spectrum acquisition time} \times \text{nr of points}$ .

In figure 4.20 we see a false color map of a matrix of simulation parameters. Each point  $(x,y)$  in the map corresponds to a simulated measurement, with a certain number of sample points,

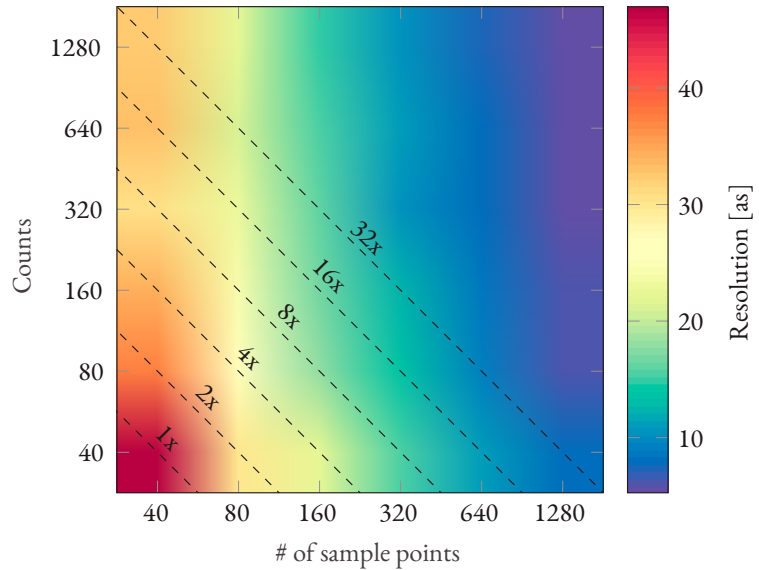


Figure 4.20. *A false-color image of the RABITT resolution, as a function of number of points and acquired counts in the sideband. Since the scales are logarithmic, the diagonal lines corresponds to a constants acquisition time, as indicated by the labels. For a certain acquisition time, the resolution can vary up to 3x, depending on the number of sample points chosen and the counts acquired. Reproduced from Paper V.*

$x$ , and a certain number of acquired counts,  $y$ . The number of acquired counts is defined as that corresponding to the maximum sideband oscillation:  $y = 100$  means the sideband oscillates in integer numbers between 0 and 100. The resolution can be read on the colorbar to the right of the image. The axis scales are logarithmic, which means that any point along a diagonal line corresponds to the same acquisition time of a spectrogram.

The false-color image shows that the number of sample points should clearly be prioritized over acquiring more counts in the sideband. For the line labeled "32x", which has an acquisition time of 32 times that of the line labeled "1x", the resolution varies from 30 as (if counts are prioritized) to 10 as (if points are prioritized). At 1280 points, little is gained by acquiring more counts.

## 4.5 SUMMARY

In this chapter we have seen how, by accessing the spectral phase of the attosecond electronic wave-packet, we can follow processes initiated by photoionization in real time. This includes timing the delay of escaping electrons released from the atom and following the creation and destruction of a resonant electron wave-packet. Extending the technique, we discussed a proof-of-principle technique which measured the phase for all angles of emission, providing a complete set of information about the process. Lastly, we examined the interferometric technique itself, known as RABITT, to detail its current possibilities and limitations in terms of time resolution.

The next chapter will summarize this thesis work and provide a peak into the near future of attosecond interferometry.







# Outlook

*In this thesis, we have introduced the realm of ultrafast science, showed how attosecond light bursts are generated from an intense laser pulse and discussed why interferometry is such a powerful tool, helping us access the spectral phase of electron wave-packets. A few examples from the papers were then highlighted, showing how the spectral phase allows us to time the process of electrons escaping an ionized atom and reconstruct the creation and decay of a resonant wave-packet. These are all important steps towards the realization of real-time observation and control of microscopic electron motion in atoms or more complex systems.*

- 5.1 Experimental improvements
- 5.2 Coincident detection
- 5.3 Technological improvements

---

## 5.1 EXPERIMENTAL IMPROVEMENTS

**F**ULL INSIGHT and control of charge movements in atoms and molecules is still a long time away. The road is full of challenges and it is outside the scope of this section to name and address them all. For an extensive review, see references [81–83]. Here, I will address some improvements to the techniques discussed in the thesis and provide insight into the current challenges and ongoing projects of the attosecond group in Lund.

The experimental and analytical techniques that are shown in this thesis would benefit from a couple of technical improvements. The frequency resolved analysis, commonly referred to as *Rainbow RABITT*, is limited by the complex process of frequency mixing due to the finite bandwidth of the probe, which is not easily compensated for in the post-analysis. A narrow bandwidth (long pulse) probe greatly improves the resolved dynamics in for example the *Wigner representation*, as discussed in *Paper III* and shown in *Chapter 4*, figure 4.12. The analysis in *Paper II*, which discerns photoelectrons from different states, would not only benefit from a narrow probe, but also from narrower harmonics (achieved through generating a longer pulse train). A bit paradoxically, these methods would benefit from longer IR pulses, not shorter. Our temporal resolution is not directly affected by the pulse lengths, as discussed in *Paper V*, although the short pulses allow us to generate the harmonic spectrum. A spectrum reaching higher energies would open the door for new dynamics to be probed, such as core shell dynamics, accessed by photon energies ranging from 100 eV to 1000 eV and beyond. The cut-off energy is most "easily" increased by adopting longer wavelength, since  $U_p \propto \lambda^2 I$ , although this requires a complete rebuild of the laser system.

## 5.2 COINCIDENT DETECTION

A technique not discussed in this thesis is an electron detection technique often referred to as *coincident detection* [84]. If the target gas density or laser intensity is reduced such that a laser shot, on average, produces a detectable electron 10 % of the times, we can assume that only a single ionization event took place per shot. If we detect several electrons from a single laser shot, there is a very high probability that they originated from the same atom. This is a very useful tool to disentangle different ionization processes. A common way of doing so is to collect the electron kinetic energies in a two-dimensional map, where one axis spans the energy of the first electron to reach the MCP (the most energetic one) and the other axis spans the energy of the second electron. A process where the two electrons share energy would then show up as diagonal lines. The *Auger process*, discovered by Auger in

1925 [85], is also easily identified since the kinetic energy of the *Auger electron* is independent of photon energy. A coincident technique is, however, also very time consuming at relatively low laser repetition rates. At 1 kHz, we only collect an average of 100 electrons per second. A two-dimensional map of 100 by 100 energy bins will, in 100 seconds, fill each bin with just a single count. Collecting enough counts to be statistically relevant may take hours to days.

### 5.2.1 Xenon 4d

A system which has been under investigation for many years in Lund is the 4d electronic state of xenon, with an ionization energy of just below 70 eV. Ionization from the 4d level of the ground state of xenon ( $4d^{10}5s^25p^6$ ) results in a secondary electron being released through an Auger process, as shown in figure 5.1. The 4d level consists of two closely lying levels, split by 2 eV, depending on the spin direction of the electron. We studied ionization of the 4d shell through coincident detection, since a normal spectrum acquisition collects all electrons released in the process, such as electrons emanating from the 5s and 5p shells as well. The broad light spectrum of harmonic orders renders the photoelectron spectrum very congested. Specifically, the 2 eV split of the 4d level creates very challenging conditions for RABITT. A coincident detection on the other hand can limit the focus to electrons only released from the 4d shell, since the ionization process results in secondary electrons. The constant energy of the *Auger* electrons, 8.29 and 10.29 eV, makes identification of the two spin levels very simple.

For a long time, the lacking stability of the laser and the interferometer hindered any definite conclusion of the 4d ionization process. Recently, promising results have been obtained in Lund where we have been able to acquire the sideband phases of both 4d levels. In figure 5.2, we see recently acquired coincident data. Half of the figure shows data acquired with just the xuv light, the other half is acquired when the IR beam was overlapped with the xuv in the interaction region. To read the figure, recall that a single point in the figure corresponds to *two* electrons. Since the Auger electrons (for example the ones released with 8.29 and 10.29 eV) are almost always slower, we can usually assign the *slow*

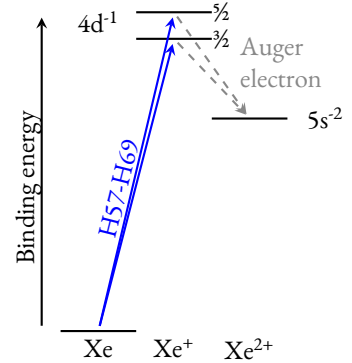


Figure 5.1. Energy diagram of the Auger process from the 4d shell. The harmonic comb ionizes the 4d shell ( $I_p$  of 67.5 and 69.5 eV). An electron from the 5s-shell fills the hole in the 4d-shell, and another electron from 5s is released in the process, leaving the xenon ion doubly ionized.



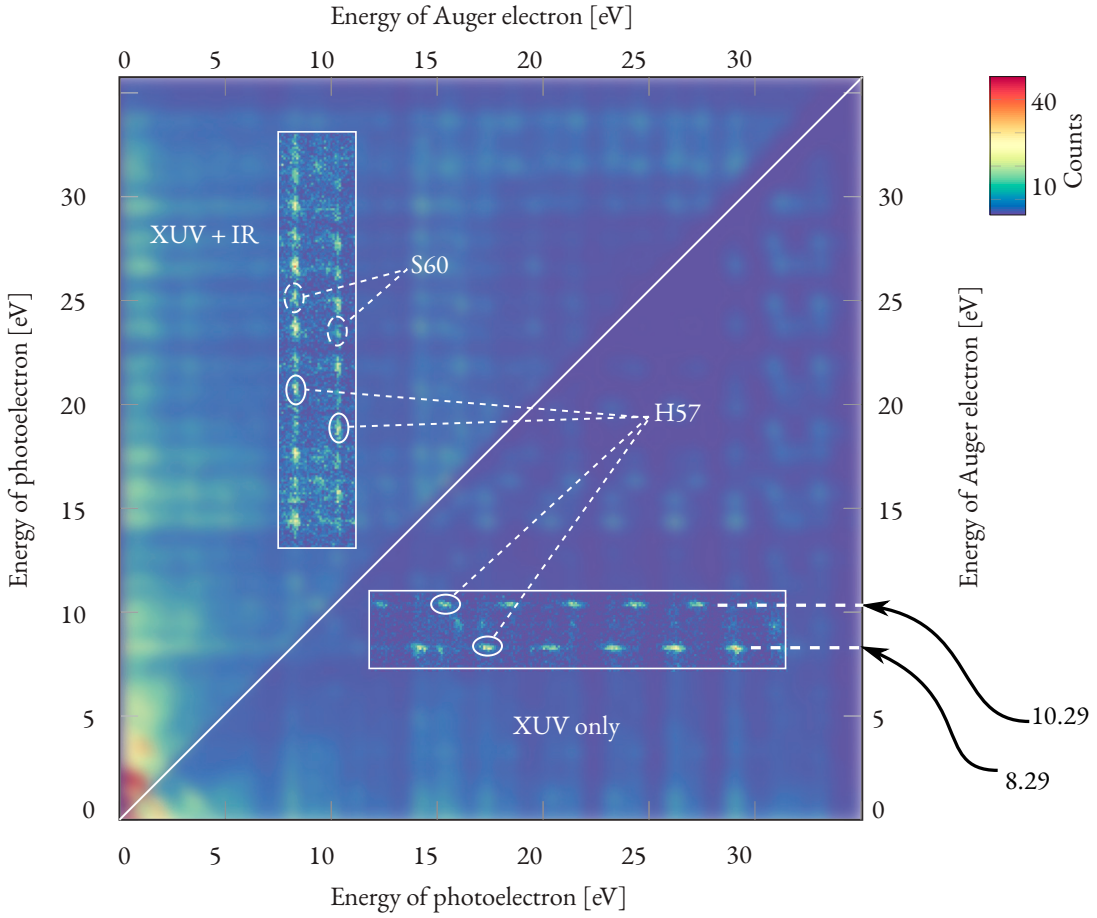


Figure 5.2. False-color energy map of a coincident detection of electron from the 4d shell of xenon. Electrons not in coincidence with the Auger electrons of figure 5.1 have been blurred for clarity.

electron to the Auger electron. The *fast electron* is then the photoelectron. On the horizontal axis (for the XUV only diagram) and respectively the vertical axis for the XUV + IR diagram, we then have our normal XUV spectrum. The respective Auger electron that was released as a result of the ionization allows for the two spin-levels to be separated energetically. We can then analyze the two spin levels individually, and compare their RABITT phases.

### 5.3 TECHNOLOGICAL IMPROVEMENTS

Even though the data is very promising, a single spectrogram acquisition takes a full day. Acquisition of less than ideal data, a discovery which can often only be made after the fact, is then a day gone to waste. Consequently, even a modest increase of the repetition rate of the laser would vastly facilitate the coincident detection. In light of this, an upgrade of the Lund kHz laser is in preparation, to reach 3 kHz repetition rate with the same pulse parameters as the current one.

In this thesis work, we have advocated for a high energy/frequency resolution alongside the extreme temporal resolution. As we have shown, there are times when high energy resolution is required, while other times yet another measurement parameter (i.e. angular information) is more valuable. Truth be told, the measurement in *Paper IV* might have been even more successful had it not lacked in energy resolution. A concoction of a VMIS and an MBES might then seem like the perfect spectrometer for attosecond experiments. Conceptually, this is what an ARTOF (*Angular Resolved Time-of-Flight*) spectrometer provides. It combines a flight tube with a position sensitive detector. There are early plans to install such a device in the attosecond beam line. These upgrades, along with a refinement of the interferometer to increase the stability further, will take the attosecond laboratory to the next stage.





# The Author's Contribution to the Papers

## Paper I **Roadmap of ultrafast x-ray atomic and molecular physics**

During my first two years, we struggled to generate any results due to technical issues and challenging experiments. In this paper, we discuss these challenges and the current status of experiments on photoionization dynamics in atoms, in a road-map on ultrafast atomic and molecular physics. I wrote parts of the manuscript.

## Paper II **Photoionization in the time and frequency domain**

In this paper, we determine photoionization time delays in neon atoms over a 40 eV energy range with an interferometric technique combining high temporal and spectral resolution, solving a puzzle raised by 7-year-old measurements. I had a leading role in conducting the experiments, I analyzed all the data and developed new ideas for the analysis. I wrote a major part of the manuscript.

Paper III **Time-frequency representation of autoionization dynamics in helium**

In this paper, we used an energy-resolved interferometric technique to measure the spectral amplitude and phase of autoionized wave packets emitted via the  $sp2^+$  (referred to as  $2s2p$  in this thesis) and  $sp3^+$  resonances in helium. Applying various time–frequency representations, we observe the build-up of the wave packets in the continuum and disentangle the dynamics of the direct and resonant ionization channels. I had a leading role in conducting the experiments, prepared methods for the analysis of the data and wrote parts of the manuscript.

Paper IV **Anisotropic photoemission time delays close to a Fano resonance**

Here, we investigated the attosecond photoemission dynamics in argon in the 20–40 eV spectral range, in the vicinity of the  $3s^1np$  autoionizing resonances. We present measurements of the differential photoionization cross section and extract energy and angle-dependent atomic time delays with an attosecond interferometric method. I had a leading role in acquiring the Lund experimental data. I developed methods of treating and analyzing the data. I contributed to the manuscript by discussions and feedback.

Paper V **Temporal resolution of the *RABBIT* technique**

In this paper, we thoroughly examine the *RABBIT* method using numerical simulations. We analyze the effects of the spatial and temporal properties of the light fields and of the experimental procedure on the accuracy of the method. I prepared and conducted the simulations of the experimental procedure, produced most of the figures and wrote a substantial part of the manuscript.

Paper VI **Fano's propensity rule in angle-resolved attosecond pump-probe photoionization**

In this paper we study *non-resonant* photoionization of argon  $3p^{-1}$ , using an attosecond interferometric technique and a VMIS. The spectrometer allows us to follow the angle-of-emission of the photoelectrons as a function of the delay between the attosecond pulse train and the laser field. We detect a periodic emission of photoelectrons perpendicular to the laser polarization at specific delays. We can explain the phenomenon with Fano's propensity rules. I took part in the experiment and contributed to the manuscript via feedback and discussions.



# Acknowledgments

**T**HE WORK throughout this thesis could not have been accomplished were it not for the joint collaborations of many, many people. I am very thankful for the welcoming and helpful atmosphere upheld by the past and present people of the Division of Atomic Physics. Special thanks go to those I have been closely working with in the *attogroup*: Cord Arnold, Johan Mauritsson, Chen Guo, Anne Harth, Marija Kotur, Shiyang Zhong, Emma Simpson, David Busto, Saikat Nandi, Piotr Rudawski, Samuel Bengtsson, Yu-Chen Cheng, Neven Ibrakovic, Jan Lahl, Hugo Laurell, Sara Mikaelsson, Lana Neoricic, David Kroon, Linnea Rading, Jasper Peschel, Hampus Wikmark, Sylvain Maclot and Stefanos Carlström. It has been a pleasure working with all of you and I thank you all! I would also like to extend my deepest thanks and appreciation to Claes-Göran Wahlström, Åke Johansson, Anne Petersson Jungbeck and Jakob Testad.

To my supervisor Anne: You are a true inspiration, both professionally and personally. It has been an honor working in your team. I am amazed by your passion, your knowledge and your ability to stay humble and down-to-earth. Thank you for being so understanding in times when I was stressed and thank you for pushing me when I needed it! I could not have wished for a better supervisor! I would also like to thank my co-supervisors: Mathieu Gisselbrecht and Per Johnsson. You are both extremely knowledgeable and I thank you for your guidance.

To my family and friends:

*Ni som känner mig tvekade säkert inte på att det här skulle gå vägen. Det gjorde nog aldrig jag heller, men trots det har*



---

*jag i stunder känt mig väldigt stressad på grund av den position man befinner sig i. Det är i sådana stunder, när stressen känns överväldigande, som man är extra tacksam för ens nära och kära. Jag har lärt mig minst lika mycket om mig själv som jag lärt mig om fysik under denna spännande resa, och jag har insett att lärdomen om sig själv är den viktigaste av alla.*

*Ett år in på resans gång träffade jag min själsfrände, Eléni. Det är mycket tack vare dig som jag står här, så lugn inför allt som väntar! Vi brukar säga att det enda som spelar roll är att vi har varandra, allt annat är en bonus. Jag älskar dig! Jag ser så mycket fram emot vår framtid tillsammans.*

*Jag hade inte heller varit där jag är idag om det inte vore för mina fina föräldrar: Paula & Per. Ni har alltid uppmuntrat min nyfikenhet för hur saker fungerar och mitt intresse för naturvetenskap. Tack för alla läxförhör genom åren i skolan! David & Rebecka, vi hade en väldigt rolig barndom tillsammans med mycket lek. Man växer upp för fort egentligen. Vad ni än väljer att göra i livet måste ni lova att vi alltid håller kontakten. Några som också varit som syskon för mig är mina kusiner: Samuel & Jonatan. Det bästa vi visste var att bygga med Lego. Stort tack också till Rita & Christian, för ert stöd och för att ni inte tröttnade på allt Lego som verkade hamna lite överallt.*

*Jag vill också tacka min mormor, Sylvia, som nyligen gick bort. Vi syskon hade så kul med dig, både som stora och små, och du kommer alltid finnas i mina tankar. En piggare 89-åring, som dessutom kallbadade året runt, har nog inte funnits. Vila i frid.*

*Jag vill också passa på att tacka Anki & Giannis Zambas för att ni är sådana fantastiska människor. Jag hoppas jag kan återgälda allt som ni gjort för mig! Jag vill även tacka Kerstin & Nisse Andersson för att ni alltid ställer upp och för er glada inställning. Jag ser upp till er båda väldigt mycket! I ett annat liv är jag nog bonde.*

*Slutligen så vill jag tacka alla mina vänner. Familj och vänner är som sagt det viktigaste vi har. Jag vet att ni alltid finns för mig och jag finns alltid för er!*

*Narcos*



## Documentation for an ADC

**A**S PART of my doctoral education, I programmed and tested a data acquisition card of the type Analog-to-Digital-Converter (ADC) of model «U1084A» from *Acquiris*. The card samples the raw signal from the MCP (after amplification) at a rate of  $4 \cdot 10^9$  samples per second. The samples are stored as 8 bit signed integers (i.e. they range from  $-128$  to  $127$ ). Due to the high amount of data, the card included a mode to only buffer data above a defined threshold, a very suitable mode for peak detection from an electron spectrometer. The LabVIEW library supplied with the card was not functioning correctly out of the box, so what follows is a documentation to modify some files in the library to successfully implement the so-called zero-suppression mode.





---

**DOCUMENTATION TO  
INTERFACE WITH U1084A  
USING LabVIEW**

**for**

**Zero-suppression acquisition**

**Version 1.0 approved**

**Prepared by Marcus Isinger**

**Lund University**

**November 8, 2018**

---

# Contents

|          |   |           |
|----------|---|-----------|
| <b>1</b> | <b>Introduction</b>                       | <b>4</b>  |
| 1.1      | Purpose                                   | 4         |
| 1.2      | Document Conventions                      | 4         |
| 1.3      | Intended Audience and Reading Suggestions | 4         |
| 1.4      | Required drivers                          | 4         |
| <b>2</b> | <b>Configuration in LabVIEW</b>           | <b>5</b>  |
| 2.1      | Initialize                                | 5         |
| 2.2      | Configure memory                          | 5         |
| 2.3      | Configure horizontal settings             | 6         |
| 2.4      | Configure vertical settings               | 6         |
| 2.5      | Configure extended trigger source         | 7         |
| 2.6      | Configure trigger class                   | 7         |
| 2.7      | Configure operation mode                  | 8         |
| 2.8      | Configure extended averager settings      | 8         |
| 2.9      | Configure setup array                     | 8         |
| 2.10     | Configure extended memory settings        | 10        |
| <b>3</b> | <b>Acquisition in LabVIEW</b>             | <b>11</b> |
| 3.1      | Acquire signal                            | 11        |
| 3.2      | Read buffered signal                      | 11        |
| 3.2.1    | Read SSR Data                             | 11        |
| 3.2.2    | Free bank                                 | 13        |
| 3.3      | Parse raw SSR data                        | 13        |
| <b>4</b> | <b>Acquisition Program Features</b>       | <b>16</b> |
| 4.1      | General Structure                         | 16        |
| 4.2      | Peak Detection                            | 17        |
| 4.3      | Data Structure and Storage                | 17        |

# 1 Introduction

## 1.1 Purpose

This document aims to fully describe the configuration and usage of the zero-suppression mode on an acquisition card of model *Acqiris U1084A* or equivalent in a LabVIEW programming environment. The zero-suppression mode can dramatically reduce the load on both the data transfer from the card to LabVIEW and the data analysis in LabVIEW, allowing for a higher trigger and signal rate.

## 1.2 Document Conventions

The LabVIEW VIs by Agilent which are required for zero-suppression to work as intended are described in this document by listing the needed inputs and outputs of respective VI under an image of the VI-icon. Note that there might be more inputs/outputs that are not needed here and are therefore not shown.

## 1.3 Intended Audience and Reading Suggestions

This document is intended to work as a supplement to the "Programmer's Guide Agilent Acqiris Instruments" manual, which is supplied with the U1084A card, and will cover usage of the card within the LabVIEW environment. The document will focus on a correct setup of the zero-suppression (mode 7), which was missing from the supplied manual. The reader of this document is assumed to have a copy of the aforementioned manual. The reader is also assumed to be proficient in LabVIEW.

## 1.4 Required drivers

Agilent Acqiris Software CD V4.2.c - 15/02/2011

---

## 2 Configuration in LabVIEW

This chapter will introduce the some of VIs included in the Agilent driver which are needed to interface with the acquisition card. The U1084A works much like an oscilloscope, and therefore needs to be setup in a similar manner. The VIs are introduced in the order they should be used. A short description of the input and output parameters are given, but for a full description of the possible values, see the "context help" of the VI in question. For an obvious sequential execution of your program, use the error cluster wiring. The error cluster input/output are not described below, but are assumed to be used. There can be more inputs/outputs to a VI than are described here, in which case they are optional.

### 2.1 Initialize



**Input:** *Resource name*

**Output:** *Instrument ID*

This VI initializes the device with a given *Resource name* (usually PCI::INSTR0 if only one Acqiris card is connected) and returns the *Instrument ID* which is a required input for all following VIs that communicate with the card. This is the first VI you should call to start interfacing with the card.

### 2.2 Configure memory



**Input:** *Instrument ID, Number of Segments, Number of Samples*

**Output:** *dup Instrument ID*

This VI configures the memory of the Acqiris card with *Instrument ID*, i.e. the number of samples and the number of segments (can be thought of as number of triggered events) that should be stored. Wire the output *dup Instrument ID* to the input of the next VI. This output will not be discussed in the following sections.

## 2.3 Configure horizontal settings



**Input:** *Instrument ID*, *Sampling interval (s)*

**Output:** *dup Instrument ID*

This VI configures the horizontal control parameters of the Acqiris card with *Instrument ID*, i.e. the sampling interval given in seconds. There is also an optional input delay time, which is ignored when the card is operating in zero-suppression mode and therefore not used here.

## 2.4 Configure vertical settings



**Input:** *Instrument ID*, *Channel*, *Coupling*, *Full scale (V)*, *Offset (V)*

**Output:** *dup Instrument ID*

This VI configures the vertical control parameters of the Acqiris card with *Instrument ID* and *Channel* (either 1 or 2). The *Full scale (V)* configures the resolution of the sampled signal. Since in zero-suppression mode the card saves the input signal as an 8bit signed integer (-128..127) the *Full scale (V)* parameter decides which real voltage (5,2,1 or 0.5 V) should correspond to the maximum integer (127). Set as close to the peak of the sampled signal as possible for maximum resolution. The *Offset (V)* parameter offsets the real voltage before it is converted to an 8bit signed integer (-128..127).



## 2.5 Configure extended trigger source



**Input:** *Instrument ID, Channel, Trigger coupling, Trigger slope, Trigger Level 1*

**Output:** *dup Instrument ID*

This VI configures the trigger source control parameters of the Acqiris card with *Instrument ID* for a specified trigger source *Channel* (either 1 for internal trigger or -1 for external trigger source). The *Trigger coupling* sets the coupling to AC or DC with an input impedance of  $1\text{ M}\Omega$  or  $50\ \Omega$ . The *Trigger slope* decides whether the card should trigger on the rising/leading edge (positive) or falling/trailing edge (negative) part of the trigger signal. For a window trigger there is a second trigger level which is not used here. *Trigger Level 1* sets the trigger level in millivolts.

## 2.6 Configure trigger class



**Input:** *Instrument ID, Source Pattern*

**Output:** *dup Instrument ID*

This VI configures the trigger class parameters of the Acqiris card with *Instrument ID*. Some instruments support a complex feature set of triggers. For this use case, supply the string "0x80000000" to the *Source Pattern* input, which enables the External Trigger 1. For other use cases, consult the manual or the "context help" of this VI.

Now the Acqiris card is initialized for normal usage, and could be used to acquire a signal on channel 1. For readability, create a subVI with the VIs above. We now need to change the operational mode of the acquisition card from normal (mode 0) to Sustained Sequential Recording or SSR (mode 7). In this mode, we can enable zero-suppression of the input data.

## 2.7 Configure operation mode



**Input:** *Instrument ID, Mode, Flags*

**Output:** *dup Instrument ID*

This VI configures the operational mode of the Acqiris card with *Instrument ID*. To enable the "ReadModeSSRW", supply a value of 7 to the input *Mode*, along with a value 10 to input *Flags*. The flag modifier enables a second memory buffer which is needed for simultaneous data acquisition and readout.

## 2.8 Configure extended averager settings



**Input:** *Instrument ID, Channel, Parameter Key, Parameter Value*

**Output:** *dup Instrument ID*

This VI allows to configure additional parameters of the Acqiris card with *Instrument ID*, which are needed for the zero-suppression to work. The VI works with a single Key-Value pair at a time, so in order to set multiple values use this VI in a loop with two arrays that hold the keys and values. The parameters we want to set are *NbrSamples*, *NbrSegments*, *PreSamples*, *PostSamples* and *InvertData*, exactly as they are written here. The first two will overwrite the number of samples and number of segments configured in the memory settings. *PreSamples* and *PostSamples* sets the number of samples to collect before and after the signal threshold is reached. *InvertData* (default is 0, no inversion applied) sets the card to cut all data above the threshold instead of below if set to 1.

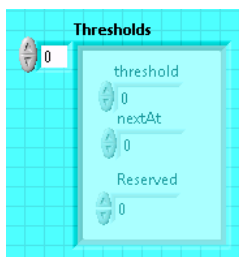
## 2.9 Configure setup array



**Input:** *Instrument ID, Channel, setupType, nbrSetupObj, thresholds*

**Output:** *dup Instrument ID*

This VI allows to configure the threshold parameters of the Acqiris card with *Instrument ID* below which it should apply zero-suppression. Here, a small modification to the VI is needed to make it work as the programmer's manual intends. Find the array called *setupData* pictured below in the VIs block diagram. It will not look like this, instead it will only have a cluster of two elements.



Modify the cluster to look like above with the number representations as shown below.

**setupData Cluster**

Array containing the setup objects.

**setupData Cluster** (cluster of 3 elements)

**threshold** (double [64-bit real (~15 digit precision)])

**nextAt** (unsigned long [32-bit integer (0 to 4,294,967,295)])

**Reserved** (long [32-bit integer (-2147483648 to 2147483647)])

Create an array of thresholds clusters as input. The threshold is set in Volts, and the nextSample tells the controller when to apply the next threshold in the threshold array. Set this input to NbrSamples if you only intend to use a single threshold. The Reserved

element can be left as 0 and should not be used. The *setupType* needs to be set to 2 as well as the *nbrSetupObj* input.

## 2.10 Configure extended memory settings



**Input:** *Instrument ID, Number of Segments, Number of Samples, Number of Banks*

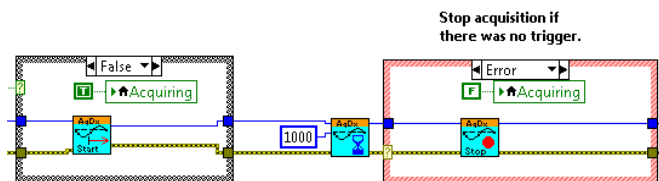
**Output:** *dup Instrument ID*

This VI allows to configure the extended memory control parameters of the Acqiris card with *Instrument ID*, which is required for the SSR mode to work. The *Number of Segments* and *Number of Samples* are the same before, rather the *Number of Banks* is the important value here, which can be set to 2 or 3.

Now the card is configured to work in the SSR mode with 2 or 3 memory banks. You should use the different "Query" VIs to make sure that the value actually has been set as you intended.

## 3 Acquisition in LabVIEW

### 3.1 Acquire signal



A simple block diagram of the acquisition call is shown above, and can be placed inside a while-loop. It looks identical to an acquisition call of the card running in normal operation. It starts an acquisition, waits for a trigger and stops acquiring either if no trigger was detected or after acquiring the selected number of samples and segments.

### 3.2 Read buffered signal

The reading of the acquired signal from the buffer is quite straightforward, requiring the VIs "Read SSR Data" to read the data and "Free Bank" to free the current memory bank making it available for another acquisition.

#### 3.2.1 Read SSR Data

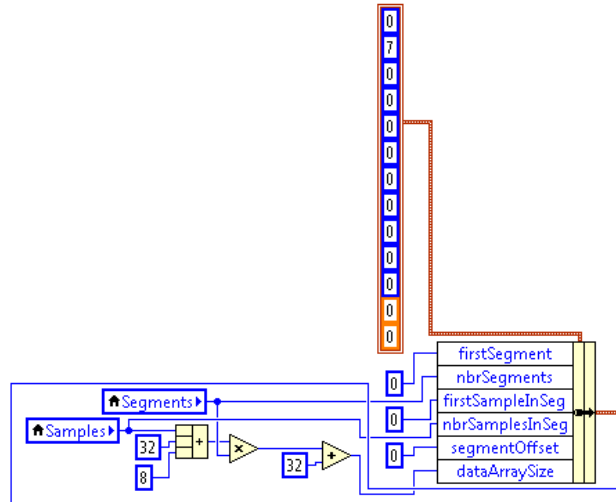


**Input:** *Instrument ID, readPar, dataArray in, Channel*

**Output:** *dup Instrument ID, dataDesc, dataArray out*

This VI reads the raw thresholded data from the Acqiris card with *Instrument ID* and *Channel*. The input *dataArray in* is a user-allocated data array of 8bit signed integers,

and can be either zeros or acquired values, they will be overwritten anyhow. The *readPar* input needs careful configuration for the readout to work. An example how to configure this parameter is shown below.



By creating a constant of the input terminal of *readPar* we get a cluster of initialized values. On page 25 of the programmer's manual there is a description of the parameters. The first zero is missing however. This zero tells the Acqiris card that the data should be sampled in 8bit, the only valid data type for the SSR configuration. This brings us to the next value, 7, which tells the card to interpret the data as zero-suppressed data. The parameters we need to manually set are the six parameters shown, which are accessed by the "Unbundle by name" function. Three of them are left as zero, *nbrSegments* and *NbrSamples* should be the same as configured before, and *dataArraySize* is the size in bytes of the user-allocated buffer that the data is transferred to. For simplicity, this buffer can be set to the worst case scenario, i.e. all of the signal is above the threshold and therefore transferred to the buffer:  $\text{maxDataSize (in bytes)} = \text{nbrSegments} * (\text{nbrSamples} + 32 + 8) + 32$ . The numbers correspond to an overhead which is always transferred, containing meta-data which we will interpret later on.

The output *dataDesc* contains information about the zero-suppressed data, such as the actual size of the data transferred, the sampling time and so on, but nothing of high importance. The *dataArray out* contains the digitized thresholded data as 8bit signed

integers together with the meta-data in a single data stream. Since this meta-data is not actually formatted as 8bit, but has been interpreted as such by the *Read SSR Data* VI, it takes a bit of trickery to retrieve the correct meta-data. More on this in section 3.3.

### 3.2.2 Free bank



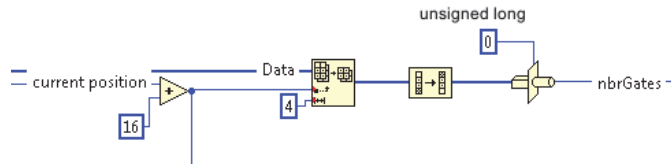
**Input:** *Instrument ID*

**Output:** *dup Instrument ID*

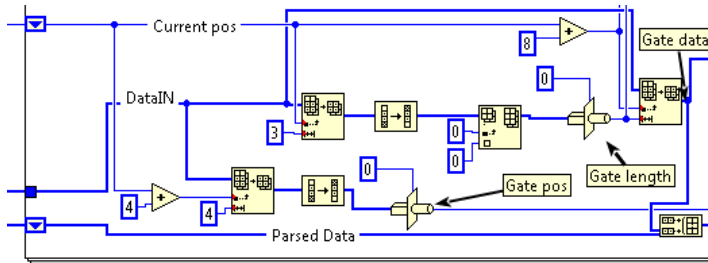
This VI frees the current memory bank, making it available to buffer a new acquisition.

## 3.3 Parse raw SSR data

On page 25 and onward in section 3.6.4 of the programmers guide, there is an explanation how the meta-data is tucked in together with the digitized data. If the data we received from the *Read SSR Data* VI was in binary format, it would be quite a straightforward process to disentangle the data from the meta-data. Now, however, the raw data is already formatted as 8bit, which means we need to re-format the meta-data to its actual data type. In the very beginning of the data stream, we have a segment descriptor, with a length of 8 words. A "word" corresponds to a data type of 32 bit length. So, the first 256 bits of a data segment are not actual digitized data from one of the channels, but a description of the data. Since these bits have been read as 8 bit data by the *Read SSR Data* VI, the first 32 (256/8) values in the data stream need to be re-cast to a new data type according to the table in section 3.6.3.1. The only data of interest in this case is the number of gates, *nbrGates*, as this describes how many gates are contained in a single segment. A gate is a sequential data stream above threshold. Below is an example of how to extract this data.



Since this segment descriptor will precede the digitized data for every saved segment, we need to keep track of our current reading position in the data stream. The current position starts at 0, the beginning of the data stream. We move it by 16 "steps" (128 bits in 8 bit data type, or 4 "words"), which is where the data for *nbrGates* starts. *nbrGates* is a 32 bit data type, so we extract the next 4 elements (32/8) in the data array and reverse the order, then re-cast them to a single 32 bit unsigned integer. This number tells us how many gates will succeed the segment descriptor. For each gate, there is a gate descriptor, 2 words (64 bits) long, which contains the length, *gateLength*, of the digitized data (of 24 bit length) which follows the gate descriptor and then absolute position in samples, *gatePos*, of the start of the data (of 32 bit length) in relation to the trigger. Both of these are necessary to extract the data correctly. We move the current position to the beginning of the gate descriptor (32 steps after the beginning of the segment which is at 0), and extract 3 and 4 elements respectively. Since LabVIEW doesn't have a 24 bit native data type, we insert an 8bit data type with a value of 0 before the 3 other 8bit data values, and re-cast it as 32bit unsigned integer. This procedure is shown below.



The actual digitized data starts 40 steps into the 8bit array, or 8 steps after the beginning of the gate descriptor. Since we don't know the end of the array before we have read the gate descriptor, we need to parse the data sequentially. We extract an array with a length of *gateLength* and move the current position by as many steps as well. The *gatePos* is used to determine the peak position of the data in relation to the trigger. If there are more gates we loop through all of them, otherwise we move to the next segment descriptor and do it all again.

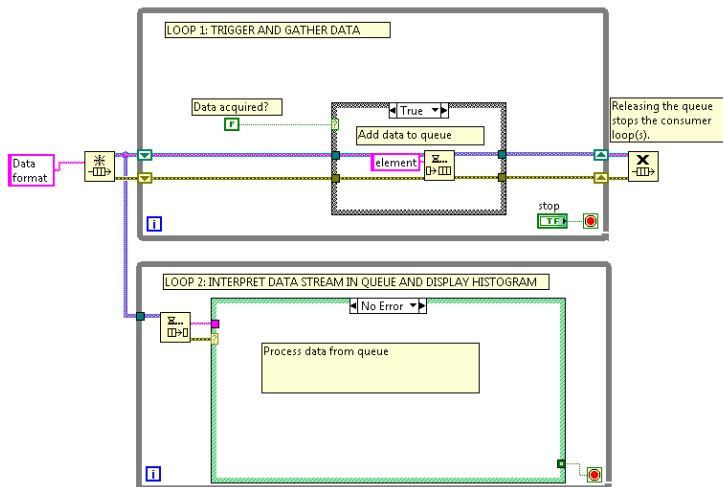


## 4 Acquisition Program Features

This chapter is dedicated to explain some of the features of the acquisition program written specifically for this type of acquisition card, with a purpose to take advantage of the features implemented in the earlier chapter.

### 4.1 General Structure

The program is structured as two parallel processes (loops), as shown below. In one loop, the card is triggered and the raw data (and meta data) acquired is added to a queue object. In the other loop, data is continuously withdrawn from the front of the queue and processed for interpretation.



With this structure, we are making sure no triggers are missed. For a trigger rate of 1 kHz, the top loop is fast enough to arm the trigger of the card each iteration, but for much faster trigger rates you might want to do a buffered acquisition instead. The bottom loop is waiting for data as long as the queue is empty, and then withdraws data as fast as it executes. In this so called "consumer" loop, the raw data is interpreted and the meta data is separated from the signal data.

## 4.2 Peak Detection

Since the acquisition card is meant to count electron, we need to convert the signal from a single electronic pulse into a number, the flight-time. The method chosen is a fast peak detection method called wavelet-based peak detection using multi-resolution analysis.

## 4.3 Data Structure and Storage

The raw, unmanipulated data we acquire from the card, after peak detection, consists of the time-of-flight (a digit of double precision) for each electron hit. This data is stored in an array during runtime, and is sequentially interpreted and presented in a histogram to the user. The data is also saved to a temporary directory using the HDF5 file format in an event based data structure, to prevent accidental data loss and increase flexibility. The event based structure is detailed in table 4.1. For each event, we store the number of hits and the time-of-flight of each hit. The data is saved sequentially in equally sized "chunks" to optimize the write-to-disk time. If there is insufficient data to fill a chunk, the unfilled space is overwritten with "-1", to clearly indicate that this is not real data. After an acquisition has finished, the temporary file is closed, and it might be copied to a directory of the users choice. This event based data needs to be read sequentially as well, starting from the very beginning, to ensure that each hit corresponds to the correct event. For a large data set, this can be quite time consuming, but the advantage is the user can interpret and present the data in a huge number of different ways.

Table 4.1: Structure of stored data.

| Hits nr | ToF [ns] |
|---------|----------|
| 2       | 100      |
| 1       | 200      |
| -1      | 50       |
| -1      | -1       |





## Photoniques Special Issue

**F**OR A special issue of *Photoniques*, we were asked to write a popular science article summarizing recent results from Lund obtained with the RABITT technique. We focused on photoionization time delays and provided an outlook on the field of attosecond science. The advertisements in the article have been removed, thereby the peculiar white-spaces and a missing page.





## HOW CAN ATTOSECOND PULSE TRAIN INTERFEROMETRY

# interrogate electron dynamics?

C.L. ARNOLD, M. ISINGER,  
D. BUSTO, D. GUÉNOT,  
S. NANDI, S. ZHONG,  
J.M. DAHLSTRÖM,  
M. GISSELBRECHT,  
A. L'HUILLIER  
Department of Physics,  
Lund University, Lund, Sweden  
[cord.arnold@fysik.lth.se](mailto:cord.arnold@fysik.lth.se)

Light pulses of sub-100 as ( $1 \text{ as} = 10^{-18} \text{ s}$ ) duration, with photon energies in the extreme-ultraviolet (XUV) spectral domain, represent the shortest event in time ever made and controlled by human beings. Their first experimental observation in 2001 has opened the door to investigating the fundamental dynamics of the quantum world on the natural time scale for electrons in atoms, molecules and solids and marks the beginning of the scientific field now called attosecond science.

Attosecond light pulses cannot be obtained from a conventional laser, but result from a nonlinear interaction, when intense femtosecond laser pulses are focused into a dilute gas. It was observed in the late eighties that this interaction leads to the emission of a comb of odd-order harmonics of the driving laser [1,2]. Unexpected from the concepts of perturbative nonlinear optics, only the first few orders decrease exponentially in power, while higher orders form a plateau of almost equal power, until a sharp drop, called the cut-off,

is reached. Depending on the generation conditions, the cut-off can exceed 100 eV of photon energy, covering several tens of harmonics, and the effect was thus named high-order harmonic generation (HHG). It was soon realized that the comb of harmonics could correspond to a train of very short pulses, *i.e.* attosecond pulses, if the harmonics were phase-locked [3]. This view was inspired by a semi-classical model of the single-atom response in a strong driving laser field [4], which was shortly after also supported by a fully quantum mechanical treatment [5,6].

The semi-classical understanding of HHG, generally referred to as the three-step model, is illustrated in *Figure 1*. First, the atomic binding potential is so strongly distorted near the crests of the driving laser field that the least bound electron may tunnel-ionize to the continuum. Second, driven by the strong laser field, the electron is taken away from the parent-ion, picking up kinetic energy. Finally, when the driving field changes sign, the electron may return to its parent-ion and recombine, whereas its excess energy is emitted as an XUV photon. The kinetic energy of the returning electron depends on its trajectory, *i.e.* the path it takes from the time it was born in the continuum to its return to the parent-ion. Not all possible trajectories return to the parent-ion and contribute to HHG. The three-step process repeats itself for every half cycle of the driving field, resulting in an attosecond pulse train (APT). While the spectrum of each individual attosecond pulse in the train is continuous, the corresponding spectrum of the train results from the spectral interference of all pulses in the train and is composed of odd-order harmonics. This can be understood in analogy to the frequency comb structure

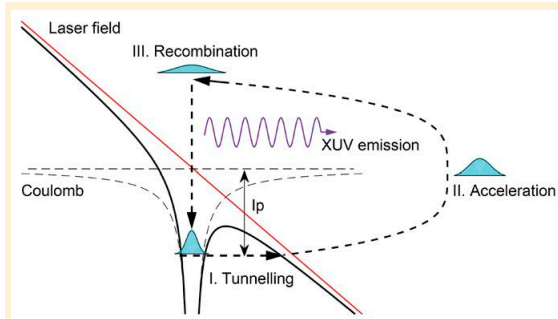


**Figure 1.** Illustration of the semi-classical three-step model for high-order harmonic generation.

of the output of an ultrafast oscillator, where the interference of the output pulses results in comb lines spaced by  $1/f$ , where  $f$  is the repetition rate of the oscillator. Single attosecond pulses (SAPs) can be obtained by spatially separating the pulses in the train [7,8] or by manipulating the driving pulse in a way that the interaction is driven by only one half-cycle of the field [9]. The conversion efficiency for HHG, *i.e.* the ratio of the energy of the attosecond pulse train or single attosecond pulse to the energy of the driving laser pulse, is about  $10^{-5}$  at best (usually lower for single attosecond pulses and for photon energies larger than 50 eV), determined both by the single-atom response and by phase-matching in the generation gas. Still, modern attosecond pulse sources can have average powers in the range of  $\mu\text{W}$  to  $\text{mW}$  [10].

After the first observation of HHG, it took almost fifteen more years until the duration of attosecond pulses in a train as well as that of a single attosecond pulse were finally experimentally measured in 2001 [11,12]. The measurement approaches, *i.e.* RABBIT (Reconstruction of Attosecond Bursts by Interference of Two-photon Transitions) for APTs and the *Attosecond Streak Camera* for SAPs, are based on performing cross-correlations of the APT or SAP with a longer low-frequency pulse, usually a copy of the driving pulse for HHG, while the photoelectron spectrum originating from a detection gas as a result of the two fields is recorded. The spectral amplitude and phase of the APT or SAP are encoded in the photoelectron spectrum and the pulses can be retrieved with different computer algorithms.

### The RABBIT technique for characterizing attosecond pulse trains

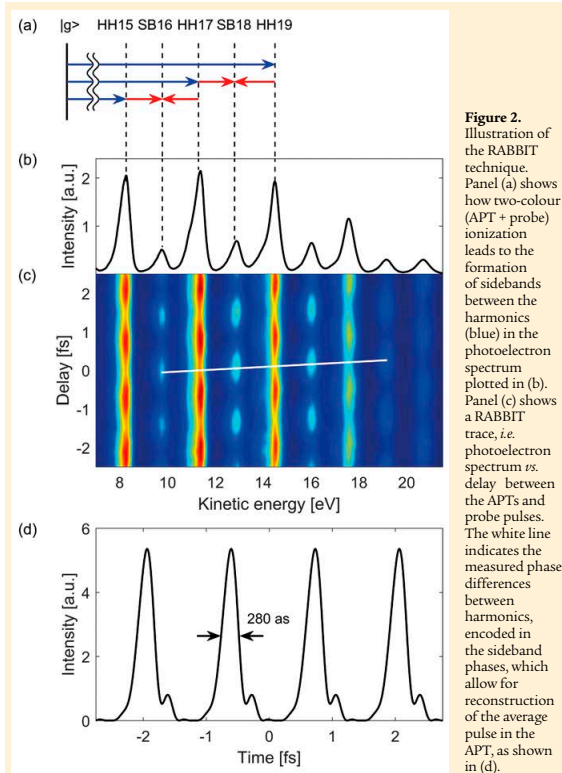
In this article, we will focus on the RABBIT technique and how it can be used to learn about fundamental electron dynamics on the attosecond

time scale. For that, we will first discuss the RABBIT scheme in more detail. The principle is illustrated in *Figure 2*. APTs synchronized with a weak copy of the driving pulse, in the following referred to as probe pulse, are sent into a photoelectron spectrometer, where photoelectrons are generated from a detection gas (usually noble gases), while the time delay between the APTs and the probe field is scanned with interferometric precision. Employing photoelectron spectroscopy for measuring attosecond pulses is somewhat obvious, taking into account that the photon energy generally overcomes the ionization potential of neutral gases. The underlying idea of RABBIT is to measure the phase difference between consecutive harmonics, which is the information needed to reconstruct the average attosecond pulse in the train. In optics, a phase difference is often assessed by interference. The different harmonics of the frequency comb representing an APT do however not result in a steady and observable interference, because they are separated in photon energy, so that the generated photoelectrons are also well separated in kinetic energy. The probe pulse however couples consecutive harmonics by introducing sidebands to the photoelectron spectrum, which are located between the harmonics. The sidebands are due to two-colour two-photon ionization; either a harmonic and a probe photon are absorbed simultaneously or a photon from the next harmonic is absorbed and a probe photon is emitted, resulting in two possible quantum paths from two consecutive harmonics to the same sideband, thus leading to interference. The sidebands oscillate with the time delay  $\tau$  between the APT and the probe field as

$$S_{2q} = \alpha + \beta \cos[2\omega\tau - \Delta\phi_{2q} - \Delta\theta_{2q}], \quad (1)$$

where  $\alpha$  and  $\beta$  describe the amplitude and contrast of the oscillations, respectively and  $\Delta\phi_{2q} = \phi_{2q+1} - \phi_{2q-1}$  is the phase difference between the consecutive harmonics of the orders  $2q+1$  and  $2q-1$ , where  $q$  is an integer.

## FOCUS | PHOTONIC DEVICES AND APPLICATIONS



The last term,  $\Delta\phi_{2q}$ , often referred to as atomic phase, is an intrinsic contribution from the detection gas due to two-colour ionization. If the phase differences between all consecutive harmonics are known, the average attosecond pulse in the train can be obtained by coherently adding the harmonics with their respective phase offsets. It should be noted that this is only accurate if the atomic contribution, *i.e.*  $\Delta\phi_{2q}$ , is small compared to the phase differences between the harmonics. Among many achievements, the RABBIT technique has shown that the intrinsic chirp of attosecond pulses, which

often is positive, can be compensated by transmission through thin metallic foils that provide anomalous dispersion in the XUV spectral range [13].

### Investigating electronic dynamics on the attosecond time scale

While the early days of attosecond science were mostly dedicated to the characterization of the spectral and temporal properties of attosecond pulses, the focus has later shifted towards actually applying those pulses for studying dynamics on a

time scale that was not accessible before. One of the most prominent questions in this respect is “how long does ionization take?”, *i.e.* “how long does it take for a photoelectron to actually *leave* the atom after interacting with an attosecond pulse?” The contrary question, *i.e.* “how long would it take the parent-atom or molecule to know that it has been ionized and become an ion?” is equally intriguing. However, since the most prominent experimental tools of the field, *i.e.* streaking and RABBIT, inherently employ photoelectron spectroscopy, the leaving of a photoelectron is more straightforward to study. It should however be noted that the ionization time is a delicate quantity to define. After ionization, the photoelectron moves in the Coulombic potential of the ion, which changes with the inverse of the distance to the ion and formally reaches infinitely far; any definition of when the photoelectron has left the proximity of the ion would be somewhat arbitrary. What helps here, is a more fundamental quantum mechanical view on ionization, where we consider photoelectron wave packets of Coulombic waves instead of a classical particle-like understanding of photoelectrons. An electron wave packet is a quantum mechanical construction, describing the electron’s probability amplitude to be found in a certain position at a certain time. After ionization the photoelectron wave packet moves in the potential landscape of the ion. Similarly to an ultrashort laser pulse propagating in a dispersive medium, where the speed is a function of wavelength, the electron wave packet will pick up a group delay, which is defined as the derivative of its phase in respect to energy. While the Coulomb potential formally reaches infinitely far, the group delay of an electron wave packet propagating through it is finite. The acquired group delay can be interpreted as ionization time. This view was first introduced by Wigner for scattering events [14].



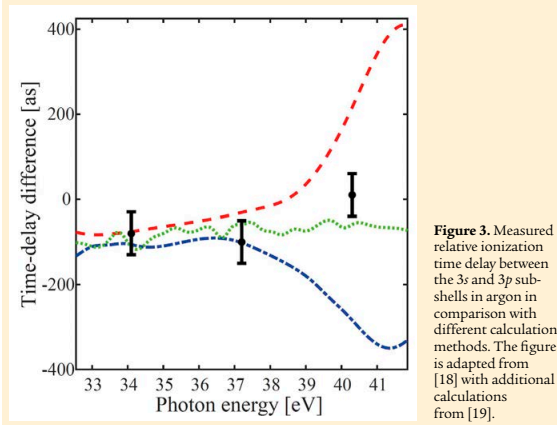


**Figure 3.** Measured relative ionization time delay between the 3s and 3p sub-shells in argon in comparison with different calculation methods. The figure is adapted from [18] with additional calculations from [19].

Determining the absolute ionization time however is complicated. Experiments have therefore mostly focused on measuring the *relative* time delay between photoelectron wave packets from different initial states, which is an easier question to answer than the absolute time delay. Prominent early examples of such experiments are the measurement of a relative time delay of about 100 as between the ionization from valence- and conduction band states in tungsten [15] as well as the relative time delay of  $21 \pm 5$  as that was measured for ionization from the 2p sub-shell in neon as compared to the 2s sub-shell [16]. The latter work, further stimulated by the intriguing fact that the magnitude of the observed time delay could not be reproduced theoretically, has triggered a vast number of experimental and theoretical efforts to understand the origin of ionization time delays, and assessing such time delays became an important direction in attosecond science throughout the last few years.

While the pioneering experiments mentioned above were performed with the streaking technique, the first attosecond ionization time delays investigated with RABBIT were measured in the  $n = 3$  shell in argon

[17,18]. The energy range around 40 eV that was investigated is particularly interesting because due to strong electron correlation effects, *i.e.* interactions between the different electrons of the atom, this energy region is difficult to treat theoretically. Thus, the measured difference in time delay can serve as qualitative indicator for the suitability of theoretical models. To illustrate how the RABBIT technique can be used to assess time delays, we shall rewrite equation 1 as

$$S_{2q} = \alpha + \beta \cos[2\omega(\tau - \tau_{2q} - \tau_\theta)], \quad (2)$$

where we express the phase differences as finite difference approximations of group delays, *i.e.*  $\tau_{2q} = \left. \frac{\partial \phi}{\partial \Omega} \right|_{\Omega=2q\omega} \approx \frac{\Delta \phi_{2q}}{2\omega}$

and  $\tau_\theta \approx \frac{\Delta \theta_{2q}}{2\omega}$ , where  $\omega$  is the carrier frequency of the laser pulses. In this view, the sideband oscillations described by equations 1 and 2, respectively can be interpreted differently. As ionization happens, the electron wave packet inherits the group delay of the harmonics, which explains one contribution to the phase of the RABBIT sidebands, *i.e.* the one corresponding to  $\tau_{2q}$ . The other contribution,  $\tau_\theta$ , refers to a delay that the electron wave packet acquires in the potential

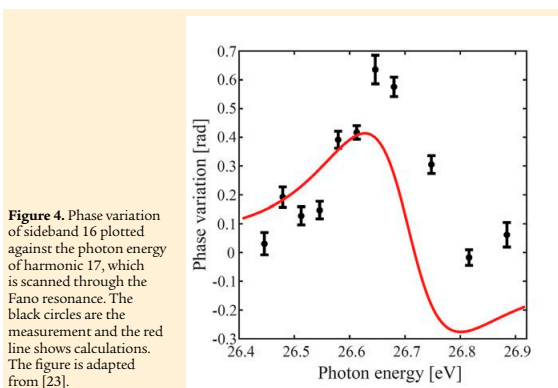
landscape of the ion in the presence of the probe field, where the contribution from the probe can often be determined theoretically [20]. While the contribution from  $\tau_\theta$  in the past was considered small, it has now moved into the focus for measuring photoionization time delays. However, determining absolute delays remains difficult since the absolute phase of a RABBIT sideband depends on the delay between the APT and the probe pulse, which usually is not known accurately enough. Thus, relative time delay measurements are performed. For example in the case of the photoionization in the  $n = 3$  shell in argon, two RABBIT traces are recorded simultaneously for photoelectrons originating from the 3p and from the 3s sub-shells. As the photoelectrons are generated from identical attosecond pulses, any relative shift of the sidebands in the two RABBIT traces must originate from different group delays that the respective electron wave packets experience as a result of two-colour ionization. Figure 3 shows measured relative time delays in comparison to different theoretical models. The different theories differ significantly around 40 eV and none of them shows perfect agreement with the measured delays.

It is fascinating to note that the relative time delays extracted from RABBIT traces are usually much smaller than the pulse duration of the attosecond pulses used in the measurement. The minimum observable delay is limited to how accurately the phase of the sidebands can be determined. This depends on the signal-to-noise ratio and the stability of the interferometer controlling the delay between the APTs and probe pulses rather than on the duration of the attosecond pulses. It is a very common feature of interferometric measurements, where often the phase of interferometric fringes can be determined with much greater accuracy than the wavelength of the light. One prominent example for this are gravitational wave detectors.

A proof-of-principle experiment performed in xenon showed that the RABBIT technique could be applied for more complicated ionization processes than those discussed so far [21]. In one-photon double-ionization, a single absorbed XUV photon leads to the ejection of two photoelectrons which share the excess energy continuously. The two electrons must thus interact with each other resulting in a time delay. Incorporating the ion into the picture, this is the prototype of the quantum mechanical three-body problem and therefore extremely interesting to study. However, recording a RABBIT trace in this case is much more challenging because the pairs of correlated photoelectrons must be measured in coincidence. This means, to be sure that two detected electrons originate from the same ionization event, one has to work at a rate of less than one event per laser shot, which makes recording RABBIT traces very time consuming and puts large demands on the laser's long-term stability. Comparing to single ionization from the  $5p$ -shell, which is recorded simultaneously, the relative ionization time delay for the double-ionization process could be extracted [21]. Here, single ionization was used as a reference clock, because the absolute phase of RABBIT sidebands, as discussed earlier, is usually unknown.

### Further developments

Since the first RABBIT measurements, femtosecond laser technology has evolved rapidly. One interesting aspect of that development is spectral tunability. Employing tunability of the carrier wavelength of the driving pulses for HHG, the high-order harmonics are no longer fixed at specific photon energies. If one harmonic is tuned through a resonance, the phase of that resonance will be carried into the sidebands above and below that harmonic. The respective next sidebands will however be unaffected and can serve as reference to extract the phase associated with the resonance. This technique was applied to study the phase in two-colour two-photon ionization of helium [22] and more recently to measure the phase evolution of a Fano resonance in argon [23]. Fano resonances are a very general phenomenon in physics, characterized by an asymmetric line shape that originates from the interference between a resonant process and a background [24]; in atomic systems, between direct photoionization to the continuum and excitation to a quasi-bound state above the ionization potential, which will rapidly decay (within femtoseconds) to the



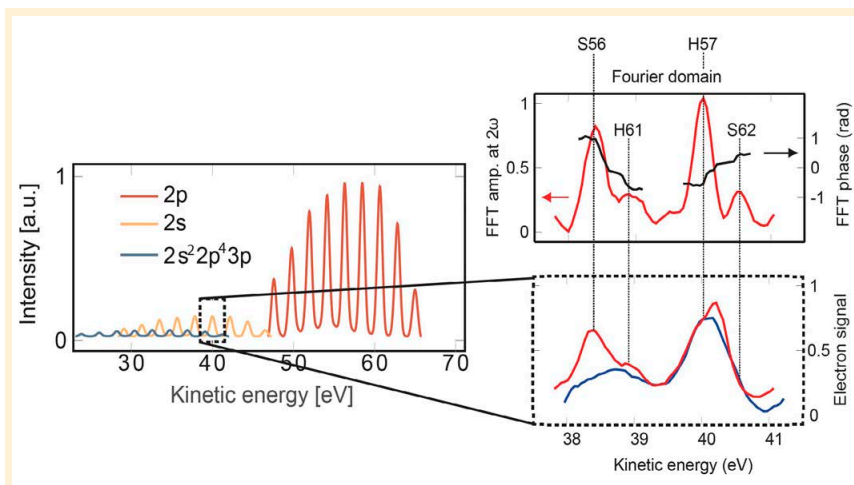


**Figure 5.** Illustration of the spectrally resolved RABBIT sideband analysis applied in [27]. The left graph shows simulated photoelectron spectra, obtained for attosecond pulse trains generated with 800 nm driving pulses, from the  $2p$  sub-shell in neon (red line, ionization potential 21.6 eV), from the  $2s$  sub-shell (yellow line, ionization potential 48 eV) and from ionization with shake-up (blue line, ionization potential 55.8 eV). The photoelectrons due to shake-up ionization lie between the ones from the  $2s$  sub-shell and would thus overlap with  $2s$  sidebands in a RABBIT measurement. The right side of the figure shows the photoelectron kinetic energy region around harmonic 57 and sideband 56 of the  $2s$  sub-shell. The lower plot shows the measured photoelectron spectrum for APTs only (blue line) and APTs+probe (red line), clearly visualizing the spectral overlap of sideband 56 with photoelectrons coming from ionization with shake up by absorption of harmonic 61. The upper plot shows the oscillation amplitude (red line) and extracted phase (black line), obtained from Fourier analysis. Only the low energy part of sideband 56 (which is free from overlap) can be used to retrieve the sideband phase.

continuum, *i.e.* auto-ionize. In the experiment, a Fano resonance in argon is spectrally scanned with harmonic 17 of a 800 nm driving pulse. The phase of the resonance is imprinted on the adjacent sidebands and can be extracted using a sideband unaffected by the resonance as reference. The experimentally obtained phase is shown in *Figure 4*. This gives a characterization of the electron wave packet in amplitude and phase, which *e.g.* in the case of helium with a single continuum channel can be used to analyse it in the time-frequency domain [25,26] similarly to what is done in ultrafast optics for ultra-short optical pulses, and provides intriguing complementary information to the spectral domain investigations extensively performed in the past.

### Conclusion

To conclude our article, we would like to focus on a very recent result. Enabled by more reliable and long-term stable lasers as well as more efficient and high-resolution photoelectron spectrometers, the signal-to-noise ratio in RABBIT measurements can be increased to a level that spectral information can now often be obtained by directly analysing the sideband phase energy-resolved instead of averaging it over the whole width of the sideband [26]. This approach has helped to resolve the long-standing mystery of the  $2s/2p$  relative ionization delay in neon [27]. One condition for a RABBIT measurement to work properly is that the sidebands are not overlapping spectrally with

any other states, which would lead to a wrong phase retrieval of the sideband. In the RABBIT traces recorded for photoelectrons from the  $2s$  and  $2p$  sub-shells in neon in [27], the  $2s$  sidebands were overlapping with peaks due to  $2p$  ionization with shake up of another  $2p$  state to the  $3p$  state, *i.e.* an ionization event where due to electron-electron interactions the ion is left in an excited state. However, the correct phase of the sideband could be obtained by only using the spectral interval where the sideband was free from overlap. Using this technique, relative ionization time delays between the  $2s$  and  $2p$  sub-shells in neon were obtained, now in excellent agreement with theory [27]. The energy-resolved sideband analysis is illustrated in *Figure 5*.

The probably most exciting aspect of the techniques discussed in this article is the ability to measure amplitude and phase of electron wave packets and by that have full access to the temporal dynamics on the attosecond time scale. Modern laser technology in combination with high-resolution photoelectron spectrometers provide high temporal and energy resolution, opening the door to measurements on more complicated systems like molecules or nano-structures. Furthermore, laser technology currently pushes the development of HHG attosecond sources with higher photon energy in the range of hundreds of electron-volts. After almost two decades of studying mostly valence shell dynamics, attosecond science is now well prepared to also put its focus on the rich dynamics of the inner atomic shells. ■

## FURTHER READING

- [1] A. McPherson *et al.*, *J. Opt. Soc. Am. B* **4**, 595 (1987)
- [2] M. Ferray *et al.*, *J. Phys. B* **21**, 31 (1988)
- [3] P. Antoine *et al.*, *Phys. Rev. Lett.* **77**, 1234 (1996)
- [4] P.B. Corkum, *Phys. Rev. Lett.* **71**, 1994 (1993)
- [5] K.J. Schafer *et al.*, *Phys. Rev. Lett.* **70**, 1599 (1993)
- [6] M. Lewenstein *et al.*, *Phys. Rev. A* **49**, 2117 (1994)
- [7] H. Vincenti *et al.*, *Phys. Rev. Lett.* **108**, 113904 (2012)
- [8] C.M. Heyl *et al.*, *New J. Phys.* **16**, 1367 (2014)
- [9] F. Calegari *et al.*, *J. Phys. B: At. Mol. Opt. Phys.* **45**, 074002 (2012)
- [10] C.M. Heyl *et al.*, *J. Phys. B: At. Mol. Opt. Phys.* **50**, 013001 (2017)
- [11] P.M. Paul *et al.*, *Science* **292**, 1689 (2001)
- [12] M. Hentschel *et al.*, *Nature* **414**, 509 (2001)
- [13] R. López-Martens *et al.*, *Phys. Rev. Lett.* **94**, 033001 (2005)
- [14] E.P. Wigner, *Phys. Rev.* **98**, 145 (1955)
- [15] A.L. Cavalieri *et al.*, *Nature* **449**, 1029 (2007)
- [16] M. Schultze *et al.*, *Science* **328**, 1658 (2010)
- [17] K. Klünder *et al.*, *Phys. Rev. Lett.* **106**, 143002 (2011)
- [18] D. Guénot *et al.*, *Phys. Rev. A* **85**, 053424 (2012)
- [19] M. Magrakvelidze *et al.*, *Phys. Rev. A* **91**, 063415 (2015)
- [20] J.M. Dahlström *et al.*, *Chem. Phys.* **414**, 53 (2013)
- [21] E.P. Månsson *et al.*, *Nature Phys.* **10**, 207 (2014)
- [22] M. Swoboda *et al.*, *Phys. Rev. Lett.* **104**, 103003 (2010)
- [23] M. Kotur *et al.*, *Nature Comm.* **7**, 10566 (2016)
- [24] U. Fano, *Phys. Rev.* **124**, 1866 (1961)
- [25] D. Busto *et al.*, *J. Phys. B* **51**, 044002 (2018)
- [26] V. Gruson *et al.*, *Science* **354**, 313 (2016)
- [27] M. Isinger *et al.*, *Science* **358**, 893 (2017)



# References

1. L. F. DiMauro. *Attophysics: Atomic photography*. Nature 419, 789–790 (2002).
2. T. H. Maiman. *Stimulated Optical Radiation in Ruby*. Nature 187, 493–494 (1960).
3. T. Brabec, Ch. Spielmann, P. F. Curley and F. Krausz. *Kerr lens mode locking*. Opt. Lett. 17, 1292–1294 (1992).
4. A. McPherson, G. Gibson, H. Jara, U. Johann, T. S. Luk, I. A. McIntyre, K. Boyer and C. K. Rhodes. *Studies of multiphoton production of vacuum-ultraviolet radiation in the rare gases*. J. Opt. Soc. Am. B 4, 595–601 (1987).
5. M. Ferray, A. L’Huillier, X.F. Li, L.A. Lompre, G. Mainfray and C. Manus. *Multiple-harmonic conversion of 1064 nm radiation in rare gases*. J. Phys. B 21, L31 (1988).
6. G. Farkas and C. Tóth. *Proposal for attosecond light pulse generation using laser induced multiple-harmonic conversion processes in rare gases*. Phys. Lett. A 168, 447–450 (1992).
7. P. B. Corkum, N. H. Burnett and M. Y. Ivanov. *Subfemtosecond pulses*. Opt. Lett. 19, 1870–1872 (1994).
8. Ph. Antoine, A. L’Huillier and M. Lewenstein. *Attosecond Pulse Trains Using High-Order Harmonics*. Phys. Rev. Lett. 77, 1234–1237 (1996).
9. P.M. Paul, E.S. Toma, P. Breger, G. Mullot, F. Augé, Ph. Balcou, H.G. Muller and P. Agostini. *Observation of a train of attosecond pulses from high harmonic generation*. Science 292, 1689–1692 (2001).
10. M Hentschel, R Kienberger, Ch Spielmann, Georg A Reider, N Milosevic, Thomas Brabec, Paul Corkum, Ulrich Heinzmann, Markus Drescher and Ferenc Krausz. *Attosecond*

- metrology*. Nature 414, 509–513 (2001).
11. M. Drescher, M. Hentschel, R. Kienberger, M. Uiberacker, V. Yakovlev, A. Scrinzi, Th. Westerwalbesloh, U. Kleineberg, U. Heinzmann and F. Krausz. *Time-resolved atomic inner-shell spectroscopy*. Nature 419, 803–807 (2002).
  12. E. Goulielmakis, Z. Loh, A. Wirth, R. Santra, N. Rohringer, V. S. Yakovlev, S. Zherebtsov, T. Pfeifer, A. M. Azzeer, M. F. Kling, S. R. Leone and F. Krausz. *Real-time observation of valence electron motion*. Nature 466, 739–743 (2010).
  13. M. Uiberacker, Th. Uphues, M. Schultze, A. J. Verhoef, V. Yakovlev, M. F. Kling, J. Rauschenberger, N. M. Kabachnik, H. Schroder, M. Lezius, K. L. Kompa, H.-G. Muller, M. J. J. Vrakking, S. Hendel, U. Kleineberg, U. Heinzmann, M. Drescher and F. Krausz. *Attosecond real-time observation of electron tunnelling in atoms*. Nature 446, 627–632 (2007).
  14. M. Schultze, M. Fieß, N. Karpowicz, J. Gagnon, M. Korbman, M. Hofstetter, S. Neppl, A. L. Cavalieri, Y. Komninos, Th. Mercouris, C. A. Nicolaides, R. Pazourek, S. Nagele, J. Feist, J. Burgdörfer, A. M. Azzeer, R. Ernstorfer, R. Kienberger, U. Kleineberg, E. Goulielmakis, F. Krausz and V. S. Yakovlev. *Delay in Photoemission*. Science 328, 1658–1662 (2010).
  15. K. Klünder, J. M. Dahlström, M. Gisselbrecht, T. Fordell, M. Swoboda, D. Guénot, P. Johnsson, J. Caillat, J. Mauritsson, A. Maquet, R. Taïeb and A. L’Huillier. *Probing Single-Photon Ionization on the Attosecond Time Scale*. Phys. Rev. Lett. 106, 143002 (2011).
  16. A. L. Cavalieri, N. Müller, Th. Uphues, V. S. Yakovlev, A. Baltuška, B. Horvath, B. Schmidt, L. Blümel, R. Holzwarth, S. Hendel, M. Drescher, U. Kleineberg, P. M. Echenique, R. Kienberger, F. Krausz and U. Heinzmann. *Attosecond spectroscopy in condensed matter*. Nature 449, 1029–1032 (2007).
  17. G. Sansone, F. Kelkensberg, J. F. Pérez-Torres, F. Morales, M. F. Kling, W. Siu, O. Ghafur, P. Johnsson, M. Swoboda, E. Benedetti, F. Ferrari, F. Lépine, J. L. Sanz-Vicario,

- S. Zherebtsov, I. Znakovskaya, A. L'Huillier, M. Yu. Ivanov, M. Nisoli, F. Martin and M. J. J. Vrakking. *Electron localization following attosecond molecular photoionization*. Nature 465, 763–766 (2010).
18. V. Vénier, R. Taïeb and A. Maquet. *Phase dependence of  $(N+1)$ -color ( $N > 1$ ) ir-uv photoionization of atoms with higher harmonics*. Phys. Rev. A 54, 721–728 (1996).
  19. H.G. Muller. *Reconstruction of attosecond harmonic beating by interference of two-photon transitions*. Appl. Phys. B 74, 17–21 (2002).
  20. D. Gabor. *Acoustical Quanta and the Theory of Hearing*. Nature 159, 591–594 (1947).
  21. S. Backus, C. G. Durfee, M. M. Murnane and H. C. Kapteyn. *High power ultrafast lasers*. Rev. Sci. Instrum. 69, 1207–1223 (1998).
  22. P. F. Moulton. *Spectroscopic and laser characteristics of  $Ti:Al_2O_3$* . J. Opt. Soc. Am. B 3, 125–133 (1986).
  23. Donna Strickland and Gerard Mourou. *Compression of amplified chirped pulses*. Optics Communication 56, 219–221 (1985).
  24. Paul B Corkum. *Plasma perspective on strong field multiphoton ionization*. Physical Review Letters 71, 1994–1997 (1993).
  25. K. J. Schafer, B. Yang, L. F. DiMauro and K. C. Kulander. *Above threshold ionization beyond the high harmonic cutoff*. Phys. Rev. Lett. 70, 1599–1602 (1993).
  26. Carsten Winterfeldt, Christian Spielmann and Gustav Gerber. *Colloquium: Optimal control of high-harmonic generation*. Rev. Mod. Phys. 80, 117–140 (2008).
  27. P. Balcou, P. Salières, A. L'Huillier and M. Lewenstein. *Generalized phase-matching conditions for high harmonics: The role of field-gradient forces*. Phys. Rev. A 55, 3204–3210 (1997).
  28. A. L'Huillier, X. F. Li and L. A. Lompré. *Propagation effects in high-order harmonic generation in rare gases*. JOSA B 7, 527–536 (1990).



29. E. Constant, D. Garzella, P. Breger, E. Mével, Ch. Dorrer, C. Le Blanc, F. Salin and P. Agostini. *Optimizing High Harmonic Generation in Absorbing Gases: Model and Experiment*. Phys. Rev. Lett. 82, 1668–1671 (1999).
30. CM Heyl, H Coudert-Alteirac, M Miranda, M Louisy, K Kovacs, V Tosa, E Balogh, K Varjú, A L’Huillier and A Couairon. *Scale-invariant nonlinear optics in gases*. Optica 3, 75–81 (2016).
31. A. L’Huillier, P. Balcou, S. Candel, K. J. Schafer and K. C. Kulander. *Calculations of high-order harmonic-generation processes in xenon at 1064 nm*. Phys. Rev. A 46, 2778–2790 (1992).
32. I. J. Sola, E. Mével, L. Elouga, E. Constant, V. Strelkov, L. Poletto, P. Villorresi, E. Benedetti, J. P. Caumes, S. Stagira, C. Vozzi, G. Sansone and M. Nisoli. *Controlling attosecond electron dynamics by phase-stabilized polarization gating*. Nature Physics 2, 319–322 (2006).
33. F. Ferrari, F. Calegari, M. Lucchini, C. Vozzi, S. Stagira, G. Sansone and M. Nisoli. *High-energy isolated attosecond pulses generated by above-saturation few-cycle fields*. Nature Photonics 4, 875–879 (2010).
34. Chen Guo, Anne Harth, Stefanos Carlström, Yu-Chen Cheng, Sara Mikaelsson, Erik Mårzell, Christoph Heyl, Miguel Miranda, Mathieu Gisselbrecht, Mette B Gaarde, Kenneth J Schafer, Anders Mikkelsen, Johan Mauritsson, Cord L Arnold and Anne L’Huillier. *Phase control of attosecond pulses in a train*. Journal of Physics B: Atomic, Molecular and Optical Physics 51, 034006 (2018).
35. E. Treacy. *Optical pulse compression with diffraction gratings*. IEEE Journal of Quantum Electronics 5, 454–458 (1969).
36. F. Verluise, V. Laude, Z. Cheng, Ch. Spielmann and P. Tournois. *Amplitude and phase control of ultrashort pulses by use of an acousto-optic programmable dispersive filter: pulse compression and shaping*. Opt. Lett. 25, 575–577 (2000).
37. O. E. Martinez. *Grating and prism compressors in the case of finite beam size*. J. Opt. Soc. Am. B 3, 929–934 (1986).

38. H. Hertz. *Über einen Einfluss des ultravioletten Lichtes auf die elektrische Entladung*. Ann. Physik 267, 983–1000 (1887).
39. A. Einstein. *Über einen die Erzeugung und Verwandlung des Lichtes betreffenden heuristischen Gesichtspunkt*. Annalen der Physik 322, 132–148 (1905).
40. N. Bohr. *On the constitution of atoms and molecules*. The London, Edinburgh, and Dublin Philosophical Magazine and Journal of Science 26, 1–25 (1913).
41. F. Quéré, Y. Mairesse and J. Itatani. *Temporal characterization of attosecond XUV fields*. J. Mod. Opt. 52, 339–360 (2005).
42. J. H. D. Eland, O. Vieuxmaire, T. Kinugawa, P. Lablanquie, R. I. Hall and F. Penent. *Complete Two-Electron Spectra in Double Photoionization: The Rare Gases Ar, Kr, and Xe*. Phys. Rev. Lett. 90, 053003 (2003).
43. A.M Rijs, E.H.G Backus, C.A de Lange, N.P.C Westwood and M.H.M Janssen. *'Magnetic bottle' spectrometer as a versatile tool for laser photoelectron spectroscopy*. Journal of Electron Spectroscopy and Related Phenomena 112, 151–162 (2000).
44. A. T. J. B. Eppink and D. H. Parker. *Velocity map imaging of ions and electrons using electrostatic lenses: Application in photoelectron and photofragment ion imaging of molecular oxygen*. Rev. Sci. Instr. 68, 3477–3484 (1997).
45. Gustavo A. Garcia, Laurent Nahon and Ivan Powis. *Two-dimensional charged particle image inversion using a polar basis function expansion*. Review of Scientific Instruments 75, 4989–4996 (2004).
46. J. Cooper and R. N. Zare. *Angular Distribution of Photoelectrons*. Journal of Chemical Physics 48, 942–943 (1967).
47. K. Zhao, T. Colvin, W. T. Hill and G. Zhang. *Deconvolving two-dimensional images of three-dimensional momentum trajectories*. Review of Scientific Instruments 73, 3044–3050 (2002).
48. M. J. J. Vrakking. *An iterative procedure for the inversion*

- of two-dimensional ion/photoelectron imaging experiments.* Rev. Sci. Instr. 72, 4084–4089 (2001).
49. Louis De Broglie. *A tentative theory of light quanta.* Philosophical Magazine 47, 411–423 (1924).
  50. Walmsley I.A. Iaconis, C. *Spectral phase interferometry for direct electric-field reconstruction of ultrashort optical pulses.* Optics Letters 23, 792–794 (1998).
  51. K. W. DeLong, Rick Trebino, J. Hunter and W. E. White. *Frequency-resolved optical gating with the use of second-harmonic generation.* J. Opt. Soc. Am. B 11, 2206–2215 (1994).
  52. Miguel Miranda, Cord L. Arnold, Thomas Fordell, Francisco Silva, Benjamín Alonso, Rosa Weigand, Anne L’Huillier and Helder Crespo. *Characterization of broadband few-cycle laser pulses with the d-scan technique.* Opt. Express 20, 18732–18743 (2012).
  53. J. M. Schins, P. Breger, P. Agostini, R. C. Constantinescu, H. G. Muller, A. Bouhal, G. Grillon, A. Antonetti and A. Mysyrowicz. *Cross-correlation measurements of femtosecond extreme-ultraviolet high-order harmonics.* J. Opt. Soc. Am. B 13, 197–200 (1996).
  54. E. S. Toma, H. G. Muller, P. M. Paul, P. Breger, M. Cheret, P. Agostini, C. Le Blanc, G. Mullot and G. Cheriaux. *Ponderomotive streaking of the ionization potential as a method for measuring pulse durations in the xuv domain with fs resolution.* Phys. Rev. A 62, 061801 (2000).
  55. E S Toma and H G Muller. *Calculation of matrix elements for mixed extreme-ultraviolet-infrared two-photon above-threshold ionization of argon.* Journal of Physics B: Atomic, Molecular and Optical Physics 35, 3435–3442 (2002).
  56. Albert A. Michelson and Edward W. Morley. *On the Relative Motion of the Earth and the Luminiferous Ether.* American Journal of Science 34, 333–345 (1887).
  57. Ludwig Zehnder. *Ein neuer Interferenzrefraktor.* Zeitschrift für Instrumentenkunde 11, 275–285 (1891).
  58. Ludwig Mach. *Über einen Interferenzrefraktor.* Zeitschrift

- für Instrumentenkunde 12, 89–93 (1892).
59. K. Varjú, P. Johnsson, R. López-Martens, T. Remetter, E. Gustafsson, J. Mauritsson, M. B. Gaarde, K. J. Schafer, Ch Erny, I. Sola, A. Zair, E. Constant, E. Cormier, E. Mével and A. L’Huillier. *Experimental studies of attosecond pulse trains*. Laser Physics 15, 888–898 (2005).
  60. S. Haessler, B. Fabre, J. Higuete, J. Caillat, T. Ruchon, P. Breger, B. Carré, E. Constant, A. Maquet, E. Mével, P. Salières, R. Taïeb and Y. Mairesse. *Phase-resolved attosecond near-threshold photoionization of molecular nitrogen*. Phys. Rev. A 80, 011404 (2009).
  61. M. Swoboda, T. Fordell, K. Klünder, J. M. Dahlström, M. Miranda, C. Buth, K. J. Schafer, J. Mauritsson, A. L’Huillier and M. Gisselbrecht. *Phase Measurement of Resonant Two-Photon Ionization in Helium*. Phys. Rev. Lett. 104, 103003 (2010).
  62. M. Kotur, D. Guénot, Á Jiménez-Galán, D. Kroon, E. W. Larsen, M. Louisy, S. Bengtsson, M. Miranda, J. Mauritsson, C. L. Arnold, S. E. Canton, M. Gisselbrecht, T. Carette, J. M. Dahlström, E. Lindroth, A. Maquet, L. Argenti, F. Martín and A. L’Huillier. *Spectral phase measurement of a Fano resonance using tunable attosecond pulses*. Nature Communications 7, 10566 (2016).
  63. V. Gruson, L. Barreau, Á. Jiménez-Galan, F. Risoud, J. Caillat, A. Maquet, B. Carré, F. Lepetit, J.-F. Hergott, T. Ruchon, L. Argenti, R. Taïeb, F. Martín and P. Salières. *Attosecond dynamics through a Fano resonance: Monitoring the birth of a photoelectron*. Science 354, 734–738 (2016).
  64. Sebastian Heuser, Álvaro Jiménez Galán, Claudio Cirelli, Carlos Marante, Mazyar Sabbar, Robert Boge, Matteo Lucchini, Lukas Gallmann, Igor Ivanov, Anatoli S. Kheifets, J. Marcus Dahlström, Eva Lindroth, Luca Argenti, Fernando Martín and Ursula Keller. *Angular dependence of photoemission time delay in helium*. Phys. Rev. A 94, 063409 (2016).
  65. James W. Cooley and John W. Tukey. *An algorithm for the machine calculation of complex Fourier series*. Mathematics

- of Computation 19, 297–301 (1965).
66. M. Swoboda, J. M. Dahlström, T. Ruchon, P. Johnsson, J. Mauritsson, A. L’Huillier and K.J. Schafer. *Intensity dependence of laser-assisted attosecond photoionization spectra*. Laser Physics 19, 1591–1599 (2009).
  67. Donald W. Marquardt. *An Algorithm for Least-Squares Estimation of Nonlinear Parameters*. Journal of the Society for Industrial and Applied Mathematics 11, 431–441 (1963).
  68. Kenneth Levenberg. *A method for the solution of certain non-linear problems in least squares*. Quarterly of Applied Mathematics 2 2, 164–168 (1944).
  69. U. Fano. *Effects of Configuration Interaction on Intensities and Phase Shifts*. Phys. Rev. 124, 1866–1878 (1961).
  70. K. Varjú, Y. Mairesse, B. Carré, M. B. Gaarde, P. Johnsson, S. Kazamias, R. López-Martens, J. Mauritsson, K. J. Schafer, PH. Balcou, A. L’huillier and P. Salières. *Frequency chirp of harmonic and attosecond pulses*. Journal of Modern Optics 52, 379–394 (2005).
  71. Álvaro Jiménez-Galán, Fernando Martín and Luca Argenti. *Two-photon finite-pulse model for resonant transitions in attosecond experiments*. Phys. Rev. A 93, 023429 (2016).
  72. Johannes Feist, Oleg Zatsarinny, Stefan Nagele, Renate Pazourek, Joachim Burgdörfer, Xiaoxu Guan, Klaus Bartschat and Barry I. Schneider. *Time delays for attosecond streaking in photoionization of neon*. Phys. Rev. A 89, 033417 (2014).
  73. L. R. Moore, M. A. Lysaght, J. S. Parker, H. W. van der Hart and K. T. Taylor. *Time delay between photoemission from the 2p and 2s subshells of neon*. Phys. Rev. A 84, 061404 (2011).
  74. J. M. Dahlström, T. Carette and E. Lindroth. *Diagrammatic approach to attosecond delays in photoionization*. Phys. Rev. A 86, 061402 (2012).
  75. J.M. Dahlström, D. Guénot, K. Klünder, M. Gisselbrecht, J. Mauritsson, A. L’Huillier, A. Maquet and R. Taïeb. *Theory of attosecond delays in laser-assisted photoionization*.

- Chemical Physics 414, 53–64 (2013). Attosecond spectroscopy.
76. S Nagele, R Pazourek, J Feist, K Doblhoff-Dier, C Lemell, K Tökési and J Burgdörfer. *Time-resolved photoemission by attosecond streaking: extraction of time information*. Journal of Physics B: Atomic, Molecular and Optical Physics 44, 081001 (2011).
  77. Eugene P. Wigner. *Lower Limit for the Energy Derivative of the Scattering Phase Shift*. Phys. Rev. 98, 145–147 (1955).
  78. L. Cohen. *Time-frequency distributions-a review*. Proceedings of the IEEE 77, 941–981 (1989).
  79. C. Bourassin-Bouchet and M. E. Couprie. *Partially coherent ultrafast spectrography*. Nature Communications 6, 6465 (2015).
  80. U. Fano. *Propensity rules: An analytical approach*. Phys. Rev. A 32, 617–618 (1985).
  81. F. Krausz and M. Ivanov. *Attosecond physics*. Rev. Mod. Phys. 81, 163–234 (2009).
  82. F. Krausz and M. I. Stockman. *Attosecond metrology: from electron capture to future signal processing*. Nat. Photonics 8, 205–213 (2014).
  83. Mauro Nisoli, Piero Decleva, Francesca Calegari, Alicia Palacios and Fernando Martín. *Attosecond Electron Dynamics in Molecules*. Chemical Reviews 117, 10760–10825 (2017).
  84. Tiberiu Arion and Uwe Hergenhahn. *Coincidence spectroscopy: Past, present and perspectives*. Journal of Electron Spectroscopy and Related Phenomena 200, 222–231 (2015).
  85. Pierre Auger. *Sur l'effet photoélectrique composé*. Journal de Physique et le Radium 6, 205–208 (1925).



# Index

- 2s2p, 51
- ADC, 32
- angular distribution, 34
- angular momentum, 28
- atto-chirp, 47
- Attosecond streaking, 44
- Auto-ionization, 48, 55
  
- CPA, Chirped Pulse Amplification, 14
- cross-section, 28
  
- dispersion, 13
  
- energy bin, 32
  
- Fano resonance, 48
- Fano's formulation, 56
- Fast Fourier-transform, 46
- Frequency-resolved, 49
  
- gain curve, 12
- Group delay, 45
  
- HHG, 6
  
- Kerr lens effect, 12
  
- Mach-Zehnder interferometer, 40
- MBES, 30
- MCP, 31
- mode-locking, 13
  
- Monte-Carlo method, 62
  
- NIR, 12
  
- Photoelectron angular distribution, 61
- photoemission, 28
- Photoionization, 28
  
- RABITT, 37, 44
- RABITT resolution, 63
- Resonant electron wave-packet, 45
  
- Shake-up, 52
- SPIDER, 36
  
- Ti:Sapphire, 12
- Time-delay, 45
- ToF, 30
- Two-photon wave-packet, 57
  
- VMIS, 33
  
- Wigner delay, 54
- Wigner representation, 57
  
- XUV, 13







FIN





This thesis deals with ultrafast dynamics of electronic processes in rare gas atoms. The processes we investigate take place during a millionth of a billionth of a second: a so-called femtosecond (0.000 000 000 000 001 s). We are able to take snapshots of these processes thanks to the possibility of creating light bursts of attosecond duration (a thousandth of a femtosecond). The ability of following charge movements in real time would give unparalleled insight into, and control of, chemical and biological processes such as photosynthesis, which involves migration of electronic charges. However, before this can be realized, the available tools need to be tested and developed on much simpler systems. This thesis then explores the time evolution of some ultrafast processes in rare gas atoms using the technique referred to as RABITT, while developing new analytical methods and courses of action for this versatile technique.



**MARCUS ISINGER**     *Time-Frequency Analysis in Attosecond Spectroscopy*     **2019**

# Time-Frequency Analysis in Attosecond Spectroscopy

---

MARCUS ISINGER

DEPARTMENT OF PHYSICS | FACULTY OF ENGINEERING | LUND UNIVERSITY

